White-Light Generation and OLED Lifetime Issues

by

Aaron R. Johnson

A dissertation submitted in partial fulfillment
of the requirements for the degree of
Doctor of Philosophy
(Macromolecular Science and Engineering)
In The University of Michigan
2008

Doctoral Committee:

Professor Jerzy Kanicki, Chair
Professor David C. Martin
Assistant Professor Jinsang Kim
Assistant Professor Jamie Dean Phillips

2008

To my family and friends, frogs, and three additional ladies who know their names.

Acknowledgements

It is a pleasure to thank the many people who have made the completion of this thesis possible. Foremost among them, I would like to thank my adviser, Professor Jerzy Kanicki, who has, for many years been a teacher, a counselor and a friend. It is with no small amount of gratitude that I credit his persistent encouragement through the tribulations of my graduate years with my continuance in the program and the completion of this body of work.

Professor Kanicki is first among a long list of professors, researchers and informal advisers at the University of Michigan who have influenced and guided me and who deserve a hearty thank-you. Thank-you to my committee, Prof. David Martin, Prof. Jamie Philips and Prof. Jinsang Kim. Thank-you to Dr. Sandrine Martin for her guidance in my first years at UofM.

I am most excited to thank my family and friends. Whatever joy I have had in Michigan can be traced, in one way or another, directly to them. From the long conversations about the esoteric nature of the universe to crass jokes about flatulence, they have been prolific. They have arrived with ice cream in the dead of night at the precise moment when ice cream was needed. They have provided long- and short-distance encouragement with a gusto and certainty. Mostly, they have been never-ending wells of love and deep pools of solace and I swim in their kindness daily.

I have also received a tremendous amount of aid from the staff at the Georgia Tech Microelectronics Research Center, most notably from Dr. Gregory Book whose skill with choosing lunch locations is surpassed only by his technical and scientific acumen.

In addition, I am fortunate to have been funded and aided by a number of generous agencies starting with the National Science Foundation, though an IGERT fellowship. In this vein, I must also thank IBM for awarding me with the IBM Ph.D. Fellowship and bringing me to the hallowed halls of the T. J. Watson Research Center in Yorktown Heights, NY for a tremendous experience I will not forget. A large thank you goes to the Office of Naval Research for funding through our partners at eMagin corp. eMagin, was of tremendous aid for the work discussed in Chapter 6 as they provided OLED samples and testing results. I wish to especially thank Dr. Fridrich Vazan for his help, conversation and efforts.

And finally, thank-you to Korea for Bi Bim Bob. Your unassuming mixture of rice, vegetables, beef and spicy pepper sauce has nourished me through the late hours of research and writing and has developed within me a mild obsession I will coddle for all my remaining days.

Table of Contents

List of Figures

List of Tables

Abstract

This thesis presents experimental results and discussion regarding issues related to organic light-emitting devices (OLEDs). In particular, this thesis has three main focuses: the generation of white light from Förster transfer in blends of emissive polymer and methods used to characterize the efficiency of that transfer; low temperature, conformal, thin film encapsulation for organic devices; and the effect of a pulsed driving scheme on the lifetime of OLEDs. In the first research focus, a method is proposed to measure the efficiency of Förster energy transfer. The efficiency of Förster transfer has previously been studied in biological systems, but this thesis presents a method which may be used for systems of semiconducting polymers. In addition, this thesis presents a theoretical basis for comparing the efficiency of a Förster-blend-based white light emitter to a similar emitter with no Förster energy transfer in order to show that white light generation from Förster transfer does, indeed, increase emission efficiency. The latter two research efforts examine the effect of encapsulation and driving scheme on the growth rate of non-emissive dark regions in OLEDs and, as such, share similar experimental apparatus. The formation and growth of non-emissive dark regions have been a persistent problem in OLED fabrication. The results presented in this thesis show that the combination of proper encapsulation and driving method can effectively slow the growth of these non-emissive regions.

Chapter 1
Background and Introduction

Introduction

Lighting of all types account for about 22% of the nation's energy consumption, or about 8.2 quads (8.2×10^{15} BTUs). Within that and as shown in Figure 1-1, commercial and residential lighting account for almost 80% of the energy consumed by lighting, with industrial and outdoor stationary lighting taking up the remaining portion. Incandescent bulbs have an energy conversion efficiency of 10% (90% going to heat) and a luminous efficiency of 13-20 lm/W while fluorescent bulbs have a conversion efficiency of about 70% and luminous efficiency of 90 lm/W (1).

The Department of Energy (DoE) has identified end-user lighting technologies as one of the least efficient energy conversion processes in modern buildings. Upwards of 58 billion dollars are spent annually on lighting alone. As such, end-user residential and commercial lighting is an area in which the aggressive pursuit of higher efficiency will yield considerable economic and environmental advantages. Towards this end, the DoE has committed to a number of technical objectives in its partnerships with industry and academia, including the development and demonstration of energy-efficient, high-quality, long lasting lighting solutions which, by the year 2025, should have the capacity

of fulfilling end-user demands using 50% less electricity than those lighting technologies in 2005.

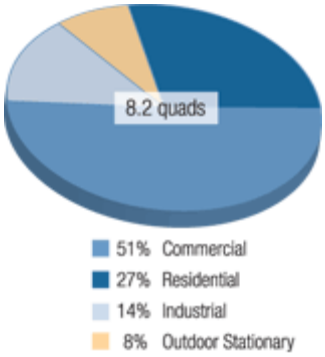

Figure 1-1: Lighting energy consumption borken down by sector.

A major area of interest, then, is the development of solid-state lighting applications, specifically organic solid-state lighting (OSSL). OSSL is an attractive technology for solid state lighting applications. Organic light-emitting devices (OLEDs) offer a number of advantages, including ease of production, fast response time, high luminance, lambertian emission (wide viewing angle), low operating voltage, emission colors across the entire visible spectrum. In 2007, the DoE funded projects in the Building Technologies Program for OLEDs totaling more than 36 million dollars. Funded research institutions included universities, corporations and national laboratories.

The success of this effort is largely dependent on technical advances made in OLED research. The DoE has set forth a roadmap of expectations for future devices. OLEDs should have a luminous efficiency of 120 lm/W for commercial applications and a luminance of 850 cd/m^2. The cap of 850 cd/m2 is required by the lighting industry so to reduce glare of the lighting element off of the room work surfaces. In addition, OLEDs should have a lifetime of 20,000 hours with a maximum luminance drop of 20% at 850 cd/m^2.

White-Emitting OLEDs

The first white OLED was produced by Junji Kido and his colleagues in 1993 (2). The Kido group doped a hole-transporting layer of poly(N-vinylcarbazole) with orange, green and blue fluorescent dyes to produce white emission. The device was successful in that sense, but it had an efficiency of less than 1 lm/W. Since that first effort, rapid progress has been made in increasing the efficiency of white OLEDs as can be seen in Figure 1-2. In June of 2007, Universal Display Corporation reported a white-emitting OLED with record efficiency of 45 lm/W at 1000 cd/m^2 (3). This device, demonstrated at the 2007 SID conference, exhibits a lifetime in excess of 4000 hours at 1000 cd/m^2.

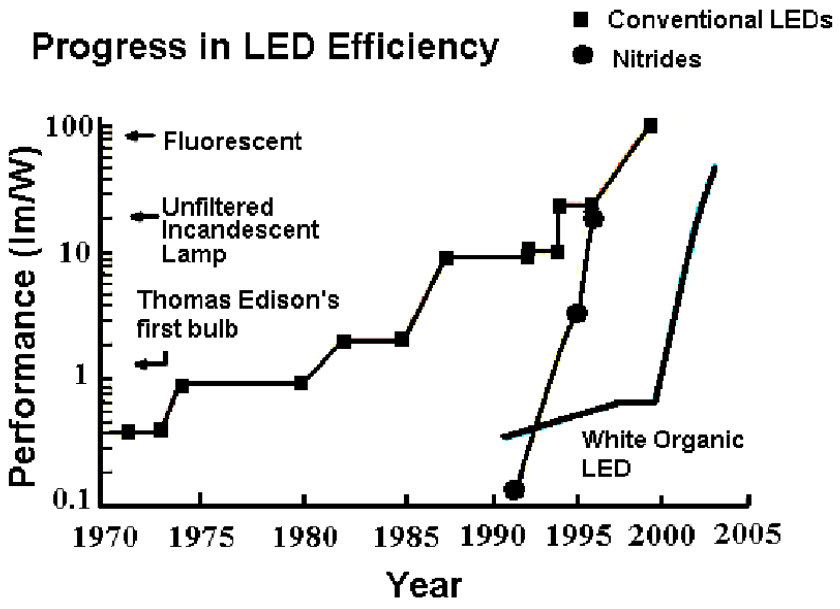

Figure 1-2: Rapid efficiency increases in white OLEDs shown in reference to inorganic LED progress.

The methods of generating white light can be generally classified in to two categories: (a) wavelength conversion and (b) color mixing. In wavelength conversion, the emission from a blue or ultraviolet OLED is absorbed by one or more phosphors. The combined emission of the OLED and the phosphors creates a broad spectrum appearing white.

Color mixing is, however, the more common technique for generating white light in OLED design. There are a number of color mixing techniques, all characterized by having multiple emitters in a single device. Some of the most common techniques are *multi-layer structures* of green, red, and blue emitters (4) (5) (6); *energy transfer blends* comprised of a blue donor and red/orange acceptor (7) (8); *bimolecular complex emitters* which produce exciplex and excimer states to broaden the emission (9) (10); *microcavity structures* which tune the final emission via deconstructive interference (11); *multi-pixel structures* which combine multiple emissive regions in to a single structure (12); and *doping* of a single emission layer with multiple emitters (2) (13) (14). Despite the multitude of viable methods for generating white illumination from organic devices, all to date degrade at a rate faster than is acceptable for commercial application. As such, lifetime issues are a major area of research within the broader OLED technological community.

Lifetime

Incandescent bulbs have a lifetime of 750-2500 hours, while fluorescent lamps have a lifetime in excess of 20,000 hours. In order to meet the needs of next generation lighting applications, OLEDs are expected to match the minimum lifetimes of current fluorescent lamps. However, the commercial viability of OLEDs is hampered by their relatively short usable lifetime, as compared to their inorganic counterparts (15). In addition, polymer-based devices have a much shorter usable lifetime than small molecule-based devices. The factors which affect OLED lifetime can broadly be classified in to two groups: intrinsic and extrinsic.

Intrinsic factors are those that, over time, diminish the emissive material's quantum efficiency. This can be, but is not limited to, chemical reactions along the polymer chain, ion migration in to the emissive layer or aggregate formation. Extrinsic factors arise from a deterioration of the device due to normal use. Among the effects of extrinsic deterioration, it is often observed that non-emissive spots appear within the device area. These "dark spots" begin small, but grow with time, reducing the emissive area of the device and, consequently, the total luminance. The area affected by this phenomenon grows linearly with time. The factors affecting the rate of growth have been a subject of ongoing investigation.

The focus of these investigation has been on the cathode/organic interface where it is understood that the diffusion of oxidizing agents cause irreversible damage to the device structure at this interface. Reactive metals, such as Mg, Ca, and Li are often used as a cathode material because their low workfunctions align well with the LUMO of the organic layers below, promoting efficiency electron injection in to the device. The high chemical reactivity of these materials, though, leaves the electrode highly susceptible to oxidation by atmospheric oxidants, such as oxygen and water vapor, which diffuse though defects in the electrode capping layer or through the organic layers below.

The oxidation of the reactive cathode alters the conductivity of the affected region and, in some cases, results in severe morphological changes in the metal film which ultimately result in cathode delamination from the organic film.

In devices utilizing poly(phenylene vinylene) (PPV) derivatives as the emission layer and a Ca/Ag cathode, Lim et. al. confirmed that dark spot formation was the result of

pinhole defects in the protective layer and, furthermore, that that the rate of dark spot growth was governed by the size of these pinholes (16). They did this by purposely adding silica particles of known sizes to the PEDOT layer and observing the growth rate of individual dark spots. In these experiments, the total dark area grows at a linear rate, even after individual dark regions begin to grow together. This suggests that dark spot growth is a function solely of the number and size of the pinholes (17). Theoretical models which link dark spot growth to the diffusion of oxygen and moisture show good agreement with this group's experimental data (18).

In addition to atmospheric oxidants diffusing down through defects in the capping layers, Nagai has shown that moisture diffusion can originate from particulate contaminants at the anode surface (19) (20). In these studies, Nagai shows that residual moisture from contaminants left on the anode diffuses through the organic layers and reacts at the organic cathode interface.

McElvain et. al. reported that for devices utilizing an Alq3 emissive layer and Mg/Ag cathode, the material cause of non-emissive regions was delamination of the cathode from the organic layer (21). This assertion is based on the observation that the adhesion between Alq3 and Mg is very poor, and when the Mg is removed by tape, very little Alq3 remains on the Mg in regions where dark spots occurred.

Liew et. al. also confirmed the relationship between cathode delamination and dark spot growth but also demonstrated that if the cathode material over the affected area were removed and a fresh cathode was redeposited, the region would subsequently emit light under applied bias (22) with no apparent dark spots. This shows that the

emissive layer is not affected by the delamination process and that dark spot formation is an extrinsic factor only.

Kolosov et. al. point out the lack of experimental evidence supporting the delamination theory of dark-spot growth (23). AFM studies of dark regions reveal that “dome-like” structures or “bubbles”, reported elsewhere (21) (24) (25) are not necessarily (and often not) associated with dark regions. They propose and alternative explanation for dark sport growth. The diffusion of water and moisture through pinholes, cracks and grain boundaries forms an insulating region at the metal/organic boundary through oxidative reactions. This process does not necessarily produce morphological changes in the film or delamination of the cathode. They do acknowledge that delamination could be an explanation for dark spot formation and growth if the process results in morphological changes too small to be detected by AFM.

One area of disagreement in these investigations is the role of applied field on the rate of dark spot growth. McElvain et. al. posit (21) that dark spot growth is independent of applied bias based on the observation that the non-emissive areas of two Alq3-based devices with Mg/Ag cathodes, one stressed at 4.5V and one unstressed, were the same after both devices were exposed to the same atmospheric conditions for 40 hours. A similar observation was also made by Kolosov et. al. (23).

Lim et. al., however, report that the applied field has a strong effect on the growth rate of devices fabricated a PPV derivative as the emissive layer and a Ca/Ag cathode (26). They report an increase in rate of dark spot growth with increasing applied field. A possible explanation for these contradictory findings is discussed in Chapter 7.

The addition of a thin (3-10nm) film of parylene between the ITO anode and the organic layers has also been shown to reduce the formation and growth rate of dark spots (27). Ke et. al. attribute this increase in device performance to better organic-organic adhesion with the HTL, increasing carrier injection efficiency. Also, the parylene layer serves to smooth the ITO surface, reducing surface roughness. A smooth ITO surface is linked to decreased occurance of dark spots as electrical shorts have also been proposed as sources for dark spot formation (28). Liu et. al. have shown that a base etching process applied to ITO anodes will reduce the roughness of the electrode, thus reducing points of high electrical field, prone to produce electrical shorts (29). Perhaps the most important advantage of a thin parylene layer, though, is that it retards the diffusion of oxygen and moisture from the ITO surface through the organic layer to the organic/cathode interface.

Packaging

These lifetime considerations have spurred interest in packaging technologies which are commensurate with OLED device structures and materials. The lifetime of OLEDs suffers greatly when exposed to atmospheric oxidants such as moisture and oxygen. Techniques to eliminate or mitigate this caustic interaction are seen as a key technology for the maturation and commercialization of OLEDs. As a first line of defense against the deleterious effects of atmospheric oxidants, many techniques have been developed to encapsulate the delicate devices using thin films of organic and inorganic materials. There is already a great deal of experience using combinations of organic and inorganic films as diffusion barriers in the beverage container and food packaging industry (30). It

is estimated that the display and lighting industry will need device encapsulation barriers capable of reducing the water vapor transmission rate to 10^{-6} g/m^2/day and the oxygen transmission rate to 10^{-5} cc(Atm.)/m^2/day.

Some of the first encapsulation methods for OLEDs were glass or metallic caps affixed to the OLED surface by epoxy resin (31) (32). These methods and those similar to them have the drawback that the encapsulation is rigid and often thicker than the actual luminescent device. This is an issue when trying to fabricate lightweight displays on flexible substrates. In response, many researchers have adopted thin film techniques to replace the rigid approach.

Methods of deposition can vary widely. Organic films can simply be spin cast or evaporated (33). Photo-curable nanocomposite resins can be applied to device surfaces using a sol-gel tequnique (34). One of the first single organic layers to be used as an OLED encapsulant is deposited by a physical chemical vapor technique. Parylene, a simple, non-damaging and conformal organic thin film is employed by Yamashita et. al. (35) They found that a film of approximately 1.2μm was sufficient to extend the lifetime of an encapsulated device to over four times that of an unencapsulated device.

Inorganic deposition techniques commensurate with organic substrates are also numerous. Atomic layer deposition (36) (37) has been used with success, though researcher report that its low deposition rate may inhibit its applicability. Sputtering of thin dielectric films has also shown promise (33) (38), but these films also tend to have high pinhole density.

Combinations of organic and inorganic films are also of interest in this regard as the addition of organic films can "fill in" the pinholes of imperfect films. Chwang et. al. demonstrated that a multilayer coating of alternating layers of Al_2O_3 (deposited by sputtering) and polyacrylate (deposited by flash evaporation followed by UV curing), with a total thickness of 5-7μm, was feasible and shows an improvement in lifetime of slightly more than 4 times that of an unencapsulated device (33). They were also able to show that thin film encapsulation can be applied to flexible substrates. Displays encapsulated via this method were able to be flexed around a 1in. tube more than 100 times without damage to the device.

Further increases in device lifetime were made by Wu et. al. by further combining polyimide, titanium nitride and stainless-steel foil films in to a hybrid encapsulation scheme (39). Using this hybrid method, the lifetime of an Alq_3-based device was increased over 25 times.

Plasma-enhanced chemical vapor deposition (PECVD) shows much promise in this area. PECVD has the potential of dense, pinhole-free and conformal thin films in a variety of materials. Rosink et. al. have shown that alternating layers of PECVD-deposited silicon oxide and silicon nitride can reduce the water vapor transmission rate to 3×10^{-5} g/m^2/day (40). In addition, they found that with the addition of a polymeric top coat, the water vapor transmission rate can be lowered further to 3.6×10^{-6} g/m^2/day. In these test they found that the top coat helped in sealing particulate contamination in to the encapsulation layer, preventing the formation of large gaps in the barrier from particles becoming dislodged.

Organization of Thesis

Chapter 2: This chapter will detail the method used to characterize organic polymer materials by electrochemistry. The cost commonly used electrochemical technique is cyclic voltammetry (CV). We have found that AC voltammetry (ACV) is a much less ambiguous means of determining energy states in polymers than CV. We describe the ACV method, and its advantages here. Results from this method were published in two referenced in IEEE Transactions on Electron Devices (41) (42).

Chapter 3: In this chapter, we present a method for characterizing the absolute PL quantum efficiency of thin organic films. This novel approach uses spectroscopic techniques to correct for self-absorption and scattering. A detailed uncertainty analysis is also presented. This method was published in review of Scientific Instruments (43).

Chapter 4: This chapter gives details on the method and materials used to fabricate and characterize the OLEDs made during this work. The techniques described in this chapter were used in fabrication for devices presented in IEEE Transactions on Electron Devices (42).

Chapter 5: This chapter explains the Förster energy transfer process and details the methods used to fabricate white-emitting OLEDs. Two blend systems are discussed. In the first system, Förster energy transfer is the sole color mixing technique observed. A method for measuring the efficiency of this energy transfer is discussed and results are presented. Methods and results regarding this system have been submitted for publication in Synthetic Metals. In the second system, an interesting phenomenon is observed as white light is generated by two distinct color mixing techniques: Förster

energy transfer and exciplex emission. Analysis of this system was submitted for publication in Applied Physics Letters.

Chapter 6: This chapters details efforts to produce thin films encapsulation structures for OLEDs. Several thin films deposition techniques are discussed including low temperature plasma-enhanced chemical vapor deposition, sputtering, and physical vapor deposition of organic films. The unique difficulties of encapsulating organic devices are discussed and results are presented.

Chapter 7: The effect of pulsed driving techniques on the lifetime of OLEDs is discussed and results are presented. The combination of encapsulation and pulsed driving is shown to be the superior method of extending OLED lifetime. Results from these studies have been submitted to IEEE Display Technology.

Bibliography

[1] Optoelectronics Industry Development Association (OIDA). *2002 Organic light emitting diodes (OLEDs) for general illumination update.* Report August. 2002.

[2] Kido, J., Hongawa, K., Okuyama, K., Nagai, K., *White light-emitting organic electroluminescenct devices using the poly(N-vinylcarbazole) emitter layer doped with three fluorescent dyes. Appl. Phys. lett.*, Vol. 64, p. 815, (1994)

[3] Universal Display Corporation Record white OLED advancements announced by Universal Display Corportation at 2007 SID conference. *UDC Press Release.* [Online] May 2007. http://www.universaldisplay.com/downloads/Press%20Releases/2007/052307.pdf.

[4] Li, G., Shinar, J., *Combinatorial fabrication and studies of bright white organic light-emitting devices based on emission from rubrene-doped 4,4[prime]-bis(2,2[prime]-diphenylvinyl)-1,1[prime]-biphenyl . Appl. Phys. Lett.*, Vol. 83, p. 5359, (2003)

[5] Ko, C. W., Tao, Y. T., *Bright white organic light-emitting diode. Appl. Phys. Lett.*, Vol. 79, p. 4234, (2001)

[6] Tokito, S., Iijima, T., Tsuzuki, T., Sato, F., *High-efficiency white phosphorescent organic light-emitting devices with greenish-blue and red-emitting layers. Appl. Phys. Lett.*, Vol. 83, p. 2459, (2003)

[7] D.Andrade, B. W., Thompson, M. E., Forrest, S. R., *Controlling Exciton Diffusion in Multilayer White Phosphorescent Organic Light Emitting Devices. Adv. Mater.*, Vol. 14, p. 147, (2002)

[8] Qin, D., Tao, Y., *White organic light-emitting diode comprising of blue fluorescence and red phosphorescence. Appl. Phys. Lett.*, Vol. 86, p. 113507, (2005)

[9] D'Andrade, B. W., Brooks, J., Adamovich, V., Thompson, M. E., Forrest, S. R., *White Light Emission Using Triplet Excimers in Electrophosphorescent Organic Light-Emitting Devices. Adv. Mater.*, Vol. 14, p. 1032, ()

[10] Feng, J., Li, F., Gao, W., Liu, S., *White light emission from exciplex using tris-(8-hydroxyquinoline)aluminum as chromaticity-tuning layer. Appl. Phys. Lett.*, Vol. 78, p. 3947, (2001)

[11] Shiga, T., Fujikawa, H., Taga, Y., *Design of multiwavelength resonant cavities for white organic light-emitting diodes . J. Appl. Phys.*, Vol. 93, p. 19, (2003)

[12] Sun, J. X., Zhu, X. L., Peng, H. J., Wong, M., Kwok, H. S., *Effective intermediate layers for highly efficient stacked organic light-emitting devices. Appl. Phys. Lett*, Vol. 87, p. 93504, (2005)

[13] Chuen, C. H., Tao, Y. T., *Highly-bright white organic light-emitting diodes based on a single emission layer. Appl. Phys. Lett.*, Vol. 81, p. 4499, (2002)

[14] Shao, Y., Yang, Y., *White organic light-emitting diodes prepared by a fused organic solid solution method. Appl. Phys. Lett.*, Vol. 86, p. 73510, (2005)

[15] Hung, L. S., Chen, C. H., *Recent progress of molecular organic electroluminescent materials and devices. Mat. Sci. Eng., R*, Vol. 39, p. 143, (2002)

[16] Lim, S. F., Ke, L., Wang, W., Chua, S. J., *Correlation between dark spot growth and pinhole size in organic light-emitting diodes. Appl. Phys. Lett.*, Vol. 78, p. 2116, (2001)

[17] Lim, S. F., Wang, W., Chua, S. J., *Degradation of organic light-emitting devices due to formation and growth of dark spots. Mat. Sci. and Eng. B*, Vol. 85, p. 154, (2001)

[18] Ke, L., Lim, S. F., Chua, S. J., *Organic light-emitting device dark spot growth behavior analysis by diffusion reaction theory. J. of Poly. Sci. B*, Vol. 39, p. 1697, (2001)

[19] Nagai, M., *Dark Spot formation and growth in color-filter-based OLED devices. J. Electrochem. Soc.*, Vol. 154, p. J116, (2007)

[20] Nagai, M., *Defects of Passivation Films for Color-Filter-based OLED Devices. J. Electrochem. Soc.*, Vol. 154, p. J65, (2007)

[21] McElvain, J., Antoniadis, H., Hueschen, M. R., Miller, J. N., Roitman, D. M., Sheats, J. R., Moon, R. L., *Formation and growth of black spots in organic light-emitting diodes. J. Appl. Phys.*, Vol. 80, , (1996)

[22] Liew, Y.-F., Aziz, H., Hu, N.-X., Xu, G., Popovic, Z., *Investigation of the sites of dark spots in organic light-emitting devices.* , Vol. 77, , (2000)

[23] Kolosov, D., English, D. S., Bulovic, V., Barbara, P. F., Forrest, S. R., Thompson, M. E., *Direct observaction of structural changes in organic light emitting devices during degradation.* , Vol. 90, , (2001)

[24] Aziz, H., Popovic, Z., Tripp, C. P., Hu, N.-X., Hor, A.-M., Xu, G., *Degradation processes at the cathode/organic interface in organic light emitting devices with Mg:Ag cathodes. Appl. Phys. Lett.*, Vol. 72, p. 2642, (1998)

[25] Do, L.-M., Oyamada, M., Koike, A., Han, E.-M., Yamamoto, N., Fujihira, M., *Morphological change in the degadation of Al electrode surgaces of electroluminescent devices by fluorescence microscopy and AFM. Thin Solid Films*, Vol. 273, p. 209, (1996)

[26] Lin, K. K., Chua, S. J., Lim, S. F., *Influence of electrical stress voltage on cathode degradation of organic light-emitting devices.* , Vol. 90, , (2001)

[27] Ke, L., Kumar, R. S., Zhang, K., Chua, S. J., Wee, A. T. S, *Effect of parylene layer on the performance of OLED. Microelectronics Journal*, Vol. 35, p. 325, (2004)

[28] Karg, S., Scott, J. C., Salem, J. R., Angelopoulos, M., *Increased brightness and lifetime of polymer light-emitting diodes with polyaniline anodes. Synth. Met.*, Vol. 80, p. 111, (1996)

[29] Liu, G., Kerr, J. B., Johnson, S., *Dark Spot formation relatice to ITO surface roughness for polyfluorene devices. Synth. Met.*, Vol. 144, p. 1, (2004)

[30] Higgins, L. M., *Hermetic and Optoelectronic Packaging Concepts Using Multiplayer and Active Polymer Systems. Advancing Microelectronics*, , p. 6, (July/August 2003)

[31] Burrows, P. E., Bulovic, V., Forrest, S. R., Sapochak, L. S., McCarty, D. M., Thompson, M. E., *Reliability and Degradation of Organic Light Emitting Devices. Appl. Phys. Lett.*, Vol. 65, p. 2922, (1994)

[32] Kawami, S., Niato, N., Ohata, H., Nakada, H., s.l. : 45th Spring Meeting Jpn. Soc. Appl. Phys. , 1998. Ext. Abstr. p. 1223.

[33] Chwang, A. B., Rothman, M. A., Mao, S. Y., Hewitt, R. H., Weaver, M. S., Silvernail, J. A., Rajan, K., Hack, M., Brown, J. J., Chu, X., Moro, L., Krajewski, T., Rutherford, N., *Thin film encapsulated flexible organic electroluminescent displays. Appl. Phys. Lett.*, Vol. 83, p. 413, (2003)

[34] Wang, Y.-Y., Hsieh, T.-E., Chen, I-C., Chen, C.-H., *Direct encapsulation of organic light-emitting devices (OLEDs) using photo-curable co-polyacrylate/silica nanocomposite resin. IEEE Trans. Adv. Pack.*, Vol. 30, p. 421, (2007)

[35] Yamashita, K., Mori, T., Mizutani, T., *Encapsulation of organic light-emitting diode using thermal chemical-vapour-deposition polymer film. J. Phys. D*, Vol. 34, p. 740, (2001)

[36] Ghosh, A. P., Gerenser, L. J., Jarman, C. M., Fornalik, J. E., *Thin-film encapsulation of organic light-emitting devices. Appl. Phys. lett.*, Vol. 86, p. 223503, (2005)

[37] Park, S.-H. K., Oh, J., Hwang, C.-S., Lee, J.I., Yang, Y. S., Chu, H. Y., Kang, K.-Y., *Ultra thin film encapsulation of organic light emitting diode on plastic substrate. ETRI Journal*, Vol. 27, p. 545, (2005)

[38] Henry, B. M., Dinelli, F., Zhao, K.-Y., Grovenor, C. R. M., Kolosov, O. V., Briggs, G. A. D., Roberts, A. P., Kumar, R. S., Howson, R. P., *A microstructural study of transparent metal oxide gas barrier films. Thin Solid Films*, Vols. 355-356, p. 500, (1999)

[39] Wu, Z., Wang, L., Chang, C., Qiu, Y., *A hybrid encapsulation of organic light-emitting devices. J. Phys. D*, Vol. 38, p. 981, (2005)

[40] Rosink, J. J. W. M., Lifka, H., Reitjens, G. H., Pierik, A., *Ultra-thin Encapsulation for large-area OLED displays.* , , , (2005)

[41] Shea, P. B., Johnson, A. R., Ono, N., Kanicki, J., *Electrical properties of staggered electrode, solution-processed, polycrystalline tetrabenzoporphyrin field-effect transistors. IEEE Trans. Elec. Dev.*, Vol. 52, p. 1497, (2005)

[42] Lee, H., Johnson, A. R., Kanicki, J., *White LED Based on Polyfluorene Co-Polymers Blend on Plastic Substrate. IEEE Trans. Elec. Dev.*, Vol. 53, p. 427, (2006)

[43] Johnson, A. R., Lee, S. J., Klein, J., Kanicki, J., *Absolute photoluminescence quantum efficiency measurement of light-emitting thin films. Rev. Sci. Instrum.*, Vol. 78, p. 96101, (2007)

Chapter 2
Electrochemical Characterization of Organic Materials

Introduction: AC voltammetry

Alternating Current Voltammetry (ACV) is an electrochemical technique used to study the reduction-oxidation systems of molecules (1) (2). Recently, it has also been used by Creager et. al. to study electroactive monolayers (3). Brevnov et. al. have used ACV to determine the chain length dependence of electron transfer kinetics between gold bead electrodes and ruthenium redox centers attached to an electrode surface via short alkanethiols (4). Little work has been done, though, to apply ACV to the task of estimating highest occupied molecular orbital (HOMO) and the lowest unoccupied molecular orbital (LUMO) values for organic thin-film materials used in different devices. The more widely adopted technique for this task, cyclic voltammetry (CV), has been used with great success for the purpose of constructing energy band diagrams of organic devices, such as polymeric light-emitting devices (PLEDs) (5) (6) (7) (8) (9) and organic thin film transistors (TFTs) (10) (11). There are drawbacks to this method, though. For example, CV measurements register reduction and oxidation current from non-reversible as well as reversible chemical reactions. Since conduction in an electrical device requires the continuous, sequential addition and subtraction of an electron to

and from an orbital, it is important to distinguish reversible current – involving molecular orbitals wherein an electron can be added and removed many times – from non-reversible current – where the addition or removal of an electron results in a permanent chemical change, altering the conductivity of the molecule at this orbital's energy level. Thus, CV voltammograms, which include both types of current, are problematic for device design because current resulting in non-reversible reactions is not indicative of a reliable conduction pathway for a properly functioning device. In addition, the interpretation of CV curves for materials with redox reactions which are not completely reversible can lead to ambiguous results, especially for materials which have multiple redox reactions in a narrow potential region.

In both of these respects, ACV offers a less ambiguous response signal than CV because it is only sensitive to reversible redox reactions (12). Since every data point is the average AC current over a user-defined integration time, a strong signal is indicative of a reduction/oxidation (redox) reaction which can be repeated – a quality necessary for electrical conduction. In other words, ACV requires the repeated addition and removal of a carrier before a signal is registered, which more closely mirrors the actual function of a molecule during device operation.

As will be seen below, ACV can provide a simpler and less ambiguous means of obtaining critical material parameters, such as HOMO and LUMO levels and, when used in conjunction with CV, can indicate

Electrochemical Instrumentation and Operation

Electrochemical measurements were performed using a CH Instruments 660a Electrochemical Workstation. A generalized schematic of a three-electrode cell consisted of a glassy carbon working electrode, a platinum counter electrode, and a Ag/Ag^{+} reference electrode is depicted in Figure 2-1. The workstation's potentiostat controls the cell by adjusting the applied voltage (V_a) across the working and counter electrode until the desired potential difference between the working and reference electrode (V_m) is reached. Current induced by the mass transfer of ions to the surface of the working and counter electrodes is registered and recorded by the workstation as the measurement signal.

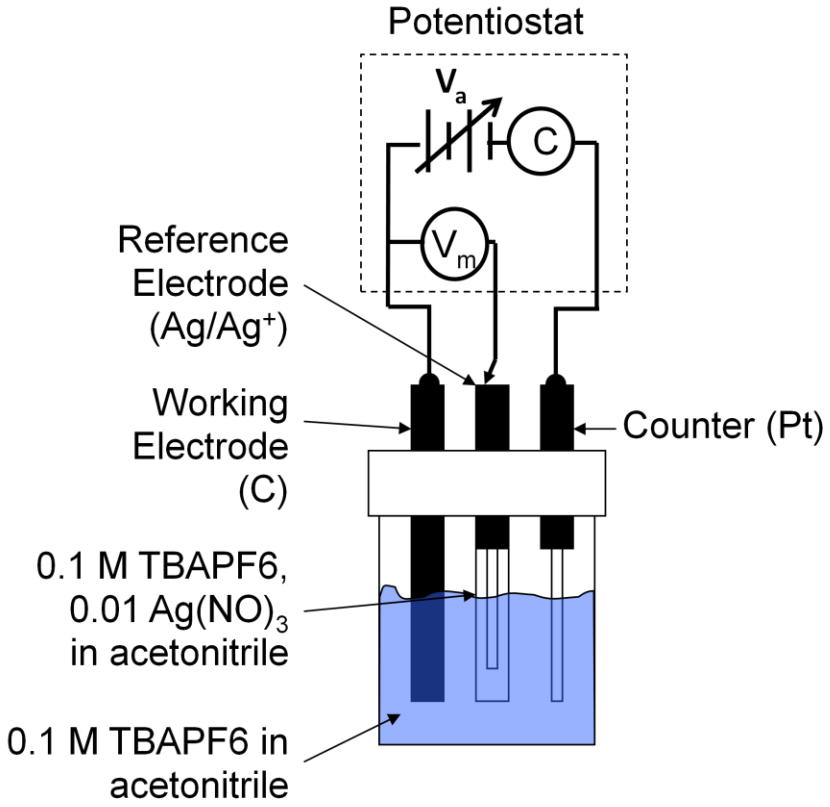

Figure 2-1. Three electrode electrochemistry cell with glassy carbon working electrode, Ag/Ag+ reference electrode and platinum counter electrode. All electrode potentials are controlled by a potentiostat.

Figure 2-2 shows the energy diagram of a cell in which the working electrode has been modified, via dip casting, with a thin, organic film. The majority of the potential between the working and counter electrode is dropped within a very short distance from the two electrode surfaces. Ideally, there is no drop in potential within the electrolyte solution, but in reality, the solution has some resistance, hence some potential drop within the solution bulk, albeit small. The electrochemical activity of interest occurs close to the surface of the working electrode. The counter material (platinum) is chosen such that the potential drop near its surface remains relatively constant with a change in current, so not to confound the measurement results.

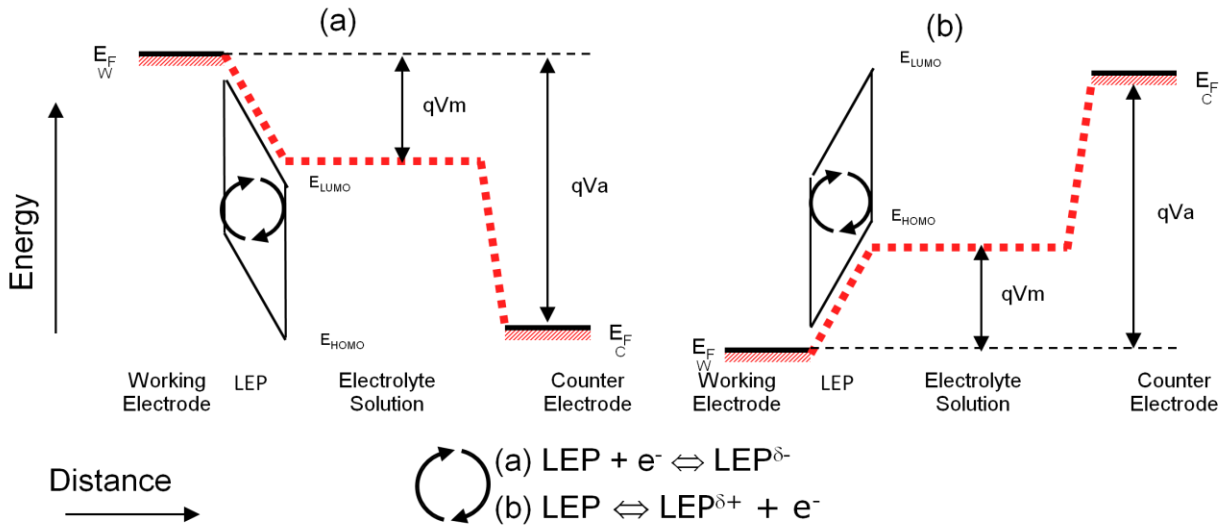

Figure 2-2. This diagram shows the cell with a sufficiently negative bias (a) to reduce the polymer films and a sufficiently positive bias (b) to oxidize the films. The dashed line indicates the potential across the cell. The potential is flat in the electrolytic solution because it is assumed that the cell has zero resistance.

In the absence of a reference electrode, the application of a voltage across the working and counter electrode is not an ideal control scheme. What is of interest to electrochemical measurements is the potential difference near the working electrode surface, directly across the film, not across the entire cell. The addition of a reference

electrode allows the potentiostat to sample the potential difference between the working electrode and the electrolyte solution by measuring the potential difference between the working and reference electrode (V_m). The reference electrode must be a well-studied redox reaction which provides a constant potential (E^0) versus a "zero potential" standard. V_m is measured in reference to E^0 of the reference electrode. The standard electrode potential of the Ag/Ag+ couple in a non-aqueous AgNO3/MeCN solution, used in these studies, is 0.5412 V (12) (13) with respect to the Standard Hydrogen Electrode (SHE) reference, chosen to be the "zero potential". No current flows through the reference electrode during measurement. Instead, cell current (C) returns to the potentiostat via the counter electrode and is recorded as a function of V_m. It should be noted that there is no electron transfer between the electrolyte solution and the counter electrode. The potential across the cell increases the concentration of one polarity of ions near the electrode surface, inducing current in the system.

When the applied potential is sufficient to raise or lower the Fermi energy of the working electrode to align with the HOMO or LUMO of the polymer film, charge transfer from the electrode to the film occurs and the film is reduced or oxidize (depending on the polarity of the applied potential). The buildup of charge within the film induces mass transfer of ions in the electrolyte solution, and the resulting current is recorded.

In the measurements that follow, the supporting electrolyte was tetrabutylammonium hexafluorophosphate (TBAPF6) in dry acetonitrile (MeCN) at a concentration of 0.1 M. The reference electrode is a silver wire in a 0.01 M solution of Silver Nitrate ($AgNO_3$) in dry MeCN which sets up the equilibrium reaction $Ag \Leftrightarrow Ag^+ + e^-$. The supporting

electrolyte solution was bubbled with nitrogen for several minutes to remove dissolved oxygen before measurements were taken. The working electrode was modified by dip casting in the organic solution and dried in air.

Both CV and ACV measurements were taken and a depiction of the potential sweeps of each is shown in Figure 2-3. CV involves scanning the potential across the polymer film at a constant rate from a starting potential to an end, and then returning to the start. In ACV, a small sinusoidal signal is superimposed over a constant sweep from a start potential to and end. At each sample point, the AC current is measured and recorded. CV scans were performed at a scan speed of 0.1 V/s and ACV scans were performed at 100Hz with a 1 second integration time. In both cases, the reduction and oxidation scans were done separately.

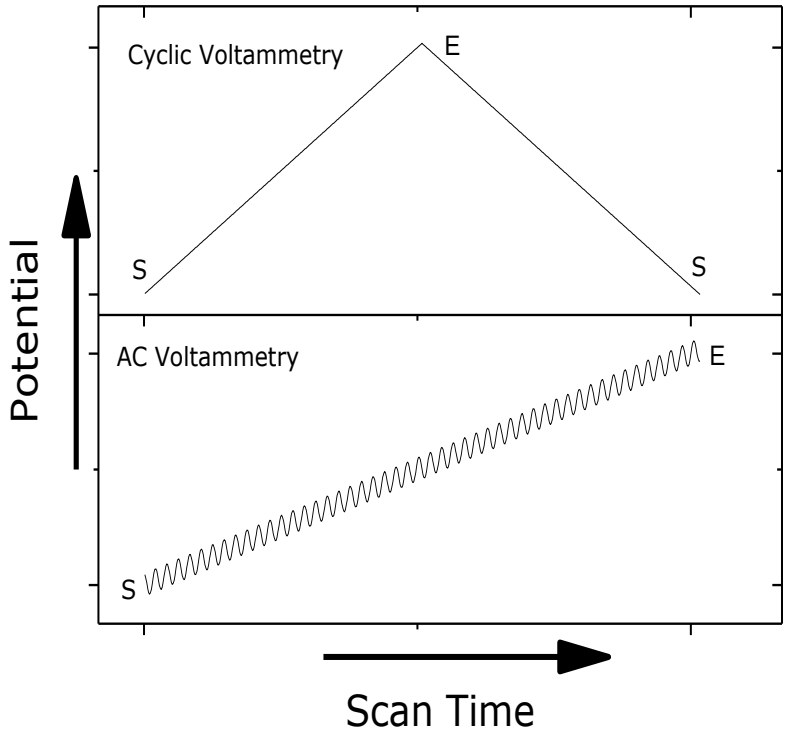

Figure 2-3. Comparison of Cyclic voltammetry and AC voltammetry. Cyclic voltammetry scan the constant potential from a start (S) to an end (E) potential and then back to S at a given rate. AC voltammetry superimposes a small sinusoidal signal on a DC sweep.

Ferrocene/Ferrocenium Standard

Figure 2-4 (a) shows the CV curve for the fully reversible redox reaction of ferrocene/ferrocenium (FOC). FOC is an instructive example since it has a well defined, reversible reaction that will allow for the comparison, discussed below, of ACV and CV curve features. In the CV curve, when V_m reaches the onset of conduction at 0.27 V vs. Ag/Ag^+, electrons begin to transfer from the ferrocene molecule to the electrode (oxidation). The transfer of an electron marks the transition from the neutral (ferrocene) to the oxidized (ferrocenium) species of the molecule. The current continues to rise until the process becomes limited by the mass transfer of the neutral

species from the solution bulk to the electrode surface, and the current falls. When, in the reverse direction, V_m reaches the onset of conduction at 0.4V vs. Ag/Ag^+, electrons begin to transfer to the oxidized molecules from the electrode (reduction), reverting the molecules back to the neutral form, until the process is, again, limited by mass transfer from the bulk solution to the electrode surface. The separation between the peaks of the forward and reverse direction measurements is a result of the kinetics of this mass transfer process. If the ferrocene molecules were confined to a small distance from the electrode surface (as is the case in organic films deposited on the electrode, such as the films described in later sections) we would expect the forward and reverse peaks to occur at the same potential.

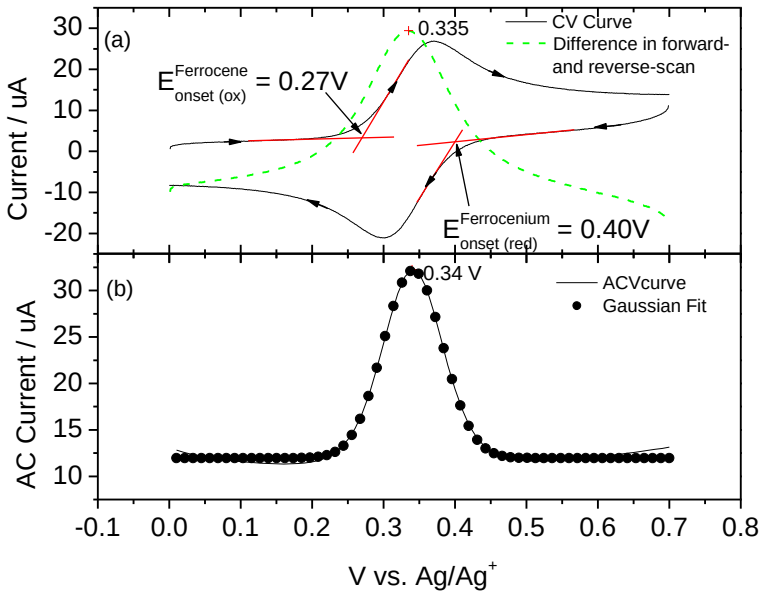

Figure 2-4. CV (a) and ACV (b) curves for a reversible redox reaction (ferrocene/ferrocenium). The dashed line in (a) represents the difference between the forward and reverse scan currents for each sampled potential.

In Figure 2-4 (b), the redox reaction is observed again, in this case using the ACV method. A strong AC signal indicates that molecules near the electrode surface oxidize

and reduce with relative ease, resulting in a large sinusoidal current as electrons transfer between electrode and molecule. This occurs when the Fermi level of the electrode is near a redox potential, E^0, of the molecule. Hence, at 0.34V vs. Ag/Ag+ where the peak of the ACV curve occurs, a relatively small change in voltage results in a large transfer of electrons between electrode and molecule, indicating the greatest alignment between the Fermi level of the electrode and the redox potential.

While the sweep potential is on the rising (left) side of the ACV peak, the FOC concentration near the electrode surface is dominated by the neutral species. Conversely, on the falling (right) side of the peak, the FOC concentration is dominated by the oxidized species. At the peak, the solution is in equilibrium with an equal concentration of neutral and oxidized molecules. The magnitude of the peak AC current is determined by the user-defined amplitude of the sinusoidal signal as well as the mass transfer kinetics from the bulk solution to the electrode surface.

Figure 2-4 also shows that the ACV curve for a completely reversible redox reaction fits very well, empirically, to a Gaussian peak. In addition, some features of the ACV curve, such as the peak position and the general curve shape, can be reproduced from the CV curve by plotting the difference between the forward and reverse direction currents. This difference is represented by the dashed line in Figure 2-4 and shows a clear peak at 0.335V vs. Ag/Ag^+, very similar to the peak potential of the ACV curve. For a completely reversible redox reaction, this should be expected. Because the reaction does not permanently alter the chemical structure of FOC, the measured AC current in ACV is, essentially, the difference between the forward and reverse direction currents. It

should be clear, then, that for FOC and for all completely reversible redox reactions, CV and ACV give very similar results for the task of determining redox potentials. However, for redox reactions which are not completely reversible, like those discussed below, the ACV features cannot be reproduced in this manner and the parameters derived from ACV and CV begin to differ.

Measurement of Organic Semiconductors

As an example, the CV and ACV measurements of a polyfluorene-based red light-emitting polymer (LEP) (14) are shown in Figure 2-5 (a) and (b), respectively. In both curves, the oxidation of the neutral LEP is in the positive potential region and the reduction of the neutral species is in the negative potential region. It should be noted that whereas Figure 2-4 depicted two species (ferrocene and ferrocinuim) with a single redox reaction, Figure 2-5 shows three species (the neutral, oxidized and reduced LEP) with several redox reactions. We will generally refer to the oxidation and reduction of the neutral species only, unless noted otherwise.

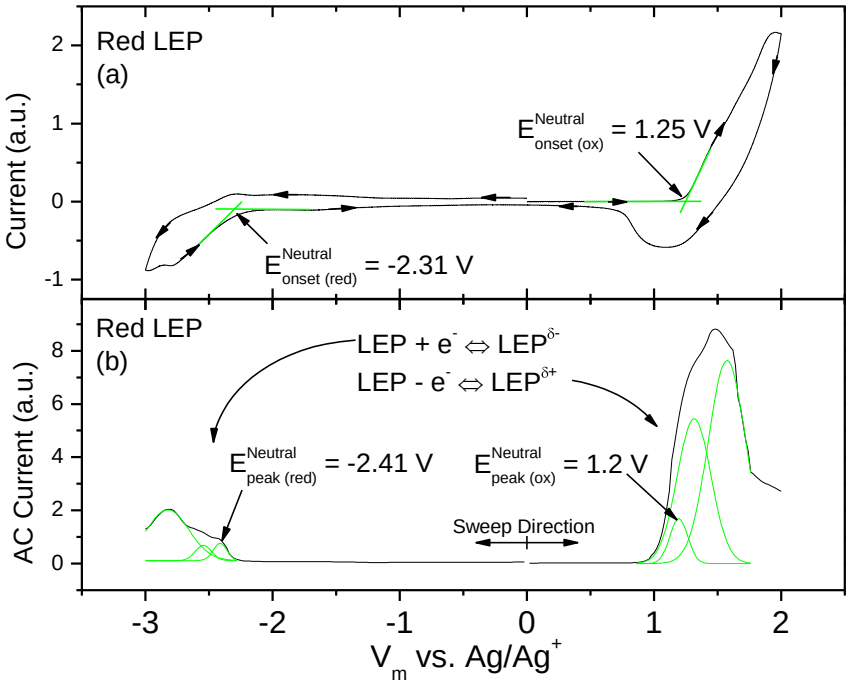

Figure 2-5. CV (a) and ACV (b) curves for red light-emitting polymer. The ACV curve was fitted to multiple Gaussian peaks in order to extract the estimated HOMO and LUMO potentials.

The redox reactions shown in Figure 2-5 are not fully reversible. This is readily apparent in the CV curve where the redox reaction current signals are not symmetrical. This implies that in addition to the injection and extraction of electrons, the chemical makeup of the film is changing. This is the case for all the PLED materials studied. The ACV signal, by contrast is not sensitive to these non-reversible reactions and only shows the fully reversible portion of the reactions. The electronically active regions of the ACV signal (cell AC current » 0) do not, however, resemble the single Gaussian peak as seen in the ACV curve for FOC. This would indicate multiple redox reactions due to conformational variations, inter- and intra-chain interactions, impurities or several electrochemically active chain segments. Because these peaks represent only reversible

reactions, it is reasonable to fit the distorted peaks to multiple Gaussian peaks as shown in Figure 2-5 (b).

It is in this regard that the advantage of ACV in determining electrical properties of semiconducting organic materials becomes clear. During normal operation of devices like OLEDs and OTFTs, current will induce both reversible and non-reversible redox reactions in the material. ACV provides a clear characterization by distinguishing the reversible reactions, which are necessary for continued device operation, whereas CV makes no distinction between the two reactions. The exclusive use of CV for the determination of HOMO and LUMO levels would introduce the possibility of mistaking a chemical change in the semiconducting film for an electronically significant charge transfer.

HOMO and LUMO values are found from the ACV curve by taking the center position of the peak closest to 0 V vs Ag/Ag^{+} in the positive and negative potential regions, respectively. The relevant oxidation and reduction peak positions of the ACV curve are at 1.2 V and -2.41 V, respectively. This is in contrast to the practice in interpreting CV curves, where redox energies relevant to HOMO and LUMO determination are taken from the onsets of conduction for both oxidation and reduction (15). Onset values are determined by extending the slope of a CV peak to a baseline, as shown in Figure 2-4 and Figure 2-5. It should be noted that onset values in ACV curves provide no useful information with respect to the redox reaction since onset values in the ACV curve are highly dependent on the magnitude of the sinusoidal signal: a user-defined parameter. The justification for using onset values is that they represent the potential at which

electrons begin to transfer in to or from the molecular film (16). In the CV curve, the onsets of oxidation and reduction potentials are 1.25 V and -2.31 V, respectively.

To relate these electrochemical potentials to vacuum level, thus obtaining the HOMO and LUMO energies, it is necessary to compare the film's redox potentials to E^0 of a known reference. FOC is often used as a pseudo-reference because its redox potential with respect to vacuum level can be approximated. Pommerehne et. al. have provided the value of -4.8 eV versus vacuum (6). The translation of V_m to energy with respect to vacuum level is done with the following equation:

$$E_{vac} = -q(V_m + 4.8 - V_{FOC}) \quad (2\text{-}1)$$

where V_{FOC} is the measured V_m of the FOC redox reaction. Thus, to perform this translation, a measurement of FOC must be made in addition to the semiconducting film. This can be done by adding a small amount of FOC to the solution when measuring the film, or in a separate independent measurement.

For the example show in Figure 2-5, the HOMO and LUMO levels as determined by ACV were -5.75 eV and -2.14 eV with an electrochemical gap of 3.61 eV. The measured results determined from the CV measurement are -5.8 eV and -2.24 eV for the HOMO and LUMO with an electrochemical energy gap of 3.56 eV.

Comparing the results from ACV to CV, the difference in electrochemical energy gap and HOMO position is about 50 meV, but the difference in LUMO positions is about 100 meV. The consequence, in terms of device design, is that the ACV method predicts a much higher barrier to electron injection and lower barrier to electron extraction at the cathode and anode electrode, respectively. In this case, the estimated barrier to

electron injection decreases by 100 meV and the estimated barrier to electron extraction increases by 50 meV. Therefore, the ACV method could predict a much lower concentration of free electrons in the light-emissive polymer due to the lower electron injection efficiency caused by the higher barrier, assuming that carriers are injected by tunneling from the metal electrode to the organic semiconductor. At the same time, ACV predicts a higher concentration of holes.

Table 2-1 summarizes the electrochemical measurements of several organic semiconductors. Many of the materials were obtained from Dow Chemical and, while the general chemical structure is known, the specific differences among the several versions of the polymer were not communicated. The materials PFAT 1, PFBTB 2, PFO-POSS, and MEHPPV-POSS were used in studies of white emission from PLEDS fabricated from blends, discussed in 0. F8BT is used in PLED lifetime studies, discussed in Chapter 6 and Chapter 7. The F8T2 series of polymers is used in organic thin-film transistors and is not discussed in this thesis.

		AC Voltammetry			Cyclic Voltammetry		
Chemical Name	**Common Name**	**HOMO**	**LUMO**	**Gap**	**HOMO**	**LUMO**	**Gap**
poly(fluorine-co-anthracene-co-p-tolylamine)	PFAT 1*	-5.61	-1.81	3.8	-5.87	-2.31	3.56
	PFAT 2*	-5.57	-2	3.57	-5.69	-2.26	3.43
poly(fluorene-co-benzothiadizol)	F8BT 1*	-5.77	-2.1	3.67	-5.83	-2.19	3.64
	F8BT 2*	-5.65	-1.99	3.66	-5.77	-2.35	3.42
	F8BT 3*	-5.57	-2.03	3.54	-5.75	-2.25	3.5
poly(fluorine-co-benzothiadiazol-co-thienyl-benzothiadizol)	PFBTB 1*	-5.95	-1.9	4.05	-5.93	-3.03	2.9
	PFBTB 2*	-5.95	-1.85	4.1	-5.8	-2.26	3.54
	PFBTB 3*	-5.9	-1.83	4.07	-5.93	**	**
poly (9, 9-dioctylfluorenyl-2, 7-diyl-co-bitiophene)	F8T2-08*	-5.47	-2.36	3.11	-5.5	-2.8	2.7
	F8T2-18*	-5.47	-2.3	3.17	-5.46	-2.36	3.1
	F8T2-22*	-5.47	-2.35	3.12	-5.52	-2.52	3
	F8T2-24*	-5.47	-2.35	3.12	-5.48	-2.53	2.95
	F8T2-25*	-5.47	-2.33	3.14	-5.51	-2.53	2.98
poly(9,9-dioctylfluorenyl-2,7-diyl)-silsesquioxane	PFO-POSS	-5.64	-2.07	3.57	-5.63	-1.89	3.74
poly(2-methoxy-5-(2-ethylhexyloxy)-1,4-phenylenevinylene)	MEHPPV-POSS	-5	-2.48	2.52	-4.92	-2.55	2.37

* Though the general chemical structure is known, the specific differences among the versions of this material were not communicated by the supplier.

** LUMO values could not be determined by Cyclic Voltammetry

Table 2-1: Electrochemical results of semiconducting polymers and small molecules

Conclusions

While the use of cyclic voltammetry as a means of determining HOMO and LUMO values for semiconducting polymers is widespread, it may not be the most unambiguous means of determining electrically active molecular states. By virtue of its insensitivity to non-reversible oxidation and reduction, AC voltammetry offers a more clear understanding of how polymers will behave when utilized in organic-based devices. This is by virtue of the fact that the applied sinusoidal bias requires the repeated addition/removal of an electron to/from the molecule before a response is recorded.

The repeated oxidation and reduction more closely mimics the behavior of active layers in organic devices. The difference between the two methods is non-trivial as the difference between ACV- and CV-estimated HOMO-LUMO gaps can be on the order of several hundred meV.

Bibliography

[1] Honeychurch, M. J., Rechnitz, G. A., Voltammetry of adsorbed molecules. Part 1: Reversible redox systems. Electroanalysis, Vol. 10, p. 285, (1998)

[2] Laviron, E., The use of linear potential sweep voltammetry and of a.c. voltammetry for the study of the surface electrochemical reaction of strongly adsorbed systems and of redox modified electrodes. J. Electroanal. Chem., Vol. 100, p. 263, (1979)

[3] Creager, S. E., Wooster, T. T., A new way of using AC voltammetry to study redox kinetic in electroactive monolayers. Anal. Chem., Vol. 70, p. 5257, (1998)

[4] Brevnov, D. A., Finklea, H. A., Ryswyk, H. V., AC voltammetry studies of electron transfer kinetics for a redoc couple attached via short alkanethiols to a gold electrode. J. Elec. Chem., Vol. 500, p. 100, (2001)

[5] Hong, Y., Hong, Z., Kanicki, J., Materials and device structures for high performance poly OLEDs on flexible plastic substrates. 2001. Proc. of SPIE. Vol. 4105, p. 356.

[6] Pommerehne, J., Vestweber, H., Guss, W., Mahrt, R.F., Bassler, H., Porsch, M., Daub, J., Efficient two layer leds on a polymer blend basis. Adv. Mater., Vol. 7, p. 551, (1995)

[7] Ciao, Y., Yu, W.-L., Chen, Z.-K., Lee, N. H. S., Lai, Y.-H., Huang, W., Synthesis and characterization of a novel light-emitting copolymer with improved charge-balancing property. Thin Solid Films, Vol. 363, p. 102, (2000)

[8] Kim, J. H., Lee, H., Efficient poly(p-phenylenevinylene) derivative with 1,2-diphenyl-2′-cyanoethene for single layer light-emitting diodes. Synth. Met., Vol. 139, p. 471, (2003)

[9] Huang, H., He, Q., Lin, H., Bai, F., Cao, Y., Properties of an alternating copolymer and its applications in LEDs and photovoltaic cells. Thin Solid Films, Vol. 477, p. 7, (2005)

[10] Wang, F., Luo, J., Yang, K. X., Chen, J. W., Huang, F., Cao, Y., Conjugated Fluorene and Silole Copolymers: Synthesis, Characterization, Electronic Transition, Light Emission, Photovoltaic Cell, and Field Effect Hole Mobility. Macromol., Vol. 38, p. 2253, (2005)

[11] Yamamoto, T., Yasuda, T., Sakai, Y., Aramaki, S., Ramaw, A., Ambipolar Field-Effect Transistor (FET) and Redox Characteristics of a pi-Conjugated Thiophene/1,3,4-Thiadiazole CT-Type Copolymer. Macromol. Rapid Comm., Vol. 26, p. 1214, (2005)

[12] Bard, A. J., Faulkner, L. R., Electrochemical Methods - Fundamentals and Applications. New York : Wiley, 2000.

[13] Meites, L., . Handbook of Analytical Chemistry. New York : McGraaw Hill, 1963.

[14] Lee, S.-J., Badano, A., Kanicki, J., Monte Carlo Simulations and opto-electronic properties of polymer light-emitting devices on flexible plastic substrates. 2003. IDRC 03. p. 26.

[15] Janietz, S., Bradley, D. D. C., Grell, M., Giebeler, C., Inbasekaran, M., Woo, E. P., Electrochemical determination of the ionization potential and electron affinity of poly(9,9-dioctylfluorene). Appl. Phys. Lett., Vol. 73, p. 2453, (1998)

[16] Bredas, J. L., Silbey, R., Boudreaux, D. S., Chance, R. R., Chain-length dependence of electronic and electrochemical properties of conjugated systems: polyacetylene, polyphenylene, polythiophene, and polypyrrole. J. Am. Chem. Soc., Vol. 105, , (1983)

Chapter 3
PL Quantum Efficiency of Polymer Thin Films

Introduction

Photoluminescence studies monitor the electronic decay of photo-excited molecules. The photo-excited molecule can decay via either radiative or non-radiative processes (1) (2) (3). To quantify the characteristic ratio of radiative process of a molecule, it is useful to define a number called the photoluminescence quantum efficiency (η_{PL}), which is the ratio of the emitted photons to the absorbed photons (4) (5). The η_{PL} of a compound in a solution is usually determined by comparing it to a standard solution. This method is valid only if the emission and absorption ratios of the standard to the sample can be accurately determined and, for thin films, such a condition is not easily met. The anisotropic films produced by spin casting typically result in angular emission patterns that differ from the standard solution. In addition, accurate determination of the reflectance of a highly scattering thin film may not be possible (4) (5). These issues can be resolved by employing an integrating sphere-based detection system, wherein the integrating sphere spatially integrates all radiant flux entering and produced within it. The procedure outlined below is used to determine absolute quantum efficiency in polymer thin film samples.

Figure 3-1 shows the photoluminescence quantum efficiency measurements system: an excitation light source with a spectral emission of $\phi_{Ex}(\lambda)$ and a detection system with a spectral response of $R_{De}(\lambda)$. The excitation light source contains a Hg/Xe lamp, monochomator and the requisite optics to maximize light throughput while protecting the monochromator gratings from infrared emissions from the lamp. A typical beam entering the integrating sphere has an excitation energy of 0.15 – 0.3 mW. $\phi_{Ex}(\lambda)$ describes the final output of the excitation system at the entrance port of the integrating sphere and is the result the spectral responses of all the optical components including the lamp, the columnating optics, the monochomator and the fiber optics.

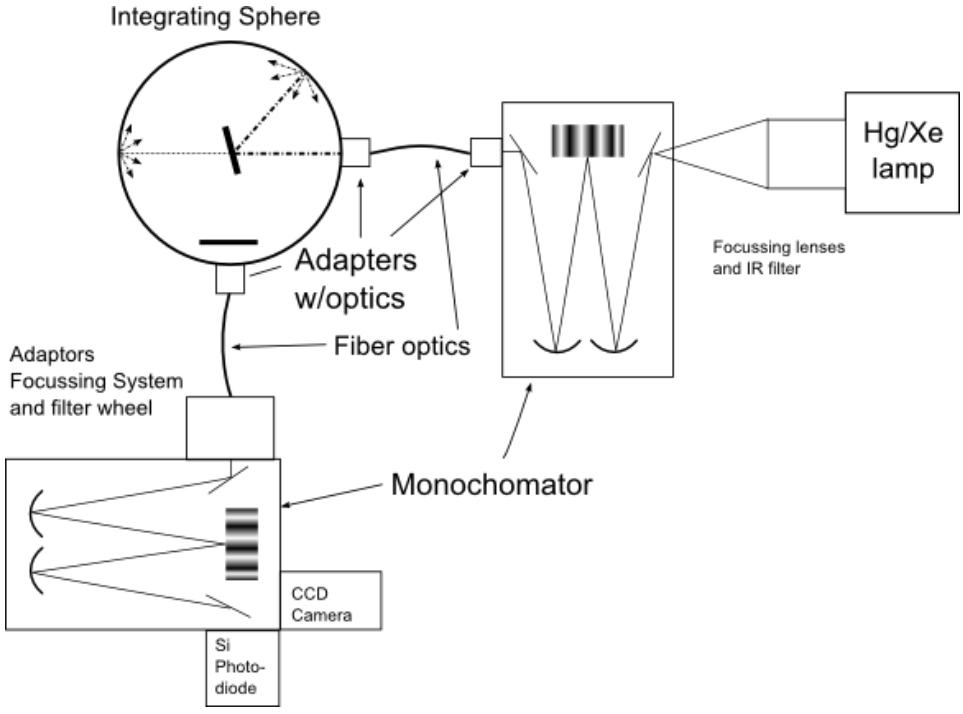

Figure 3-1: Measurement setup for photoluminescent quantum efficiency measurements

The detection system consists of an integrating sphere, monochomator, detector and supporting optics. In the system shown in Figure 3-1, either a silicon photodiode or CCD can be used, but only the silicon photodiode was used to obtain the results reported in

this note. During measurement, the sample is typically mounted in the center of the sphere, but can be moved about the interior. For any photon flux, $\phi(\lambda)$, entering or generated within the integrating sphere, the spectral response measured by the photodiode or CCD, $S(\lambda)$, to the excitation is the result of a simple geometric response of the detector, $R_{De}(\lambda)$:

$$S(\lambda) = \phi(\lambda) \times R_{DE}(\lambda) \tag{3-1}$$

Broadly speaking, determination of PL quantum efficiency follows the following procedure: calibration of the system, measurement of the excitation flux, measurement of the excitation absorption and sample emission and finally correction for sample self-absorption.

Calibrating the system

Calibration of the detection system and determination of the response function, $R_{De}(\lambda)$, proceeds with a NIST traceable tungsten lamp (OL220C from Optronics Labs) with a known spectral irradiance at 50 cm given in $W \times cm^{-2} \times nm^{-1}$ as shown in Figure 3-2. The known irradiance over the area of the sphere entrance, $\phi_{std}(\lambda)$, can be converted to photon flux entering the sphere by the relation:

$$\phi_{std}(\lambda) = \frac{\lambda}{\hbar c} \cdot I_r(\lambda) \cdot A \tag{3-2}$$

where $I_r(\lambda)$ is the known spectral irradiance obtained from the lamp manufacturer, and A is the area of the entrance to the sphere. $\phi_{std}(\lambda)$ is in units of $photons/s$ per wavelength.

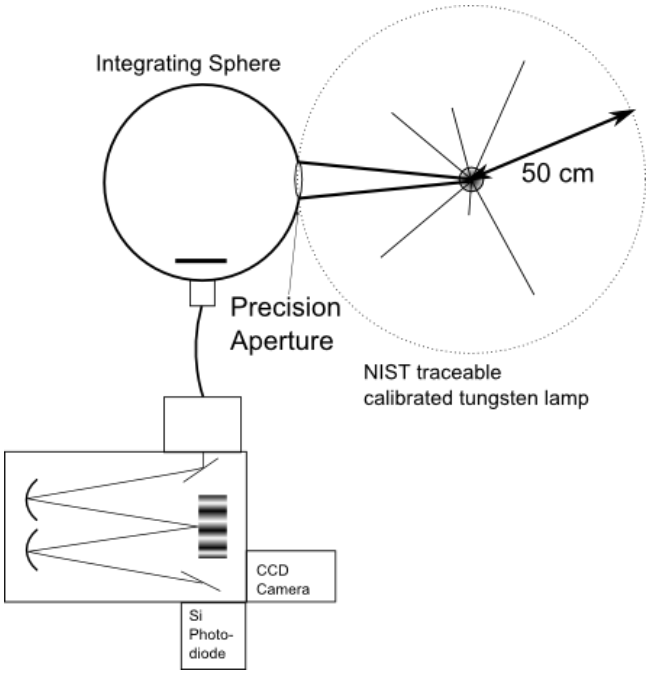

Figure 3-2: Calibration setup for spectroradiometer

We expose the sphere-based detection system to the emission of the standard lamp placed at 50 cm away from the surface of the entrance port of the sphere, through a precision aperture. The measured spectrum represents the system response to the standard lamp. $R_{de}(\lambda)$ is the ratio of the system response to the known photon flux:

$$R_{de}(\lambda) = S_{std}(\lambda)/\phi_{std}(\lambda) \tag{3-3}$$

where $S_{std}(\lambda)$ is the measured response in units of $counts \times s^{-1}$. The units of the detection response are then $counts/photon$, allowing for the proper conversion of units when this term is used to calibrate collected spectra. The relative uncertainty of the system response is found by:

$$U_{R_{de}} = \sqrt{U^2_{S_{std}}(\lambda) + U^2_{std-Lamp}(\lambda) + U^2_{detection}(\lambda)} \tag{3-4}$$

where $U^2_{S_{std}}(\lambda)$ is the relative uncertainty (type A analysis) of the measured spectrum, and $U^2_{std-Lamp}(\lambda)$ and $U^2_{detection}(\lambda)$ are the systematic relative uncertainties (discussed below) for the standard spectral irradiance lamp and the detection system, respectively. Figure 3-3 shows the calibration curve of the detection system and the relative uncertainty associated with it. The U-shape of the calibration curve is mainly contributed from the spectral variation of the blazed grating. According to an approximation to the grating equation, for blazed gratings the strength of a signal is reduced by 50% at two thirds the blaze wavelength and 1.8 times the blaze wavelength (6). Since the employed grating (with a groove density of 600 grooves/mm) has a blaze wavelength of 500 nm, its usable range is from 333 nm to 1000 nm. Therefore, the calibration factors are valid only within this spectral region of this grating. It should also be noted that the spectral responsivity of a standard silicon detector drops below 0.1 A/W at a wavelength shorter than 400 nm. The high relative uncertainty for wavelengths below 400nm is due to a combination of the silicon detector responsivity and low intensity levels from the standard lamp in that wavelength range.

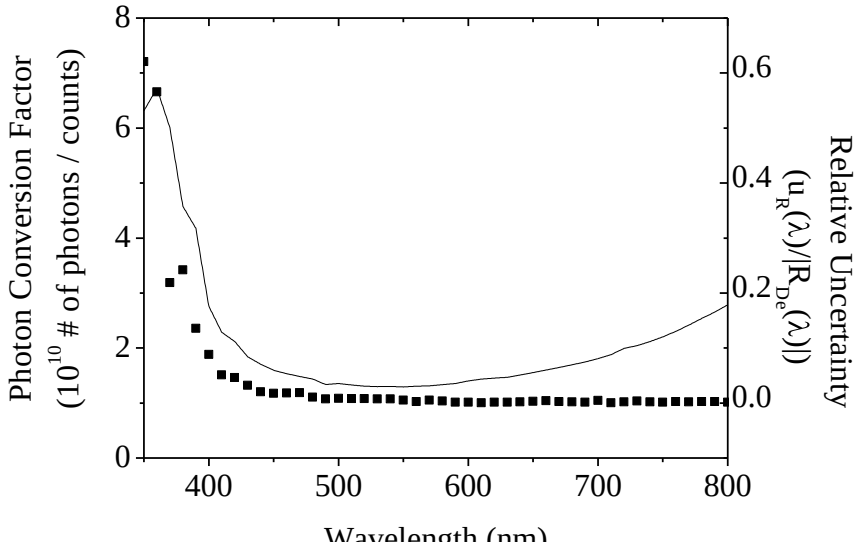

Figure 3-3: Calibration factor (inverse of the detection system response) plotted with its relative uncertainty

The photon flux of any excitation, either entering the sphere or generated within the sphere, can be determined from the measured response of the excitation, $S(\lambda)$, by the simple relation:

$$\phi(\lambda) = {S(\lambda)}\Big/{R_{de}(\lambda)} \tag{3-5}$$

The relative uncertainty in this determination follows from the law of propagating uncertainty (7):

$$U_{\phi}(\lambda) = \sqrt{U_S^2(\lambda) + U_{R_{de}}^2(\lambda) + U_{system}^2(\lambda)} \tag{3-6}$$

where $U_S(\lambda)$ is the relative uncertainty (from a type A analysis) of the measured sample, $U_{R_{de}}(\lambda)$ is the relative uncertainty for the detector responsivity and $U_{system}(\lambda)$ is the relative uncertainty for the systematic errors, which depend on the specific measurement configuration and will be described in greater detail below.

Measuring the input flux

Once the detection system is calibrated, the output of the excitation system is connected to the entrance of the integrating sphere and the total photon flux of the excitation light entering the sphere, E_a, is characterized. The lamp is first allowed to warm up for at least 60 minutes prior to measurement to minimize uncertainty in short term repeatability. E_a is determined by shining the excitation light against the sphere wall and integrating the calibrated measured response over the wavelength range of the excitation, λ_{ex}, to find the total number of photons emitting in that region. Hence, the total number of photons entering the sphere, E_a, is found by:

$$E_a = \int_{\lambda_{ex}} \phi_{Ex}(\lambda)\, d\lambda \tag{3-7}$$

where $\phi_{Ex}(\lambda)$ is the photon flux of the excitation system in to the integrating sphere and is found by applying equation (3-5. The relative uncertainty of E_a is found, again through the law of propagating uncertainty, by:

$$U_{E_a} = E_a^{-1} \sqrt{\int_{\lambda_{ex}} (\phi_{ex}(\lambda) \times U_{\phi_{ex}}(\lambda))^2\, d\lambda} \tag{3-8}$$

Measuring the Sample Emission

The emission spectrum of the sample and the absorbed excitation flux are characterized in a second measurement in which the sample is placed in the integrating sphere and directly illuminated by the excitation flux. The sample holder was designed in a way such that the light reflecting from a mounted sample will reflect away from the entrance and detection ports. The complete excitation as collected by the detector, $\phi_b(\lambda)$, is the

sum of the unabsorbed excitation light, E_b and the emission light, L_b, less the emission reabsorbed by the sample. E_b can be quantified by similar means as expressed in equation (3-7:

$$E_b = \int_{\lambda_{ex}} \phi_b(\lambda)\, d\lambda \tag{3-9}$$

with a relative uncertainty defined similarly to equation(3-8):

$$U_{E_b} = E_b^{-1} \sqrt{\int_{\lambda_{ex}} (\phi_b(\lambda) \times U_{\phi_b}(\lambda))^2\, d\lambda} \tag{3-10}$$

Self Absorption Correction

Before quantifying the total emitted flux, L_b, we must correct for self absorption of the sample. In sphere-based measurement systems, self absorption refers to the emitted flux of the test sample which bounces off the inner wall of the sphere and is, subsequently, reabsorbed by the sample. The major consequence of self absorption is that the total radiant flux, as measured, is less than the actual flux of the sample emission. Since the Stokes shift of emissive polymers is generally small, self absorption can be a significant source of error in sphere-based quantum efficiency measurements. Correcting for self absorption is a typical procedure in the characterization of the total luminous flux of broadband lamps and it is useful to critique the application of that correction procedure to the case of photo luminescent polymer thin films.

In the characterization of broadband lamps, the typical method for finding the correction factor for self absorption uses a calibrated auxiliary lamp mounted inside the integrating sphere (8). The luminous flux of the auxiliary lamp is measured by a

photopic photo-diode with and without the test lamp inside the sphere and the ratio of these values is the self-absorption correction factor. The auxiliary lamp is chosen such that its emission is similar to that of the test lamp. Hence, the absorption by the test lamp of the auxiliary flux will be comparable to the test lamp's self absorption, with a small error factor. A system such as this, which measures total luminous flux, has a correction factor of a single value representing the correction over the entire emissive band of the lamp. For a sphere-based spectroscopic radiometer (as is used in the procedure described in this chapter) the correction factor would be a function of wavelength. The purpose of a spectroscopic correction factor is to adjust the relative emission intensities, per wavelength, of a measured spectrum which exhibits self absorption to that of a theoretical spectrum which does not exhibit self absorption.

However, even if the photopic detector of the broadband lamp setup is replaced with the spectroscopic radiometer, the auxiliary lamp method is not suitable for luminescent polymer thin film samples for two reasons. First, polymer thin films are highly wavelength selective in emission and absorption. The wavelength region over which self absorption is at issue is a small band where the emission and absorption of the thin film overlap. Flux from a broadband auxiliary lamp would be subject to absorption across the entire absorption band, not just the region of absorption-emission overlap. Secondly, the absorbed photons from the broadband auxiliary lamp will excite the polymer film, inducing photoluminescence. The emitted higher wavelength photons will distort the correction factor over the emissive wavelength region.

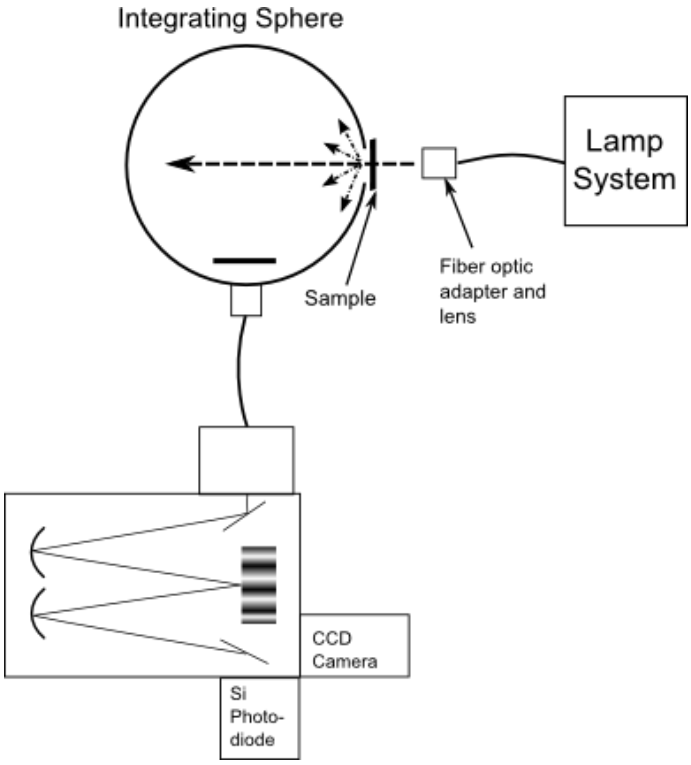

Figure 3-4: Self absorption setup for measuring the sample outside the sphere. Measuring the sample inside the sphere makes use of the normal measurement setup described above

To correct for self absorption in sphere-based PL quantum efficiency measurements, a comparison of the spectrum envelopes with and without self-absorption is made. To measure the emissive spectrum of the sample without the effect of self absorption, the sample is removed from the integrating sphere and placed outside, at the entrance of the sphere as shown in Figure 3-4. When illuminated by the excitation system, a portion of the emitted spectrum enters the sphere and is incident on the sphere walls. The remaining emitted light travels away from the opening of the sphere and has a negligible chance of bouncing off the lab walls and entering the sphere. The light entering the sphere is measured without the effect of self absorption, since any emitted light incident on the thin film sample and partially reabsorbed does so while exiting the sphere and, hence, is not collected by the detector. The result of this measurement is

an unadulterated envelope of the emission spectrum, albeit at a much lower intensity than would be measured if the sample were positioned directly in front of the detector. It is important, however, to perform this measurement with the integrating sphere so that the spectral response of the system in this measurement matches that of the calibration function.

The sample is then placed in the sphere and a repeat measurement is made. It should be clear that this measurement will be subject to the effects of self absorption whereas the first was not. The two spectra are normalized over a spectral range where self-absorption is expected to be minimal (i.e. longer wavelengths) and the correction factor is found by:

$$C_{abs}(\lambda) = \phi'_{out}(\lambda)/\phi'_{in}(\lambda) \tag{3-11}$$

where $\phi'_{out}(\lambda)$ is the normalized photon flux with the sample out of the integrating sphere, and $\phi'_{in}(\lambda)$ is the normalized photon flux with the sample inside the sphere. The relative uncertainty of the correction factor is found by:

$$U_{C_{abs}}(\lambda) = \sqrt{U^2_{\phi'_{out}}(\lambda) + U^2_{\phi'_{in}}(\lambda)} \tag{3-12}$$

where $U^2_{\phi'_{out}}(\lambda)$ and $U^2_{\phi'_{in}}(\lambda)$ are the relative uncertainties for the two measurements described above.

Figure 3-5 shows the result of correcting for self absorption on a thin film of MEH-PPV-POSS as well as the correction factor. The correction factor is taken as a function of wavelength so that it can be applied selectively to the wavelength range of the sample emission and not to the range of the excitation lamp. L_b is then found by:

$$L_b = \int_{\lambda_{emit}} \phi_{samp}(\lambda) \times C_{abs}(\lambda)\, d\lambda \tag{3-13}$$

where λ_{emit} is the wavelength range of the sample emission and $\phi_{samp}(\lambda)$ is the photon flux of the remaining excitation flux and the sample emission.

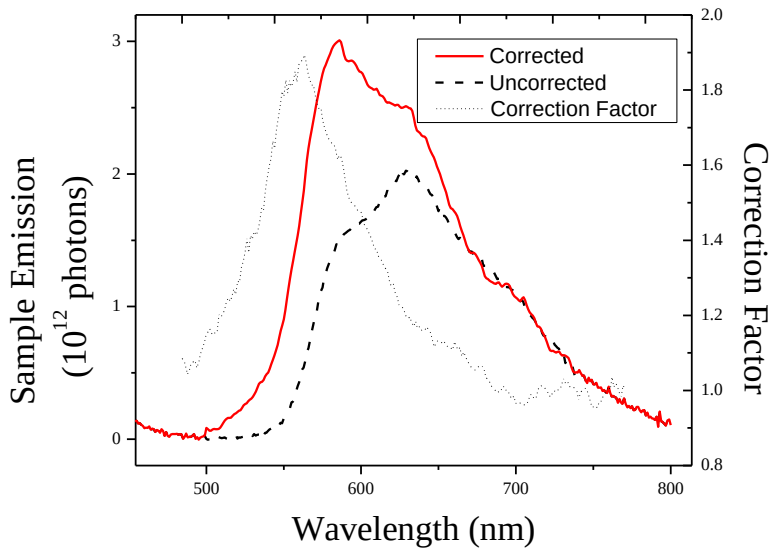

Figure 3-5: Effect of self absorption correction on the photoluminescent emission spectrum of MEH-PPV-POSS

Quantum Efficiency Measurement

When a sample is excited within the integrating sphere, a fraction, A, of excitation photons is absorbed by the sample upon first incidence. Therefore, the absorbed photons contribute to an $\eta_{PL}AE_a$ amount of the emission spectrum. As for the unabsorbed photons, $E_a(1-A)$, the spherical geometry and diffuse reflective property of the sphere reflection from the sphere wall result in isotropic illumination of the sample regardless of the sample's position within the sphere. Thus, a fixed fraction, μ, of the reflected excitation is absorbed by the sample. Secondary absorbed photons then contribute to an $\eta_{PL}\mu E_a(1-A)$ amount of the emission spectrum in the

wavelength range of λ_{emit}. Tertiary and higher order absorption can be effectively ignored as the emissions from these orders are well below the detection limit of our system. The remaining unabsorbed photons (E_b) will contribute to the resulting spectrum in the same way as the first measurement. The total number of photons absorbed ($E_a A + \mu E_a(1 - A)$) is the difference between the total number of photons entering the sphere and the number of photons not absorbed by the sample: $E_a - E_b$. With the corrected emission, L_b, the PL quantum efficiency can be found by:

$$\eta_{PL} = L_b/(E_a - E_b) \tag{3-14}$$

The relative uncertainty for this measurement, $U_{\eta_{PL}}$, follows from the law of propagating uncertainty (9):

$$U_{\eta_{PL}} = \left[U_{L_b}^2 + \frac{E_a \cdot U_{E_a}^2 + E_b \cdot U_{E_b}^2}{(E_a - E_b)^2}\right]^{1/2} \tag{3-15}$$

where U_{E_a}, U_{E_b} and U_{L_b} are the relative uncertainties in excitation flux, unabsorbed photons and emission flux, respectively.

Measurement Uncertainty

The uncertainties of this measurement procedure arise from four main sources: The standard lamp and calibration, the detection system, the excitation system used to generate photoluminescence, and the sample itself. An uncertainty budget is shown in Table 3-1.

Excitation Lamp Stability	0.5%
Standard Lamp	0.32%
Alignment and distance	0.07%
Field Stability	0.31%
Input Aperture	0.002%
Spatial uniformity	0.01%
Detector	1.01%
Photometer temperature	0.01%
Sphere reflectance uniformity	1.0%
Monochromator linearity	0.04%
Detector Sensitivity uniformity	0.1%
Light Leak	0.1%
Sample Self-Absorption	1.0%

Table 3-1: Uncertainty Budget for PL quantum efficiency measurement system

The alignment of the standard spectral irradiance and its distance from the entrance of the integrating sphere are fixed to a relative uncertainty of 0.07% based on the specifications of optical bench and mount. During calibration, the entrance of the integrating sphere is fitted with a precision aperture with a relative uncertainty of 0.002%. The NIST traceable spectral irradiance standard was calibrated, covering the spectral regions of 200 to 2500 nm with a typical relative uncertainty in field stability of 0.31% in the visible range and 0.78% in the IR region (10). Since we use a standard spectral irradiance standard to calibrate a system to measure total spectral radiance, the spatial uniformity of the standard must be taken in to consideration. At 50cm along the axis of the lamp, the OL220C, by manufacturer specifications, has a relative uncertainty in spatial uniformity of 0.01%. The combined relative uncertainty for the spectral irradiance standard is 0.32%.

In the detection system, the non-uniform spatial emissions of the thin film sample and the excitation light lead to errors as a result from sphere reflectance non-uniformity. For a spatially uniform emission within the sphere, the sphere reflectance non-uniformity is quite low – the design of the sphere ensures that the intensity of light at

any point on the sphere wall is the same as any other point. When there is a strong spatial bias to the emission, as is the case for a beam of photons entering the sphere (such as the described excitation system), or for the case of anisotropic, emissive thin films, the spatial non-uniformity creates areas of the sphere wall which deviate from the mean illumination, leading to errors in measurement. In polymer thin films, where anisotropy cannot be easily predicted or repeated, correction for this non-uniformity is not possible. Uncertainty from the anisotropy of the sample can be characterized, though, by making repeat measurements with the sample rotated axially between measurements. The directionality of the excitation light, though, is the main source of uncertainty in spatial uniformity. While the input optics diffuse the excitation light so to diminish this uncertainty, we estimate the maximum relative uncertainty in uniformity for our measurements at 1%.

Spectral mismatch errors are generally not an issue when measuring total spectral radiant flux (11). However, monochromator linearity, light leakage and detector sensitivity uniformity were determined during manufacturer calibration of the instrumentation to be no greater than 0.04%, 0.01%, 0.1%, respectively, over the visible range. In our experimental setup, the detector is positioned away from the incident light. As a consequence, the main source of temperature instability comes from heating of the sphere wall, which is quite low. This leads to an estimated relative uncertainty of 0.01%. The combined relative uncertainty for the detection system is no greater than 1.01%.

During the normal procedure described above, the flux at the entrance port of the integrating sphere from the lamp-monochomator is characterized. Hence, the relative uncertainties of the excitation system, are reduced to spectral field stability, which is estimated by the manufacturer to be 0.5% across the visible spectrum. The primary source of uncertainty from the sample is self absorption of emitted photons. We estimate the uncertainty of the self-absorption correction (described above) to be 1%.

System Validation and Sample Measurement

To validate the measurement setup, we measured the photoluminescence quantum efficiency of a 10-5M solution of rhodamine 6G in ethanol. We compared our data with results from literature. The reported η_{PL} of rhodamine 6G in ethanol is 93-95% at a solution concentration of 10-5 M and an excitation wavelength of 492 nm (12) (13). We measured the η_{PL} of rhodamine 6G as 94.33 ± 3.02% (k = 2) which matches very well with accepted values.

This measurement technique was applied to three polymers commonly used in organic electroluminescent devices, orange-emitting poly(2-methoxy-5-(2-ethylhexyloxy)-1,4-phenylenevinylene) (MEHPPV-POSS), blue-emitting poly(9,9-dioctylfluorenyl-2,7-diyl) (PFO-POSS) and green-emitting poly(9,9'-dioctylfluorene-alt-benzothiadiazole) (F8BT). The samples were illuminated near their absorption maxima: 433nm for MEHPPV-POSS, 362nm for PFO-POSS, and 400nm for F8BT. Quantum efficiency values for these polymers in thin films and in solution are summarized in Table 3-2. As expected, concentration quenching leads to lower values for η_{PL} in the thin film samples than in the solution samples. The thin film quantum efficiencies for MEHPPV-POSS, PFO-POSS

and F8BT are 4.21%, 29.04% and 62.41%, respectively, while the solution samples yield 18.93%, 70.01% and 80.44%, respectively.

The uncertainty of the measurements varies greatly. While systematic uncertainties remain constant for each sample, a number of elements change from sample to sample which do, indeed, affect the uncertainty. These include the excitation wavelength, the absorption of the sample (which is also affected by the sample thickness and the concentration) and the PL emission intensity. The absorption and PL emission intensity of the sample directly relate to the relative uncertainties U_{L_b} and U_{E_b} in that lower absorption and emission increases the noise to signal ratio.

The measurement uncertainty is strongly affected by the excitation wavelength due to a combination of the calibration method used and the hardware used to realize this measurement design. As can be seen in Figure 3-3, the relative uncertainty of the calibration function rises sharply below 400nm. This is due two both the lower response of the silicon photodiode at lower wavelengths and to the low emission intensity of the calibration lamp within the lower wavelength range. At 362 nm (the excitation wavelength for the PFO-POSS samples), the relative uncertainty of the calibration function is 48%. The result of which is that, in the case of PFO-POSS, the uncertainty of the measurement rises to unacceptable levels – 20.08% for the thin film and 29.6% for the solution. Since this is a product of the system uncertainty, high levels of uncertainty are not unique PFO-POSS and any sample which is excited at low wavelength will exhibit high uncertainty. The relative uncertainty at 400 nm (the excitation wavelength of the PFBT samples) is 8.8%. While significantly lower than the uncertainty at 362 nm, this

still produces an uncertain measurement: 12.4% for the thin film and 3.01% for the solution. Measurements of MEHPPV-POSS, however, have much more acceptable levels of uncertainty, 0.2% for the thin film and 0.56% for the solution. This is due to the fact that in the wavelength range of the sample excitation and emission, the uncertainty is quite low. At 433nm, the calibration function uncertainty is 2.8%, at 600 nm the calibration function uncertainty is 0.14% and at 700nm the calibration function uncertainty is 0.48%.

Sample	ηPL	Uη (k=2)
MEH-PPV-POSS (thin film)	4.21%	± 0.20%
MEH-PPV-POSS (10-6 M in xylenes)	18.93%	± 0.56%
PFO-POSS (thin film)	29.04%	± 20.08%
PFO-POSS (10-5 M in xylenes)	70.01%	±29.60%
F8BT (thin film)	62.41%	± 12.4%
F8BT (10 mg/mL in xylenes)	80.44%	± 3.01%

Table 3-2: PL quantum efficiency values for polymers

Conclusions

The method described above has shown to be an effective means of quantifying the PL quantum efficiency of both polymer thin films and dilute solutions. The use of such characterization tools is essential in OLED design as it aids in the proper selection of emissive materials. In addition, such a tool can be used to study the complex dynamics of radiative and non-radiative energy transfer in blends of emissive polymers.

Bibliography

[1] Turro, N. J., . *Modern Molecular Photochemistry.* New York : Benjamin/Cummings, 1978.

[2] Swenberg, M. Pope and C. E., . *Electronic Processes in Organic Crystals.* Oxford : Clarendon, 1982.

[3] M. Yan, L. J. Rothberg, F. Papadimitrakopoulos, M. E. Galvin, and T. M. Miller, *Defect Quenching of Conjugated Polymer Luminescence. Phys. Rev. Lett.*, Vol. 73, p. 744, (1994)

[4] J. C. de Mello, H. F. Wittmann, and R. H. Friend, *An improved experimental determination of external photoluminescence quantum efficiency. Adv. Mater.*, Vol. 9, p. 230, (1997)

[5] N. C. Greenham, I. D. W. Samuel, G. R. Hayes, R. T. Philips, Y. A. R. R. Kessener, S. C. Moratti, A. B. Holmes, and R. H. Friend, *Measurement of absolute photoluminescence quantum efficiencies in conjugated polymers. Chem. Phys. Lett.*, Vol. 241, p. 89, (1995)

[6] Thevenon, J. M. Lerner and A., Edison, New Jersey : Jobin Yvon Inc, 1988.

[7] ISO, . *Guide to the Expression of Uncertainty.* 1995.

[8] CIE, . *Publication No. 25, Procedures for the Measurement of Luminous Flux of Discharge Lamps and for Their Calibration as Working Standards.* Vienna, Austria : Central Bureau of the CIE, 1973.

[9] Standardization, International Organization for, . *Guide to the Expression of Uncertainties in Measurements.* 1995.

[10] Inc, Optronics Laboratories, . *Bulletin 6, Rev. 3-07.*

[11] Y. Ohno, Y. Zong, Mexico : CENAM, Proc. Symp. Metrology 2004, Published in CD, 2004.

[12] Georges, M. Fischer and J., *Fluorescence quantum yield of rhodamine 6G in ethanol as a function of concentration using thermal lens spectrometry. Chem. Phys. Lett.*, Vol. 260, p. 115, (1996)

[13] Arden, J., Deltau, G., Huth, V., Kringel, U., Peros, D., Drexhage, K. H., *Fluorescence and lasing properties of rhodamine dyes. J. Lumin.*, Vols. 48-49, p. 352, (1991)

Chapter 4
OLED Fabrication

Introduction

The general structure of a PLED can be broadly classified in to two categories, top- and bottom-emitting (1) (2), and sub-categorized in to two addition designations, standard and inverted (3)(4). This nomenclature refers to the direction through which emitted light travels (in the distinction between bottom- and top-emitting) and the orientation of the electrodes with respect to the substrate (in the distinction between standard and inverted).

Top-emitting OLEDs emit light away from the substrate and through the top electrode, which must be made to be transparent or semi-transparent. Similarly, the bottom electrode is chosen to be highly reflective so to increase the total light output through the top electrode. By orienting the light emission to be topwards, a wide variety of substrates can be used, including silicon(5), stainless steel (6), and even paper(7). Because of the wide variety of substrates available for top-emission OLEDs, this is a desirable device structure for a wide variety of applications including high aperture ratio displays (8), solid state white lighting (9)(10) and wearable displays(11). Top-emission OLEDs have an additional advantage over their bottom-emitting counterpart in that they

present fewer optical interfaces to emitted light and, as a result, tend to have higher extraction efficiency owing to diminished waveguiding (12) (13).

Bottom emission OLEDs, by contrast, orient the emission of light to travel through the substrate which must, by necessity, be transparent. Common choices for transparent substrates are glass (14) and plastic (15). In addition, the bottom electrode must also be transparent and the top electrode reflective. Despite having limited options for the choice of substrate, bottom-emitting OLEDs are widely researched due to the accessibility of transparent conductive oxides (TCOs), serving as transparent electrodes, which are much simpler to deposit on inorganic and robust substrates than on the delicate organic layers, as would be required if the TCO were to be used as a top electrode.

Alternatively, several groups have fabricated transparent OLEDs which employ a transparent substrate and transparent anodes and cathodes(16) (8). Light is emitted in both directions providing illumination to an observer on either side of the device.

All devices discussed within this thesis employ a bottom-emitting, standard multi-layer structure shown in Figure 4-1. While top emission PLEDs offer a number of advantages for production-quality devices, the PLED used in this thesis are regarded as testing platforms for additional design elements, and as such, simplicity in fabrication and low cost are favored over flexibility in substrate material and higher outcoupling. Glass substrates are used throughout these experiments detailed here. From the substrate up, the order of the layers is glass substrate, transparent conductive anode (deposited

and patterned by Thin Film Devices), a hole injection layer, the emissive layer and, finally, the cathode. The materials used are discussed below.

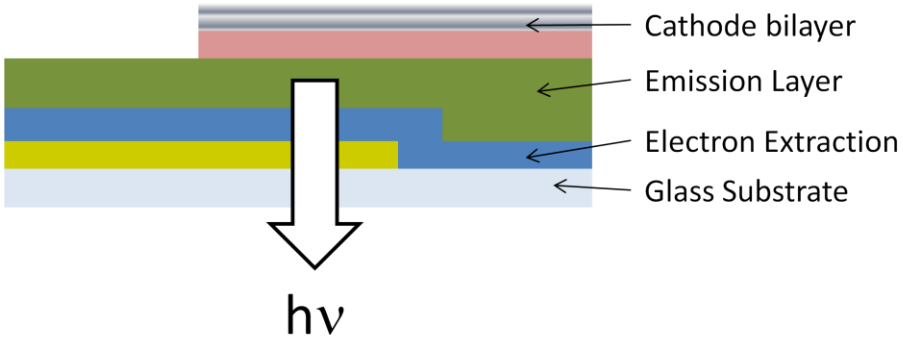

Figure 4-1: Schematic of bottom emitting PLED structure.

Structure and Materials

Transparent anode - Indium Tin Oxide

Indium tin oxide (ITO) layers are prepared via sputtering with an indium oxide (In_2O_3)/ tin oxide (SnO_2) target. ITO is an apt choice for the transparent anode due to its high transparency (17) (>85% over the visual spectrum) and its low resistivity (< 10 Ω/☐) given the right post-deposition annealing conditions and oxygen content (17)(18). Because of the high workfunction of ITO (4.7-5 eV), ITO efficiently extracts electrons from the organic layers subsequently deposited.

Hole Injection Layer – PEDOT:PSS

Poly(4-styrenesulfonate)-doped poly(3,4-ethylenedioxythiophene) (PEDOT:PSS) is used as a hole injection layer between the device anode and the emission layer. PEDOT:PSS is obtained from H.C. Starck with the commercial name BAYTRON P in an aqueous solution and used without further purification. Spin coating of PEDOT at 4000 rpm

typically results in a 60nm thick film. Electrochemical deposition of PEDOT was not considered in order to remain consistent with commercial procedures.

Emissive Layer – F8BT

poly(2,7-(9,9-di-n-octylfluorene-alt-benzothiadiazole) (F8BT) was obtained from DOW Chemical as part of a collaboration with the Kanicki group. F8BT is a fluorene -based polymer widely used in organic-based devices due to its high brightness and charge transfer efficiency(19)(20). The chemical structure is shown in Figure 4-2.

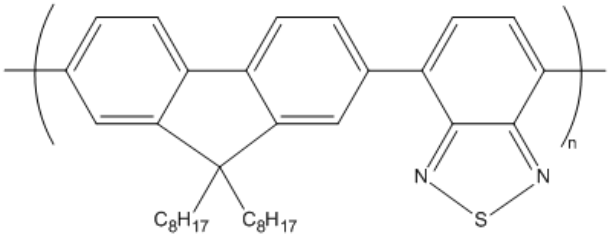

Figure 4-2: Chemical structure of F8BT

F8BT has two absorption bands centered at 470nm (2.62 eV) and 326nm (3.8 eV). The onset of absorption occurs at 547nm giving an optical gap of 2.26 eV. F8BT emits a yellow-green color with broad spectral peaks, the dominant of which is centered at 536nm (2.31 eV). The maximum emission occurs at 496nm (2.5 eV). AC voltammetry measurements reveal a HOMO of -5.57 eV and a LUMO of -2.03 eV. The electrochemical gap is, then, 3.54 eV, which is 1.28 eV larger than the estimated optical gap. The molecular weight for the F8BT polymer was 25,000 (21).

Emissive Layer – PFO-POSS and MEHPPV-POSS

Poly(9,9-dioctylfluorenyl-2,7-diyl) (PFO) and poly(2-methoxy-5-(2-ethylhexyloxy)-1,4-phenylenevinylene) (MEHPPV) are widely studied materials for use in OLEDs (22)(23), sensors(24)(25), solar cells (26) and other organic-based devices in research

environments. In the white-light studies, detailed in Chapter 5, PFO and MEHPPV are used because of their high brightness and because their emission colors make them ideal for the production of white light through blending.

While these materials generate a great deal of research interest, their widespread use in commercial applications is hampered by the ease in which the materials degrade under normal device operation. This degradation comes in the form of aggregate formation, side chain chemical reactions, and, in the case of blends of polymers, phase separation due to high chain mobility. The latter of these degradation modes is of primary concern for the study of white light-emission from blends Chapter 5 as phase separation will increase the average molecular distance between donor and acceptor molecules and hamper the generation of white light.

Xiao et. al. (23) have shown that by endcapping semiconducting polymers with bulky, inorganic groups, such as polyhedral oligomeric silsesquioxanes (POSS), they can improve thermal stability, reduce chain mobility and decrease the formation of aggregates. The lower chain mobility of the endcapped molecules (termed PFO-POSS and MEHPPV-POSS) makes the modified forms of these molecules ideal for studies of polymer blends. PFO-POSS and MEHPPV-POSS are obtained from American Dye Source (Baie D'Urfé, Quebec) and used without further purification. Figure 4-3 shows the chemical structure of these polymers. Both materials are highly soluble in toluene, xylenes, tetrahydrofuran, and chlorobenzene.

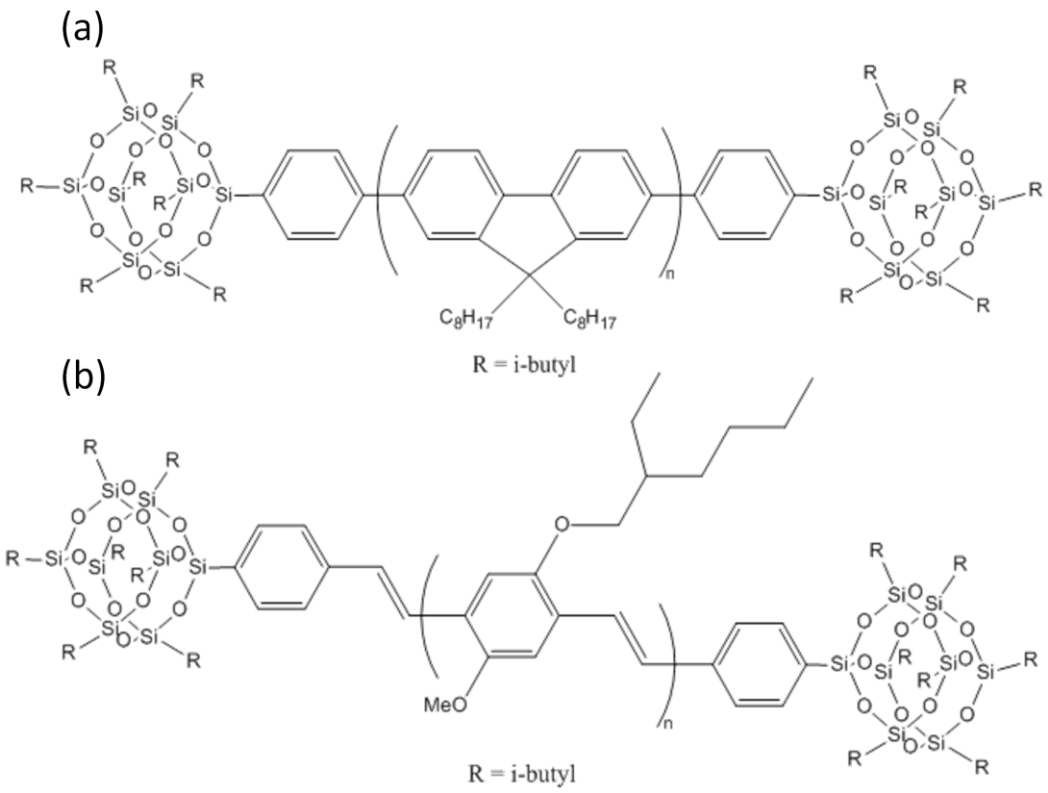

Figure 4-3: Chemical structure of PFO-POSS (a) and MEHPPV-POSS (b).

The absorption of PFO-POSS peaks at about 380nm (3.2 eV) with an absorption onset at 415nm giving an optical gap of 2.99 eV. The photoluminescence spectrum shows peaks at 435nm (2.85 eV), 480nm (2.69 eV), 490nm (2.53 eV) and 510nm (2.43 eV) with a maximum emission at 410nm (3.02 eV). AC voltammetry measurements estimate the HOMO of PFO-POSS to be -5.64 eV and the LUMO to be -2.07 eV giving an electrochemical gap of 3.57 eV. The molecular weight for PFO-POSS, as measured by gel permeation chromatography with a polystyrene standard, is 117,000.

The absorption spectrum of MEHPPV-POSS shows a strong peak at 502nm (2.47 eV) with an absorption onset of 561nm, leading to an optical gap of 2.21 eV. Photoluminescence measurements reveal broad peaks at 560nm (2.21 eV), 590nm (2.11 eV) and 625nm (1.99 eV) with a maximum emission at 486nm (2.55 eV). AC

voltammetry measurements estimate the HOMO of MEHPPV-POSS to be -5.0 eV and the LUMO to be -2.48 eV giving an electrochemical gap of 2.52 eV. The molecular weight for MEHPPV-POSS, as measured by gel permeation chromatography with a polystyrene standard, is 346,000.

For all three molecules, the measured electrochemical gap was larger than the optical gap (F8BT: +1.28 eV, PFO-POSS: +0.58 eV, and MEHPPV-POSS: +0.31 eV). The electrochemical gap represents the amount of energy required to place an additional charge carrier on the molecule, and, hence, is more representative of the barriers to charge diffusion. The large disparity between the measured gaps suggests that there is significant relaxation of the molecule between its oxidized or reduced state and its excited state (with the presence of an exciton on the molecule).

Cathode – Calcium/Silver

In all the PLEDs fabricated for the studies detailed in this thesis, calcium was used as the cathode with a thick silver capping electrode. Calcium is used because it has a low workfunction of 2.87 eV (27) which allows for efficient injection of electrons in to the emissive layer. In addition, it has been shown that Ca produces an efficiency interface with organic semiconductors and that changing the cathode metal to a lower workfunction material has little effect on the device performance (28). Because of its low workfunction, Ca is highly reactive to atmospheric oxidizers. A thick Ag capping layer is used to protect the Ca electrode from deleterious elements during operation. Ag was chosen due to its high conductivity, high reflectivity and compatibility with our deposition tools. The workfunction of Ag is 4.26 eV (27).

Fabrication Procedure

Pre-patterned ITO/glass substrates are obtained from Thin Film Devices (Anaheim, CA). The substrates are 2×2 inch and 0.5mm thick. The anode and cathode masks are designed to fit eight individual devices on to the substrate. Figure 4-4 shows the electrode pattern used in the devices. Figure 4-4 (a) shows the ITO anode pattern as received on the 2×2 inch substrates from Thin Film Devices. Figure 4-4 (b) shows the shadow mask pattern used to deposit the metallic cathode. Figure 4-4 (c) is the overlay of the two electrode patterns. The area of overlap forms the device area. The green region is the area where the organic layers are built up. The masking procedure is described below. The width of the electrodes near the edge of the substrate is 2.5mm. This narrows to 1mm where the device is located, leading to a $1mm^2$ device.

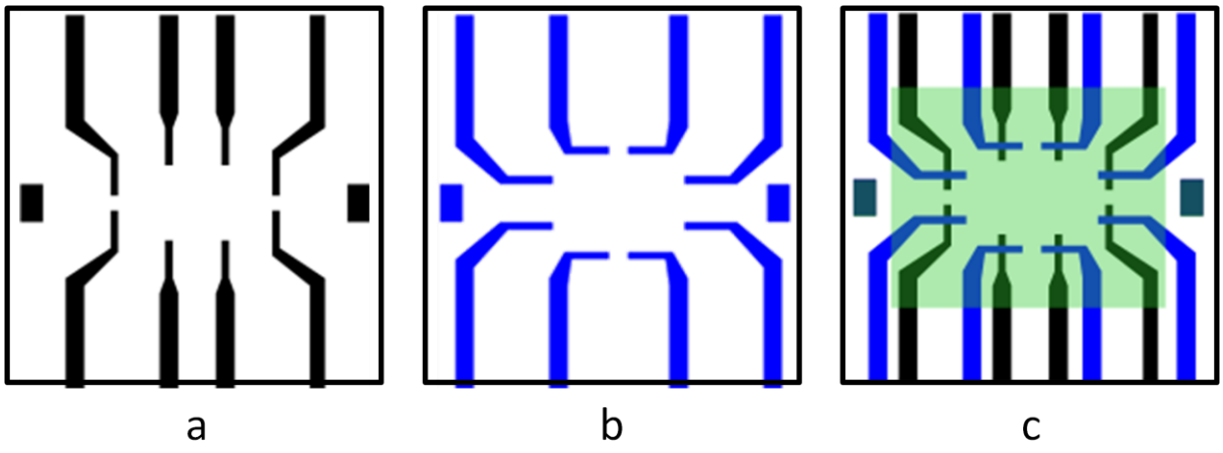

Figure 4-4: (a) ITO anode pattern. (b) cathode pattern. (c) overlay of anode and cathode. Green region shows organic area.

Once received, the substrates are rinsed with acetone, isopropyl alcohol and finally deionized water and dried with nitrogen. The substrate is then placed in a UV-Ozone system from UVOCS, Inc. for twenty minutes. UV-Ozone is an ultraviolet radiation and

oxidation cleaning step. The highly oxidizing radicals formed by the UV exposure strip the surface of contaminating hydrocarbons. Next, using a low tack masking tape, the organic area is defined by covering the electrode contact area and the sides of the device. Aqueous PEDOT:PSS is spun, in lab atmosphere, on the exposed portion of the substrate at 4000 rpm until dry, producing a 40nm thick film. The device is placed in a vacuum oven at 90˚C for at least 90 minutes to remove residual moisture. The device is then transferred to an oxygen-free, moisture-free, nitrogen glove box equipped with a spinner and vacuum oven. The emissive layer (typically dissolved in xylenes) is applied with a syringe-driven filter (0.2μm) and spun cast at 1500 rpm until dry. The device is then baked at 90˚C in a vacuum oven for 120 minutes. After removal from the vacuum oven, the low tack tape is carefully removed exposing the electrode contact area.

The cathode is deposited by thermal evaporation through a shadow mask in an evaporation system connected to the nitrogen glove box. A 100Å thick calcium film is deposited at 0.5 Å/s at a base pressure of ~4×10^{-6} Torr. This is followed by a thick silver capping layer (~4000Å) deposited at 20Å/s with a base pressure of ~4×10^{-6} Torr.

Characterization

Current-Luminance-Voltage Measurement

Current-Luminance-Voltage (ILV) measurements are conducted within the nitrogen atmosphere glove box, allowing for the fabrication and characterization of devices in an inert environment. An ILV measurement traces the luminous output of the device and the current drawn through the device as a function of the applied voltage. A schematic

of the measurement system is shown in Figure 4-5. The Labview-controlled computer is connected to a Keithly 2400 sourcemeter via GPIB. Positive and negative leads from the sourcemeter are passed through the wall of the glovebox via BNC connectors and attached to the device under test via "toothless" alligator clips. The OLED is mounted at the entrance port of a calibrated International Light integrating sphere. The sphere is fitted with a photopically filtered silicon photodetector connected to an IL1700 from International Light. Cables leading from the photodetector to the IL1700 were modified to fit the glove box's BNC passthoughs. The IL1700 is calibrated to display the detected signal as lumins and is connected via serial cable to the computer. Using user-imputed device dimensions, the labview routine converts the reported lumin value to candelas/m^2 and output all values as a text file.

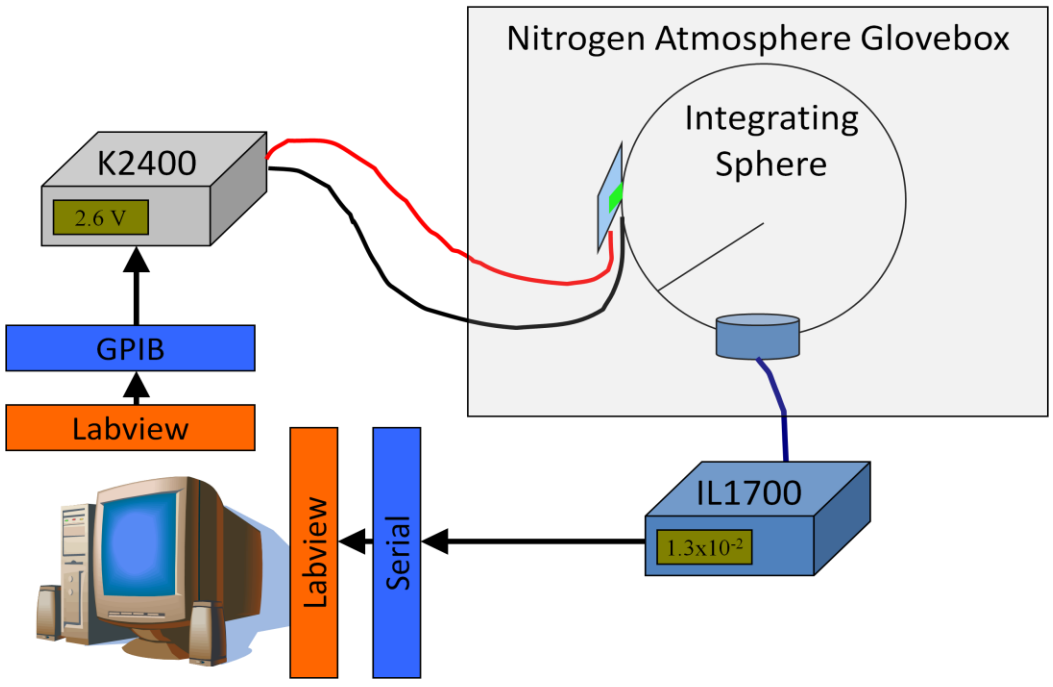

Figure 4-5: ILV measurement system schematic

Electroluminescence Measurement

The device electroluminescence (EL) spectrum is measured outside the nitrogen atmosphere, although future studies should consider incorporating the EL system in to the glove box. Figure 4-6 show the schematic diagram for the EL measurement system used. The OLED is mounted to the entrance port of an integrating sphere and connected to a power supply via "toothless" alligator clips. Collection optics are mounted at the exit port of the sphere, and focus incident light on the end of a fiber optic cable. The fiber optic cable leads to a Triax 190 monochromater fitted with a liquid nitrogen-cooled CCD unit from Horiba Jobin-Yvon. The spectral images are relayed to a computer and outputted as a data file.

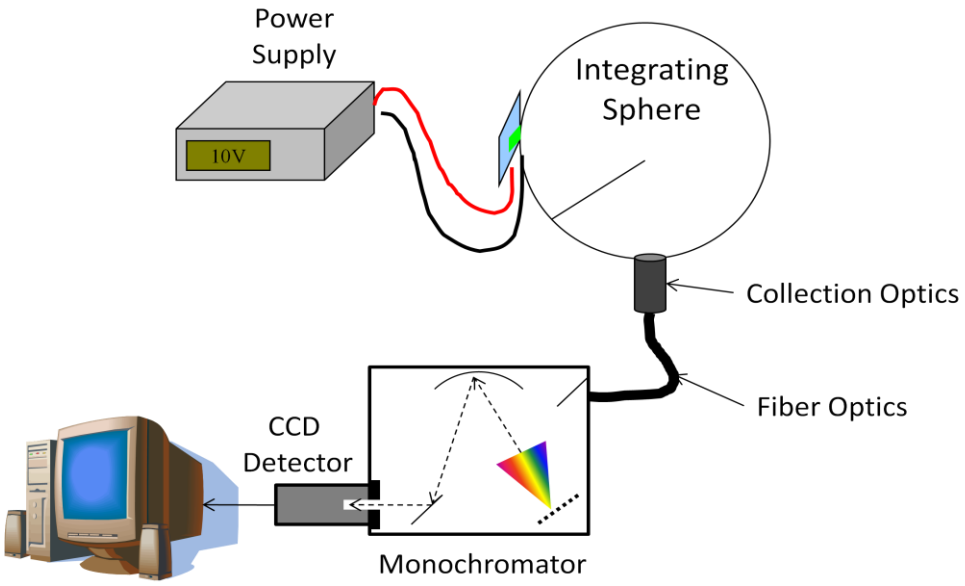

Figure 4-6: EL measurement system schematic

Lifetime

The lifetime measurement system is design to record luminance, current and emission area as a function of time under constant bias. For measurements, the OLED is placed in an environmental chamber. During operation, the chamber can be flooded with house

nitrogen, evacuated or left open for exposure to lab air, depending on the type of measurement being performed. When the chamber is closed, a quartz window allows observation of the device. When the device is to be exposed to lab air, the cover is removed. Within the chamber, the device under test is connected to a Keithley 2400 sourcemeter via pass-throughs in the chamber wall. The bias voltage remains constant throughout the measurement, and the current through the device is recorded. A small portion of the emitted light is diverted to a silicon photodiode connected to an uncalibrated IL1700. Photodiode current is recorded by the computer. A CCD camera is positioned above the device to image the emission area of the device while operating. From these images, the effective device area is calculated using a procedure described below. For each measurement, the computer records a timestamp so that luminance, current, effective current density and effective device area can be plotted as a function of elapsed time.

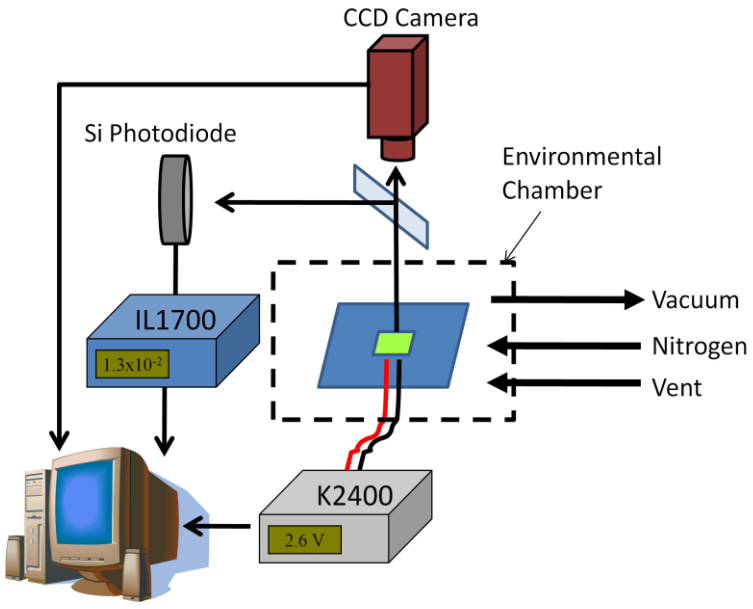

Figure 4-7: Schematic of DC lifetime measurement system

An AC lifetime measurement setup can be accomplished by substituting the Keithley DC source for a HP8114a pulse generator with a buffered output and substituting the IL1700 radiometer with a Lecroy oscilloscope. Such a measurement setup is shown in figure Figure 4-8.

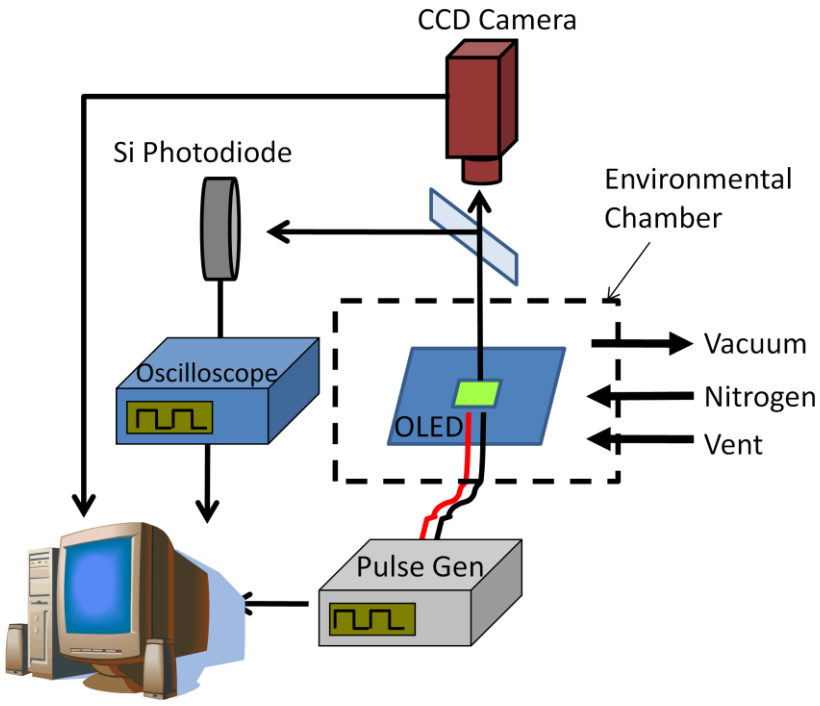

Figure 4-8: Schematic of AC lifetime measurement system

During operation and under constant exposure to atmospheric moisture and oxygen, OLED cathodes will degrade leading to the formation and growth of non-emissive, dark spots (29)(30). The rate of growth of these dark spots is directly related to the flux of moisture and oxygen to the cathode/organic interface. The normalized effective area of the device is that percentage of the device area not consumed by the growing dark regions. Experimentally, this is measured via analysis of images taken of the device over the course of the lifetime experiment. For each measurement, the recorded image is converted to an 8-bit grayscale matrix. A histogram of these images shows two distinct

regions. The grayscale image and histogram are shown in Figure 4-9. Pixels representing dark spot area and the non-luminescent area around the device have values close to zero while pixels representing the actively emitting area of the device have higher values. Based on the histogram, a threshold value can be defined and the pixels can be binned in to one of two categories: *on* pixels (pixels whose grayscale value is above the threshold) and *off* pixels (pixels whose grayscale value is below the threshold). This is done for each image taken and the sum of the *on* pixels is normalized to the t=0 value.

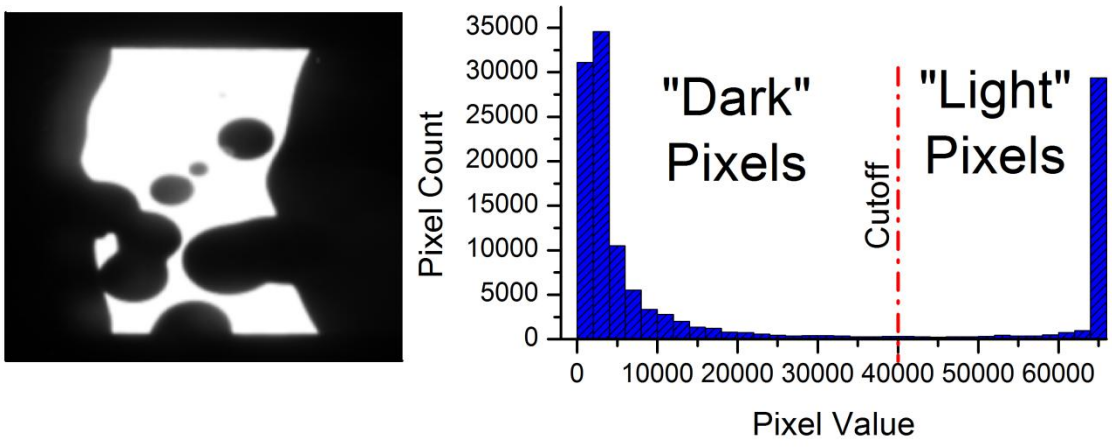

Figure 4-9: 8-bit grayscale image of OLED emission after some degradation due to dark spot growth. The histogram of the image (right) allows the area of the emissive region to be calculated.

Some error is introduced in to this procedure from the response of the CCD camera and the changing luminance of the device. As the device ages, the total luminance decreases for reasons independent of the dark spot growth. With no change in the camera gain or shutter speed, this dimming results in a lowering of the image contrast. While the contrast between the emitting area and the dark regions remains sufficiently high to determine a threshold value, the decrease in contrast increases the apparent

area of transition regions, such as the device edge and the edge of the dark regions where there is a gradation of grayscale values. As a consequence, some *on* pixels shift to the *off* bin, confounding an exact measurement of the area. In short, two images taken of the same emission area, but under high and low contrast conditions will register slightly different effective areas (high contrast images registering higher area and low contrast images registering lower area).

This contrast dependent error is minimized by taking steps to homogenize the contrast of images. This is done using software provided with the camera to automatically adjust the shutter time and gain such that the illuminated area of the device is uniform in intensity among images. Post-measurement image processing is used to subtract background and stray light, leading to more uniform among the collected images. Regardless, effective area measurements should not be taken as an absolute measurement, but should be considered approximations within ±2%.

CIE calculation

The chromaticity of OLED emissions is characterized with the CIE 1931 XYZ color space (31)(32)(33). The CIE 1931 XYZ color space is based on observer color matching data and is defined by three color matching functions, $\bar{x}(\lambda)$, $\bar{y}(\lambda)$, and $\bar{z}(\lambda)$ shown in Figure 4-10. Because the human eye has three light receptors, roughly corresponding to short, medium and long wavelength photons, the perception of color can be expressed with three values:

$$X = \int I(\lambda)\bar{x}(\lambda)d\lambda$$
$$Y = \int I(\lambda)\bar{y}(\lambda)d\lambda \quad (4\text{-}1)$$
$$Z = \int I(\lambda)\bar{z}(\lambda)d\lambda$$

where $I(\lambda)$ is the spectrum of the emission or stimulus. In this thesis, CIE coordinates are expressed using the xyY formulation of the 1931 color space. This formulation takes advantage of the fact that the $\bar{y}(\lambda)$ was specifically chosen to represent the luminance of the stimulus. Thus, the xyY formulation separates the chromaticity and brightness, allowing a color to be expressed as with two values, x and y, according to

$$x = \frac{X}{X + Y + Z} \quad (4\text{-}2)$$
$$y = \frac{Y}{X + Y + Z}$$

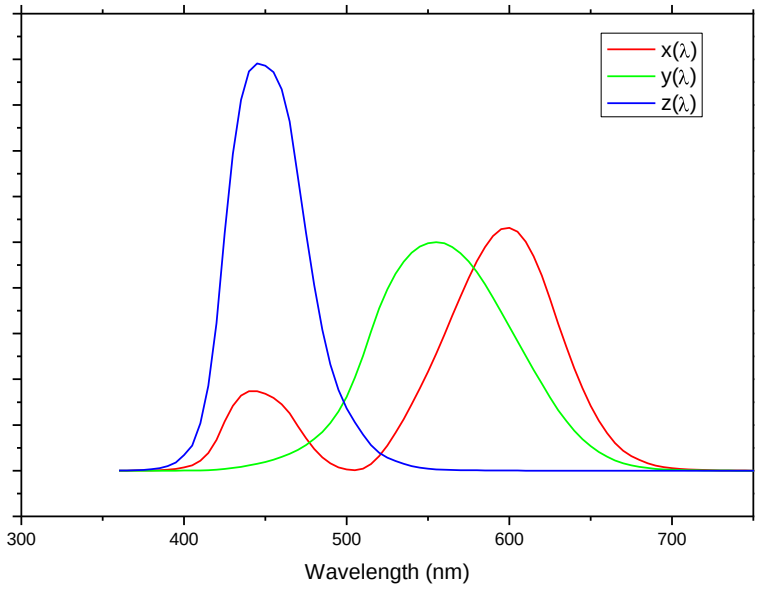

Figure 4-10: Standard observer functions for CIE 1931 XYZ color space

OLED Fabrication and Discussion

PLEDs were fabricated using the procedure outlined above. The ILV and electroluminescence spectra are discussed below. Lifetime measurements are discussed in Chapters 6 and 7.

Figure 4-11 show the typical ILV characteristics for a PLED fabricated using F8BT as the emissive layer. F8BT was spin cast from a 10mg/mL solution in xylenes. The typical device shows a maximum luminance of 11,500 cd/m^2 at about 9.8V. The turn-on voltage (voltage which produces 1 cd/m^2) is 2.3V. F8BT shows very high efficiency. The maximum emission efficiency is 1.96 cd/A and the maximum power efficiency is 2.27 lm/W

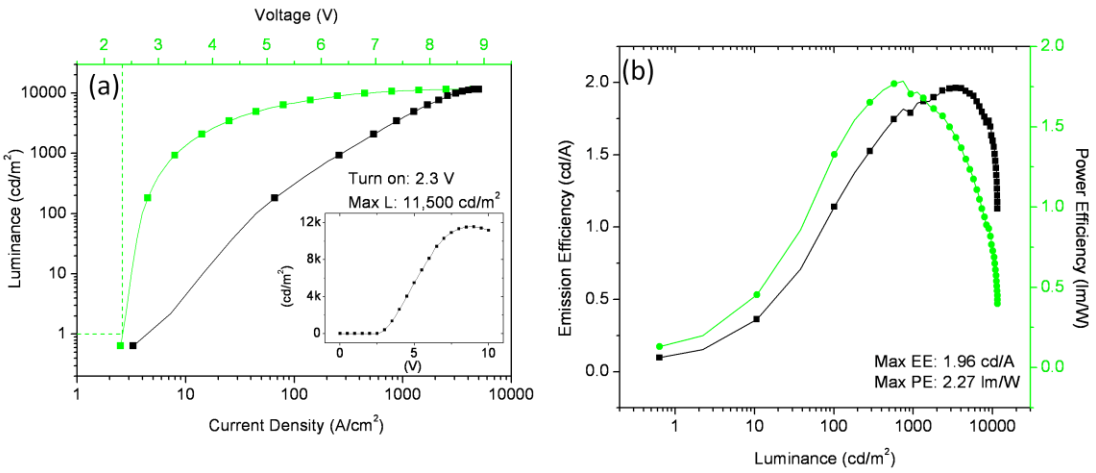

Figure 4-11: Typical ILV characteristics for PLED with F8BT emission layer

Figure 4-12 shows the ILV characteristics for a typical PLED fabricated with a PFO-POSS emission layer. The PFO-POSS was cast from a 12 mg/mL solution in xylenes. This device shows a much lower maximum luminance than the F8BT device with only 210 cd/m^2 at about 17.5V. This value is deceptive, however, since this maximum is the

result in a spike in luminance observed as the bias is increased. Beyond 17.5 V, the device undergoes a catastrophic failure. It is unlikely that without further optimization of the device structure, that this output could be maintained for prolonged periods of time. The turn-on voltage for this device is 11.3 V. As can be expected from the relatively low luminance as compared to the F8BT device, the efficiency of the PFO-POSS device is low, showing a maximum emission efficiency of 0.057 cd/A and a maximum power efficiency of 0.011 lm/W.

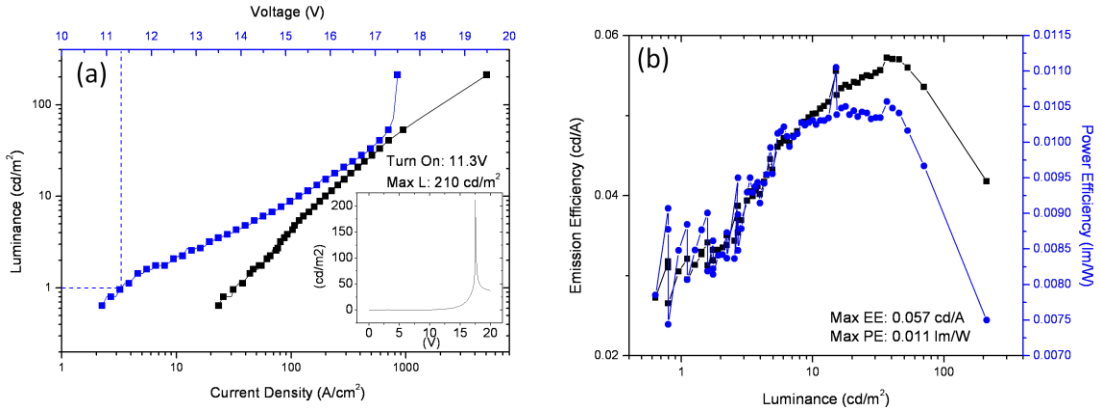

Figure 4-12: Typical ILV characteristics for PLED with PFO-POSS emission layer

Figure 4-13 shows the typical ILV characteristics for a PLED fabricated with a MEHPPV-POSS emission layer. The emission layer was cast with a 10 mg/mL solution in xylenes. The MEHPPV-POSS device has a maximum luminance of 345 cd/m2 at about 15V. The turn-on voltage is 7.7 V. These devices typically yield a maximum emission efficiency of 0.288 cd/m^2 and a maximum power efficiency of 0.076 lm/W.

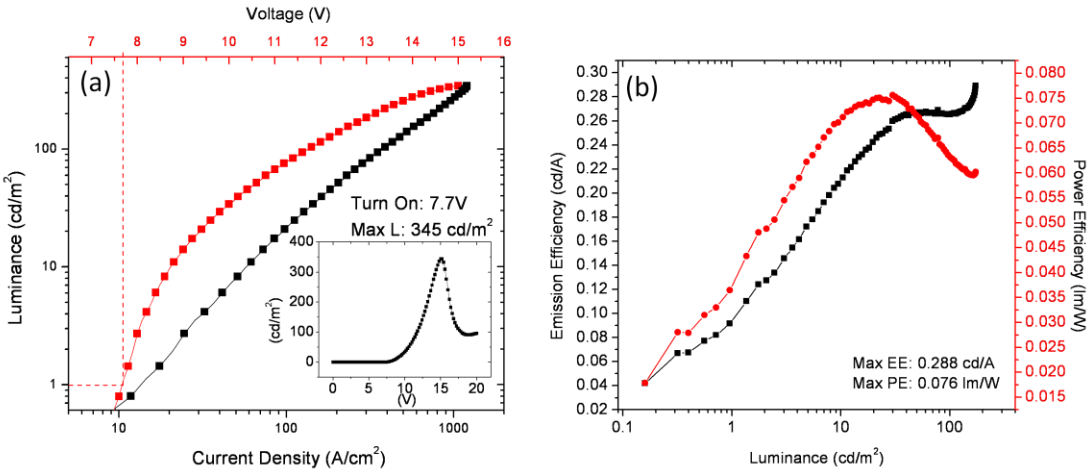

Figure 4-13: Typical ILV characteristics for PLED with MEHPPV-POSS emission layer

Figure 4-14 shows the emission spectrum of the previous devices. The photoluminescence spectra are plotted along the same graph for comparison. There is very good agreement between the PL and EL spectra for F8BT. The wider emission of the EL spectrum is most likely due to the difference in detectors as the EL was measured using a CCD and the PL with a photodiode. The EL spectrum of the PFO-POSS (b) exhibits four narrow peaks in good agreement with the positions of the peaks in the PL spectrum, albeit with the relative intensities of each peak altered. The EL spectrum of the MEHPPV-POSS devices shows three broad peaks in good agreement with the PL spectral peaks, but, again, with the relative intensities altered.

It should be noted that the reported power efficiencies for the F8BT-, PFO-POSS-, and MEHPPV-POSS-based OLEDS are well below the efficiency goal set by the DoE (Chapter 1) as well as below the state of the art device currently reported in the literature. This should not be construed as an inherent deficiency in the materials and methods discussed in this thesis. Rather, it should be noted that no effort has been made to

mitigate the various factors which limit device efficiency. For instance, fluorescent molecules typically have a maximum internal efficiency of 25% (greater for polymers) due to the limitation that only singlet transitions (which constitute only 25% of excited electronic states) may emit (34). The internal efficiency of the device may be increased by either doping the host material with a phosphorescent material (35) or replacing the fluorescent material with a phosphorescent one (34). Both solutions will take advantage of the populous triplet excited state leading to internal efficiencies close to unity (36). In addition, up to 80% of the emitted light can be lost to external factors such as waveguiding through the transparent substrate (37). No effort was made in these studies to try to reclaim this lost luminance.

The CIE coordinates were found to be (0.17, 0.09), (0.55, 0.45), and (0.39, 0.57) for F8BT, PFO-POSS and MEHPPV-POSS, respectively.

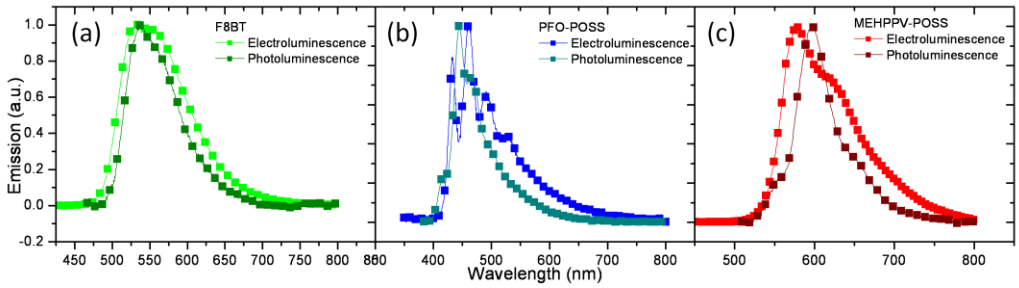

Figure 4-14: Electroluminescent spectra compared to photoluminescent spectra of F8BT device (a), PFO-POSS device (b), and MEHPPV-POSS device (c)

Conclusions

The materials and device structures were chosen to provide an appropriate and simple test platform for the measurements to be described in the following chapters. Devices

fabricated with an F8BT emission layer have high brightness and efficiency, making them ideal for studies of lifetime and packaging. Devices fabricated with PFO-POSS and MEHPPV-POSS emit spectra which allow the fabrication of white illumination, while their bulky endgroups diminish chain mobility, inhibiting phase separation in blends of these polymers.

Bibliography

[1] Zhao, J, Xie, S., Han, S., Yang, Z., Ye, L., Yang, T., *Organic light-emitting diodes with AZO films as electrodes. Synth. Met.*, Vol. 114, p. 251, (2000)

[2] Chen, C.-W., Hsieh, P.-Y., Chiang, H.-H., Lin, C.-L., Wu, H.-M., Wu, C.-C., *Top-emitting organic light-emitting devices using surface-modified Ag anode. App. Phys. Lett.*, Vol. 83, p. 5127, (2003)

[3] Vaufrey, D., Khalifa, M. B., Tardy, J., Ghica, C., Blanchin, M. G., Sandu, C., Roger, J. A., *ITO-on-top organic light-emitting devices: a correlated study of opto-electronic and structural characteristics. Semicond. Sci. Technol.*, Vol. 18, p. 253, (2003)

[4] Chen, C.-W., Lin, C.-L., Wu, C.-C., *An effective cathode structure for inverted top-emitting organic light-emitting devices. Appl. Phys. Lett.*, Vol. 85, p. 2469, (2004)

[5] Wu, Z., Chen, S., Yang, H., Zhao, Y., Hou, J., Liu, S., *Top-emitting organic light-emitting devices based on silicon substrate using Ag electrode. Semicond. Sci. Technol.*, Vol. 19, p. 1138, (2004)

[6] Jeong, J. K., Jin, D. U., Shin, H. S., Lee, H. J., Kim, M., Ahn, T. K., Lee, J., Mo, Y. G., Chung, H. K., *Flexible full-color AMOLED on ultrathin metal foil. IEEE Elec. Dev. Lett.*, Vol. 28, p. 389, (2007)

[7] Lee, C.-J., Moon, D.-G., Han, J.-I., *Top emission organic EL display on paper substrate.* 2004. SID04 Digest. Vol. 2004, p. 1005.

[8] Nakamura, Y., Ikeda, H., Ohara, H., Ishitani, T., Hirakata, Y., Yamazaki, S., Ishii, A., Ohshima, T., Kodaira, T., Kawashima, H., Sato, K., *2.1-inch QCIF+ Dual Emission AMOLED Display having Transparent Cathode Electrode.* 2004. SID04 Digest. Vol. 04, p. 1403.

[9] Lee, H., Johnson, A. R., Kanicki, J., *White LED Based on Polyfluorene Co-Polymers Blend on Plastic Substrate. IEEE Trans. Elec. Dev.*, Vol. 53, p. 427, (2006)

[10] Shen, F., He, F., Lu, D., Xie, Z., Xie, W., Ma, Y., Hu, B., *Bright and Colour stable while polymer light-emitting diodes. Semicond. Sci. Technol.*, Vol. 21, p. L16, (2006)

[11] Antoniadis, H., Lui, M. W., *Passive matrix displays based on light emitting polymers.* s.l. : IMID, 2004. Workshop Digest fo Asia Display. Vol. 04, p. 1.

[12] Riel, H., Karg, S., Beierlein, T., Ruhstaller, B., ReiB, W., *Phosphorescent top-emitting organic light-emitting devices with improved light outcoupling. Appl. Phys. Lett.*, Vol. 82, p. 466, (2003)

[13] Smith, L. H., Wasey, J. A. E., Barnes, W. L., *Light outcoupling efficiency of top-emitting organic light-emitting diodes. Appl. Phys. Lett.*, Vol. 84, p. 2986, (2004)

[14] Hong, Y., Nahm, J.-Y., Kanicki, J., *100 dpi 4-a-Si:H TFTs Active-Matrix Organic Polymer Light-Emitting Display. IEEE JSTQE*, Vol. 10, p. 16, (2004)

[15] He, Y., Kanicki, J., *High-efficiency organic polymer light-emitting heterostructure devices on flexible plastic substrates. App. Phys. Lett.*, Vol. 76, p. 661, (2000)

[16] Gu, G., Bulovic, V., Burrows, P. E., Forrest, S. R., Thompson, M. E., *Transparent organic light emitting devices. Appl. Phys. Lett.*, Vol. 68, p. 2606, (1996)

[17] Vankatesan, M., McGee, S., Mitra, U., *Indium Tin Oxide Thin Films for Metallization in Microelectronic Devices. Thin Solid Films*, Vol. 170, p. 151, (1989)

[18] Onisawa, K.-I., Nishimura, E., Ando, M., Takabatake, M., Minemura, T., *Resitivity increase after crystallization of amorphous Indium-Tin Oxide thin films prepared by DC magnetron sputtering at room temperature with H2O addition.* Osaka : SID, 1995. Digest of Technical Papers. Vols. AM-LCD95, p. 137.

[19] Kim, J.-S., Ho, P. K. H., Murphy, C. E., Baynes, N., Friend, R. H., *Nature of non-emissive black spots in Polymer Light-Emitting Diodes by In-Situ Micro-Raman Spectroscopy. Adv. Mater.*, Vol. 14, p. 206, (2002)

[20] Halls, J. J. M., Arias, A. C., MacKenzie, J. D., Wu, W., Inbasekaran, M., Woo, E. P., Friend, R. H., *Photodiodes Based on Polyfluorene Composites: Influence of Morphology. Adv. Mater.*, Vol. 12, p. 498, (2000)

[21] Hong, Y., Hong, Z., Kanicki, J., *Materials and Device Structures for High Performance Poly OLEDs on Flexible Plastic Substrates.* 2001. Proceedings of SPIE. Vol. 4105, p. 356.

[22] Ahn, J. H., Wang, C., Pearson, C., Bryce, M. R., Petty, M. C., *Organic light-emitting diodes based on a blend of poly[2-(2-ethylhexyloxy)-5-methoxy-1,4-phenylenevinylene] and an electron transporting material. Appl. Phys. Lett.*, Vol. 85, p. 1283, (2004)

[23] Xiao, S., Nguyen, M., Gong, X., Cao, Y., Wu, H., Moses, D., Heeger, A. J., *Stabilization of Semiconducting Polymers with Silsesquioxane. Adv. Func. Mater.*, Vol. 13, p. 25, (2003)

[24] Zhang, M., Lu, P., Tian, L. L., Zhang, W., Yang, B., Ma, Y. G., *Study of the fluorescent conjugated polymers on metal ion sensing. ACTA PHYSICO-CHIMICA SINICA*, Vol. 20, p. 924, (2004)

[25] Heeger, P. S., Heeger, A. J., *Proc. Natl. Acad. Sci. USA*, Vol. 96, p. 12219, (1999)

[26] Yu, G., Gao, J., Hummelen, J. C., Wudl, F., Heeger, A. J., *Polymer photovoltaic cells - enhanced efficiencies via a network of internal donor-acceptor heterojunctions . Science*, Vol. 270, p. 1789, (1995)

[27] Michaelson, H., *Relation Between an Atomic Electronegativity Scale and the Work Function. IBM J. Res. Dev.*, Vol. 22, p. 72, (1978)

[28] Bernius, M. T., Inbasekaran, M., O'brian, J., Wu, W., *Progress with light-emitting polymers. Adv. Mater.*, Vol. 12, p. 1737, (2000)

[29] Nagai, M., *Defects of Passivation Films for Color-Filter-based OLED Devices. J. Electrochem. Soc.*, Vol. 154, p. J65, (2007)

[30] Nagai, M., *Dark Spot formation and growth in color-filter-based OLED devices. J. Electrochem. Soc.*, Vol. 154, p. J116, (2007)

[31] Wright, W. D., *A re-determination of the trichromatic coefficients of the spectral colours. Transactions of the Optical Society*, Vol. 30, p. 141, (1928)

[32] Guild, J., *The colorimetric properties of the spectrum. Philosophical Transactions of the Royal Society of London*, Vol. A230, p. 149, (1931)

[33] CIE, *Publication No. 25, Procedures for the Measurement of Luminous Flux of Discharge Lamps and for Their Calibration as Working Standards.* Vienna, Austria : Central Bureau of the CIE, 1973.

[34] Baldo, M. A., O'Brien, D. F., You, Y., Shoustikov, A., Sibley, S., Thompson, M. E., Forrest, S. R., *Highly efficient phosphorescent emission from organic electroluminescent devices. Nature*, Vol. 395, p. 151, (1998)

[35] Baldo, M. A., Thompson, M. E., Forrest, S. R., *High-efficiency fluorescent organic light-emitting devices using a phosphorescent sensitizer. Nature*, Vol. 403, p. 750, (2000)

[36] Adachi, C., Baldo, M. A., Thompson, M. E., Forrest, S. R., *Nearly 100% internal phosphorescence efficiency in an organic light-emitting device. J. Appl. Phys.*, Vol. 90, p. 5048, (2001)

[37] Chen, W., Li, G., Wu, F., *Light extraction frmo organic light emitting diode.* 2007. Proceedings of SPIE. Vol. 6722, p. 672241.

Chapter 5
White Light Emission from Emissive Polymer Blends

Introduction

The prospect of viable polymer-based solid-state lighting and display backlights has spurred interest in blends of semiconducting polymers to be used as the emissive layer in polymeric light-emitting devices (PLEDs). In contrast to devices which rely on multiple emission layers to produce white light (1), single emission layer utilize efficient energy transfer (Förster transfer) from a donating molecule (ubiquitously a blue emitter) to a accepting molecule (either a red or a blend of red and green emitters) to generate the broad spectrum emission. The goal of such blends is to produce a white emission, characterized by the CIE (Commission Internationale d'Eclairage) coordinates of (0.33, 0.33). The CIE coordinates are highly sensitive to the emission characteristics of constituent polymers which can be altered by bimolecular interactions among the various polymers, such as Förster energy transfer and exiplex formation. Hence, the effect of these heterodimeric interactions on the CIE coordinates of the overall emission is a research effort of great interest.

Of the possible donating host materials, blue-emitting poly-fluorene (PF) and its many derivatives and copolymers are widely used in white-emitting blends due to PF's high

photoluminescent efficiency, good hole mobility, thermal stability and variability of chemical properties. A wide range on PF-based systems can be realized. We have previously shown high luminance and efficiency from white-emitting devices based on red and blue polyfluorene copolymers (2). Virgili et. al. have fabricated light-emitting devices using a blend of PF and a red-emitting small molecule, tetraphenylporphyrin (3). Efficient Förster transfer from the PF to the porphyrin is suggested by the low weight percent (0.15%) of porphyrin needed to produce sufficient red emission. Gong et. al. have produced highly efficient white PLEDs with a blend of PFs with a phosphorescent small molecule, tris[2,5-bis(9,9-dihexylfluoren-2-yl)pyridine-κ2NC3]iridium-(III),Ir(HFP)3 (4). Liu et. al. produce white emission from a blend of polyfluorene and a benzothiadiazole derivative(5). Shen et al. produce stable white emission from PLEDs with emissive layers consisting of blends of poly(fluorene) (PFO) and poly(2-(2'-ethylhexyloxy)-5-methoxy-1,4-phenylenevinylene) (MEHPPV)(6).

We produce similar white light-emitting OLEDs from blends of blue- and red-emitting fluorescent polymers, with a polyfluorene-based donor material and poly phenylenevinylene-based acceptor. Clearly, efficient Förster transfer is, as it is in the previously mentioned examples, a crucial process in the generation of white light, the production of which requires a critical ratio of emitting materials. To better understand the energy transfer characteristics of our emissive materials, we examine the efficiency of Förster transfer in donor-acceptor blends as a function of solution concentration and donor to acceptor ratio by employing an adaptation of the method proposed by Epe et. al. (7) in which fluorophores are separated by diluting solutions of fixed ratios of donor

and acceptor molecules and the resultant emission is decomposed by means of a simple curve-fitting routine which uses the fluorescence of the individual polymers as a reference. We then determine the specific increase in efficiency this blending method affords as compared to a trivial solution of using two emissive samples to produce white light.

Förster Transfer

Förster transfer, also known as resonant energy transfer, is the radiationless transfer of energy from an excited molecule to a ground state molecule. It is important to note the Förster transfer does not involve the emission of a photon (as in reabsorption), the formation of a bimolecular complex, or collision between excited species. There are five condition for the efficient transfer of energy by the Förster process (8):

1. There is sufficient overlap between the donor molecule's emission spectrum and the acceptor molecules absorption spectrum.
2. The average donor-acceptor distance must be sufficiently small
3. The donor and acceptor chromophores must be in reasonable mutual alignment
4. The electronic transitions of both molecules must be in the near ultraviolet to near infrared range.
5. Both materials must have sufficiently high quantum yields.

The degree to which a system of molecules meets these criteria determines the efficiency by which Förster transfer occurs. For blends of donors (D) and acceptors (A) which meet or partially meet the above criteria, excitation of the donor molecule by means of photon absorption leads to a number of processes.

$$D + A + h\nu \rightarrow D^* + A \quad \begin{matrix} (a) \xrightarrow{k_T} D + A^* \\ (b) \xrightarrow{k_r} D + A + h\nu \\ (c) \xrightarrow{k_{nr}} D + A \end{matrix} \tag{5-1}$$

In process (a) of the above equation, the excitation is resonantly transferred from the donor to the acceptor at a rate of k_T. The acceptor then decays radiatively or nonradiatively according to its quantum efficiency. In process (b), no resonant transfer occurs and the donor decays radiatively at a rate of k_r. In process (c), neither the donor or acceptor decay radiatively, which occurs at a rate of k_{nr}.

The efficiency of Förster energy transfer, E, is defined as the fraction of donor excitations which are transferred to the acceptor material. This can be expressed as:

$$E = \frac{k_T}{k_r + k_{nr} + k_T} \tag{5-2}$$

Förster efficiency is usually observed as a decrease in donor luminance, due to the transfer of the excitation to the acceptor(8). This can, alternatively be expressed as:

$$E = \frac{1}{1 + (r/R_0)^6} \tag{5-3}$$

where r is the average distance between donor and acceptor molecules and R_0 is the characteristic distance at which the energy transfer efficiency is 50% and typically is in the range of 2 to 10 nm (9). It is clear that the efficiency of Förster transfer is highly dependent on the average molecular spacing. In this formulation, R_0 contains all the relevant information regarding the five criteria and is defined as:

$$R_0^6 = \frac{9000(\ln 10)\kappa^2 \eta_D J}{128\pi^5 n^4 N_{AV}} \tag{5-4}$$

where κ^2 is the orientation factor (~2/3 for randomly oriented polymers), η_D is the quantum efficiency of the donor molecule, J is the overlap integral, n is the index of refraction for the medium, and N_{AV} is Avogadro's number.

This well studied metric is used in a number of applications (8)(10) to determine the average separation between fluorophores. Experimentally, E can be expressed as the quenching of donor luminescence in the presence of the acceptor via (11)(12). Rewriting Equation (5-3), E is expressed as:

$$E = 1 - \frac{\eta_{DA}}{\eta_D} \tag{5-5}$$

where η_{DA} is the PL quantum efficiency of the donor in the blend and η_D is the PL quantum efficiency of the donor alone.

Such a measurement can be made by measuring the efficiency of the donor molecule alone, then measuring the efficiency of the blend emission and differentiating the emission of the donor from that of the acceptor. For molecular systems where the emission emissions of the molecules occupy distinct ranges of the spectrum, this is a trivial matter.

In the case of molecular systems where the emissions of the donor and acceptor molecules are wide and overlap slightly, differentiating the source of the emission in the overlap region is difficult, and η_{DA} cannot be measured directly. All of the molecular systems observed in this study were of this nature. To overcome this, we employ a simple curve-fitting routine on the collected spectra of blends. The spectra of the donor and acceptor molecules, individually, are decomposed in to a sum of Gaussian peaks. These reference peaks represent vibrational modes and distinct fluorophores along the

polymer chain. The peaks from both donor and acceptor spectra are used to fit the measured spectra from the blends. Once fitted, the individual emissions from the donor and acceptor can be reconstructed by arithmetically separating the appropriate groups of peaks. In this manner, the fractional contributions of the donor and acceptor emissions can be determined as a ratio. As such, the fractional contribution of the donor emission ($\mathrm{H_D}$) in the blend is given by

$$\mathrm{H_D} = \frac{\phi_\mathrm{D}}{(\phi_\mathrm{D} + \phi_\mathrm{A})} \tag{5-6}$$

where ϕ_D and ϕ_A are the photon fluxes of the donor and acceptor within the blend (determined via the method described above), such that $\phi = \phi_\mathrm{D} + \phi_\mathrm{A}$, where ϕ is the total photon flux of the blend emission. If the absorption of the acceptor is low relative to that of the donor (from a combination of low extinction coefficient and low concentration), the quantum efficiency of the donor in the presence of the acceptor, η_{DA}, can be determined as the ratio between ϕ_D and the number of absorbed photons. This allows us to rewrite equation 1 with measurable quantities:

$$E = 1 - \frac{\mathrm{H_D} \times \eta_B}{\eta_D} \tag{5-7}$$

where η_B is the PL quantum efficiency of the donor-acceptor blend. In our studies, the PL quantum efficiency of the individual donor and acceptor samples and the blends were measured via a calibrated spectrometer utilizing an integrating sphere to establish the absolute photon flux. Details of this experimental setup are presented in Chapter 3.

Förster transfer in PFO-MEHPPV systems

The blue-emitting donor material used in this study was poly(9,9-dioctylfluorenyl-2,7-diyl) end-capped with polyhedral oligomeric silsesquioxane (PFO-POSS), shown in Figure 5-1(a). The red-emitting acceptor material used was poly(2-methoxy-5-(2-ethylhexyloxy)-1,4-phenylenevinylene) also end-capped with silsesquioxane (MEHPPV-POSS) and shown in Figure 5-1(b). Estimates for the HOMO and LUMO values were made electrochemically via AC voltammetry. HOMO and LUMO levels are shown in Figure 5-1 (c).

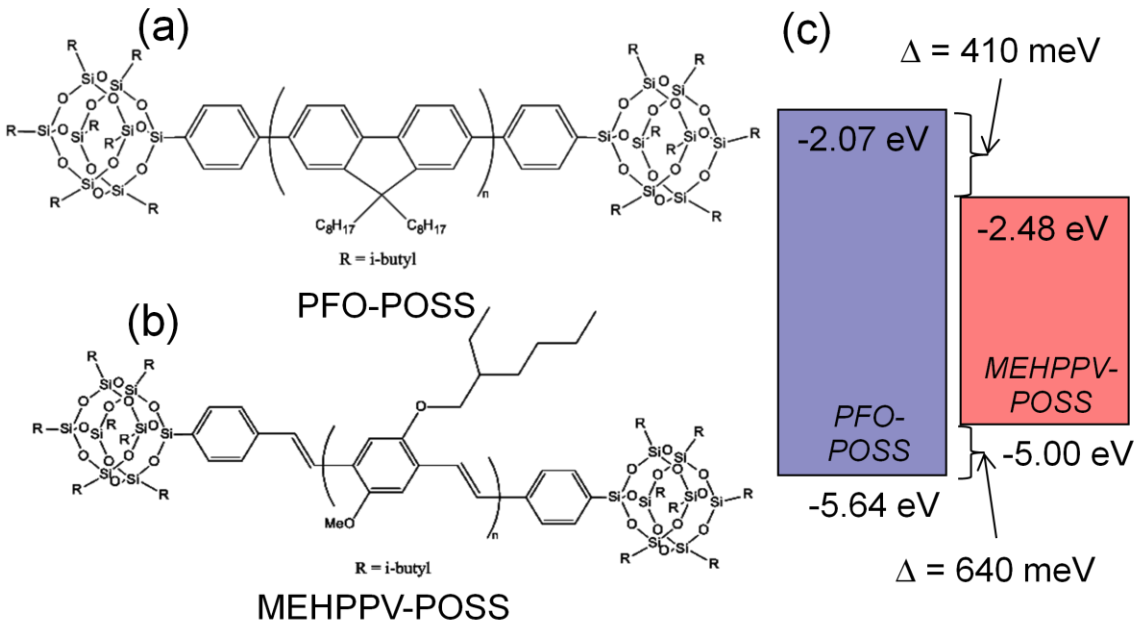

Figure 5-1: Chemical schematic of poly[9,9-dioctylfluorenyl-2,7-diyl] (PFO) end-capped with polyhedral oligomeric silsesquioxane (a) and poly[2-methoxy-5-(2-ethylhexyloxy)-1,4-phenylenevinylene] also end-capped with polyhedral oligomeric silsesquioxane. (c) Energy level diagram of the donor acceptor system. HOMO and LUMO values taken from AC voltammetry measurements.

Solutions in xylenes of donor-acceptor blends with fixed molar ratios of 99.9:0.1, 99.5:0.5 and 99:1 were prepared by combining appropriate volumes of dilute solutions of each. Several samples of varying concentration ranging from 10^{-9} to 10^{-4} M were prepared for each ratio. The calibrated spectra (in $photons \cdot s^{-1} \cdot nm^{-1}$) were taken

and the PL quantum efficiency was calculated. The calibrated spectra for dilute solutions of the donor and acceptor molecules alone are also collected and the PL quantum efficiency is calculated.

The quenching of donor emission is observed by noting its fractional decrease with respect to the total blend emission as the total molar concentration of the solution increases and as the relative concentration of the red increases. The Förster transfer efficiency can be calculated as a function of average molecular spacing by proxy of solution concentration and donor-acceptor ratio.

Figure 5-2 shows the absorption and photoluminescence spectra for the donor (a) and acceptor (b) materials. The absorption spectrum for the blue donor shows a single peak at 388 nm (3.19 eV). This optical gap is 0.53 eV smaller than the measured electrochemical gap. A decomposition of the photoluminescence of the blue donor shows four total peaks. The absorption spectrum of acceptor has a single peak centered at 502 nm (2.47 eV), which is 0.05 eV smaller than the measured electrochemical gap. The photoluminescence spectrum is decomposed in to three peak, the highest energy of which is centered at 599 nm (2.21 eV). The fitted Gaussian peaks are plotted as well. The relative positions of these peaks are used to identify the origin of emissive peaks in blends of polymers.

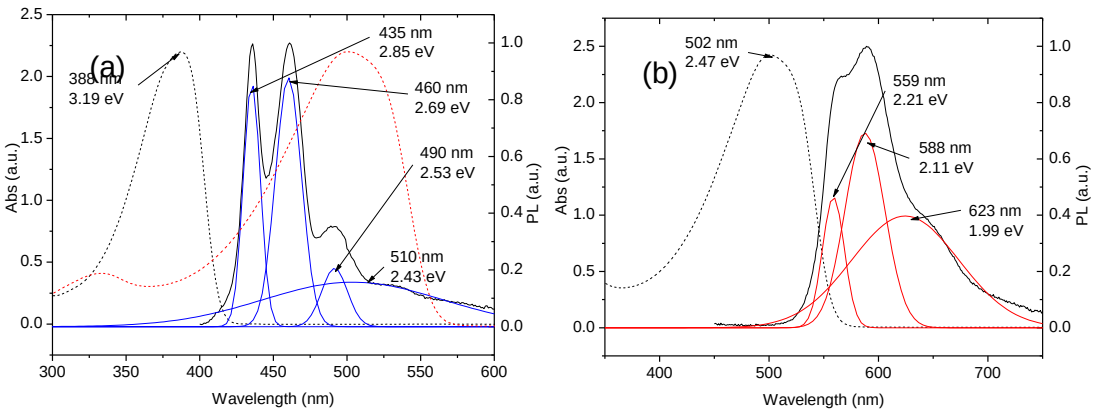

Figure 5-2: Photoluminescence and Absorption for PFO-POSS (a) and MEHPPV-POSS (b). Absorption spectra are plotted as dashed lines. In (a) the absorption of MEHPPV-POSS is plotted as a red dashed line to show the overlap between MEHPPV-POSS absorption and PFO-POSS emission. The emission spectra of PFO-POSS and MEHPPV-POSS has been decomposed in to constituent Gaussian peaks and plotted in solid blue and red lines, respectively.

One of the conditions for efficiency Förster energy transfer is a sufficient overlap of the donor emission and the acceptor extinction coefficient. In Figure 5-2(a), the absorption spectrum of the red acceptor is plotted over the blue donor, showing an acceptable, if not ideal, overlap. It should be noted that these materials were not chosen based on their emission-absorption overlap, but on their electroluminescent color. When combining two colors on a CIE chart, the resultant color coordinate is on a line connecting the two fundamental colors coordinates, so it is important that the fundamental colors of any blend lie on opposite sides of the desired coordinate, (0.33, 0.33).

In Figure 5-3(a), the normalized PL spectra of three blend ratios at 10^{-5}M are plotted along with the normalized spectra of the donor and acceptor materials alone. Clearly, as the relative concentration of the acceptor is increased, the spectra show an increased red component corresponding with a decreasing average intermolecular spacing between the donor and acceptor. Interestingly, the shape of the blend spectra do not

resemble a simple combination of the donor and acceptor spectra. Instead, the relative peak intensities have shifted dramatically. Whereas the height of the blue peak near 440nm is dominant in the donor-alone spectrum, its relative intensity decreases until it is similar to that of the peak located near 415nm as the acceptor ratio increases. On the red side, the dominant peak in the acceptor-alone spectrum is near 595nm while for lower acceptor ratios, the dominant peak is near 550nm.

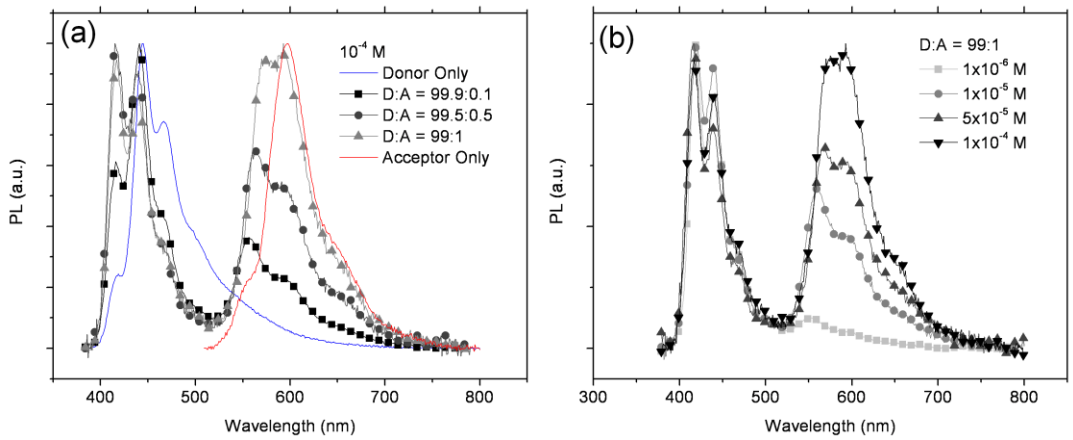

Figure 5-3: (a) The evolution of PL spectra of thin films with a decreasing donor:acceptor ratio. (b) The evolution of PL spectra of dilute solutions of the donor:acceptor ratio 95:5 as the overall molar concentration increases. In both cases, the increase in donor emission is a result of a decrease in average molecular spacing between donor and acceptor.

Clearly, this indicates that not all vibrational modes participate equally in energy transfer. In the case of blends of PFO-POSS and MEHPPV-POSS, energy transfer seems strongest between the 440nm donor peak and the 550nm acceptor peak, based on this analysis. This is a critical point since as the spectrum shape changes, so does the emission color. Thus, two fundamental emitters, when blended, may produce a resulting spectrum whose color coordinate is unexpected from a simple CIE coordinate analysis.

A similar change in spectrum shape is observed when the blend ratio is held constant and the intermolecular spacing is decreased by means of increasing the total concentration. As shown in Figure 5-3(b), an increase in concentration, expectedly, increases the intensity of the red component as the donor and acceptor molecules are brought closer.

The calculated PL quantum efficiencies for all ratios and concentrations are plotted in Figure 5-4 with the PL quantum efficiencies for the donor-only and acceptor-only concentrations. At low concentrations, the efficiencies of the blends match those of the donor-only samples indicating that at sufficiently low concentrations, the molecular spacing is such that Förster transfer and the absorption of the acceptor are negligible. At higher concentrations, the efficiencies of the blends begin to drop as increased Förster transfer shifts molecular excitations from the efficient donor to the less efficient acceptor. The highest acceptor ratio samples (99:1) begin to deviate from the donor efficiency at the lowest concentration (about $1x10^{-7}$ M) followed by the 99.5:0.5 ratio (at about $1x10^{-6}$) and then the 99.1:0.1 ratio (at about $5x10^{-6}$).

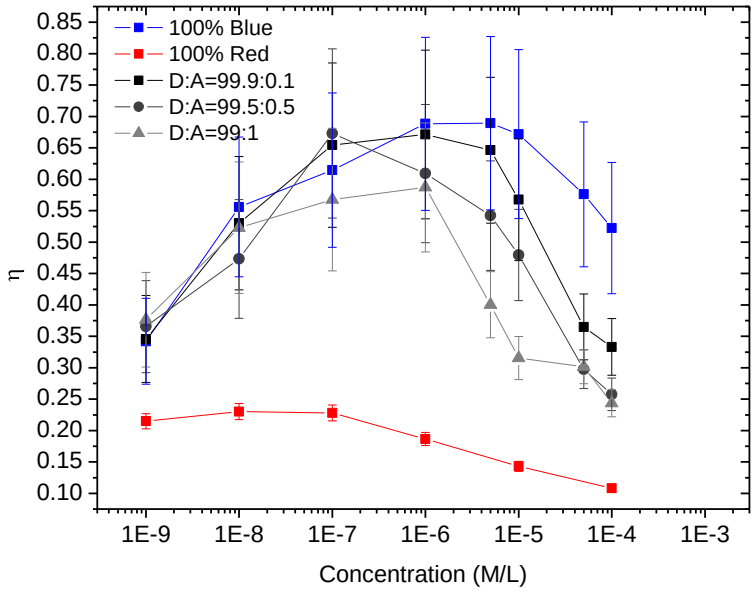

Figure 5-4: PL quantum efficiency versus concentration for blue donor alone (blue diamonds), red acceptor alone (red diamonds) and blend ratios (grey). At low concentrations, the blend emissions behave like the blue donor alone, suggesting little to no Förster transfer.

As the blend concentrations increase, the fractional contribution of the donor (H_D) decreases, as shown in Figure 5-5. Tracing this decrease, we can plot the Förster transfer efficiency as a function of concentration for the three blend ratios (Figure 5-6). The plots confirm the general trend that a higher acceptor ratio and higher concentration will promote Förster transfer.

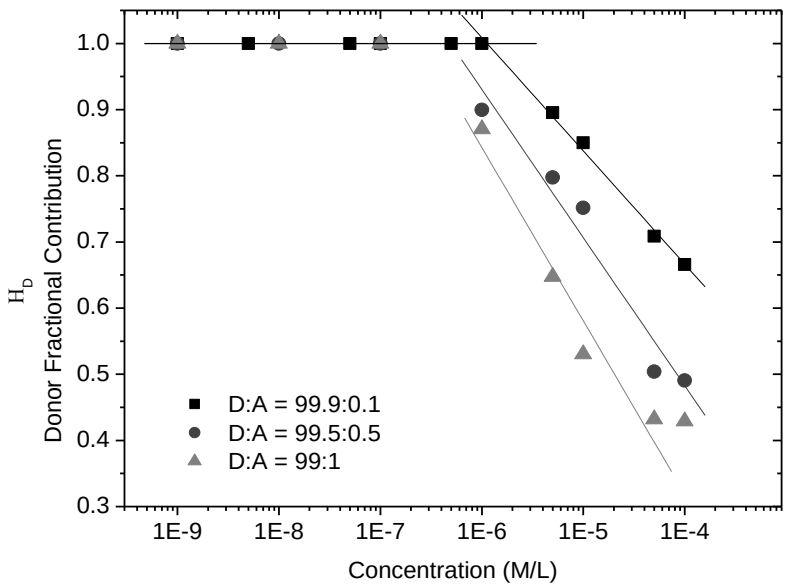

Figure 5-5: Fraction of the total blend emission from the blue donor. The reduction of blue fractional emission at higher concentrations indicates Förster transfer to the red acceptor molecule.

Figure 5-5 shows that below a critical concentration (10^{-7} – 10^{-6} M) all of the detectable emission of the blend originates from the donor. Above the critical concentration, the fraction of the donor decreases steadily.

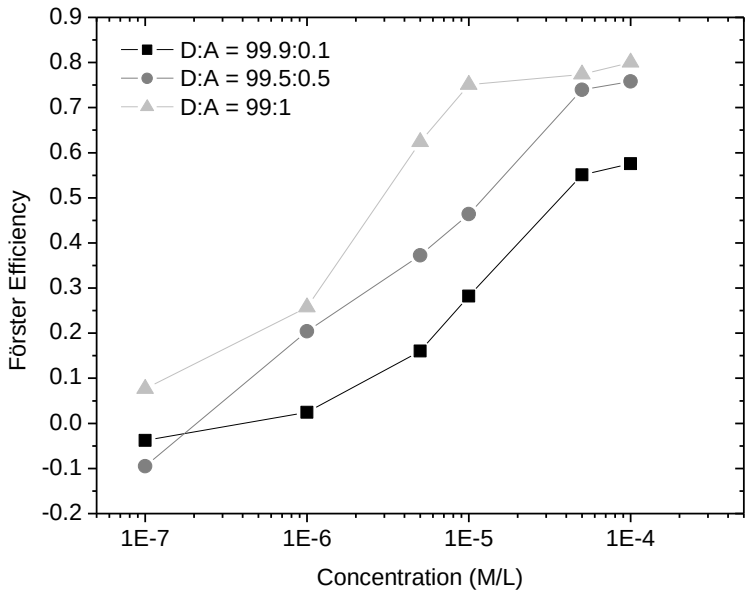

Figure 5-6: Efficiency of Förster transfer as a function of concentration for three blend ratios. As expected, the Förster efficiency increases as the average intermolecular spacing decreases with increasing concentration.

Measurements of Förster transfer efficiency at higher concentrations, extending to concentrations found in thin films, require a slightly different experimental approach and are not pursued in this thesis. Förster transfer efficiency in thin films is of interest because, while the intermolecular spacing is expected to decrease – thus theoretically increasing the Förster transfer efficiency – the rate of intermolecular quenching, aggregation and other bimolecular phenomenon increases – thus theoretically decreasing the Förster transfer efficiency. The competition between these two phenomenon will help determine what, if any, strategies should be employed to maximize Förster transfer efficiency by altering the thin film deposition methods or by adding an inert, transparent filler material, such as poly(methyl-methacrylate), in order to control the thin film concentration.

The question remains as to what, if anything has been gained by blending polymers and generating white light via Förster transfer. For Förster transfer to be an advantageous means of producing white illumination, we should expect an increase in efficiency over the trivial solution of placing two independent blue and red polymer emitters in close proximity. A comparison of PL quantum efficiencies can be made between the measured efficiencies of the blend samples and a hypothetical 2-sample emitter made with the individual electro-optical characteristics of the donor and acceptor molecules and tuned so to produce the same photon flux as a similar blend emitter.

The PL quantum efficiency of a 2-sample emitter producing a similar photon flux as a blend emitter can be calculated via the equation

$$\eta_{2-sample} = \frac{1}{{\mathrm{H}_D}/{\eta_D} + {(1-\mathrm{H}_D)}/{\eta_A}} \tag{5-8}$$

In the above equation, $\eta_{2\text{-sample}}$ is the quantum efficiency of the hypothetical 2-sample emitter, and η_D and η_A are the quantum efficiencies of the donor and acceptor molecules alone, respectively.

Clearly, for dilute solutions which do not exhibit Förster transfer (H_D = 1), the 2-sample emitter has the same efficiency as the blend. Table 5-1 shows the measured PL quantum efficiencies for blends along with the calculated PL quantum efficiency for the 2-sample emitter. For samples with detectable Förster transfer, there is an immediate increase in efficiency by blending the polymers, averaging around +10.6%.

Concentration in xylenes (M)	η for B:R = 99.9:0.1			η for B:R = 99.5:0.5			η for B:R = 99:1		
	2-Sample	Förster Blend	Δ	2-Sample	Förster Blend	Δ	2-Sample	Förster Blend	Δ
1×10^{-4}	0.229	0.333	+0.104	0.177	0.258	+0.081	0.164	0.244	+0.080
5×10^{-5}	0.271	0.365	+0.094	0.197	0.298	+0.100	0.180	0.302	+0.121
1×10^{-5}	0.432	0.567	+0.135	0.350	0.479	+0.129	0.246	0.315	+0.070
5×10^{-6}	0.508	0.646	+0.138	0.408	0.542	+0.135	0.313	0.400	+0.087
1×10^{-6}	0.688	0.671	-0.017	0.542	0.609	+0.067	0.510	0.587	+0.077

Table 5-1: Based on the increase in efficiency shown in PL samples of blends as compared to the 2-sample analog, we conclude that the use of blends of polymers in OLEDs would show an increase in internal efficiency as compared to a similar 2-emissive layer PLED.

White Light Emission from PLEDs Using PFO-MEHPPV blends

Single emission-layer PLEDs were fabricated with donor to acceptor blend ratios of 99.92:0.08, 99.9:0.1, 99.5:0.5, 99:1, and 95:1. The bottom-emitting devices were fabricated on ITO-coated glass with a PEDOT:PSS injection layer and a thermally evaporated bi-layer cathode of calcium and silver. EL spectra were measured with a CCD spectrometer cooled with liquid nitrogen from Horiba Jobin-Yvon.

Figure 5-7 (a) and (b) show the electrical characteristics of a PLED made with a 99.92:0.08 blend ratio. The maximum luminance is 80 cd/m^2 with a turn-on voltage of 9.9V. The maximum emission efficiency is 0.06 cd/A and the maximum power efficiency is 0.017 lm/W.

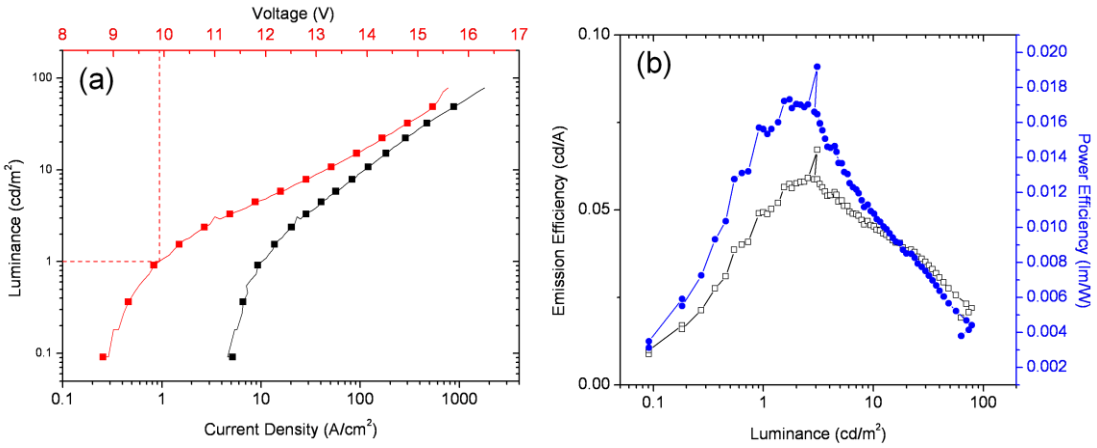

Figure 5-7: (a) Luminance vs. voltage and current density and (b) emission and power efficiency versus luminance for a single-layer PLED with an emissive layer consisting of a 99.92:0.08 PFO:MEHPPV blend ratio.

The CIE coordinates for PLEDs fabricated with several blend ratios is shown in Figure 5-8. As was mentioned previously, the emission envelope of the two emitters changes with blend ratio. This effect, however, is small and only amounts to small deviations from an otherwise straight line connecting two color points. The EL spectra for the donor- and acceptor-alone PLEDs are (0.17, 0.09) and (0.55, 0.45), respectively. The CIE coordinates for the blend PLEDs, however, tend to fall along a line between the donor EL and the acceptor PL (0.49, 0.50). This is due to the different means by which the acceptor is excited – electron injection in the case of EL, and photon absorption in the case of PL. The emission spectrum of the acceptor excited by photon absorption more closely resembles that of the acceptor excited by Förster transfer than by charge injection. The blend comprised of a 99.92:0.8 donor to acceptor ratio was shown to produce an emission closest to pure white, at (0.32, 0.32).

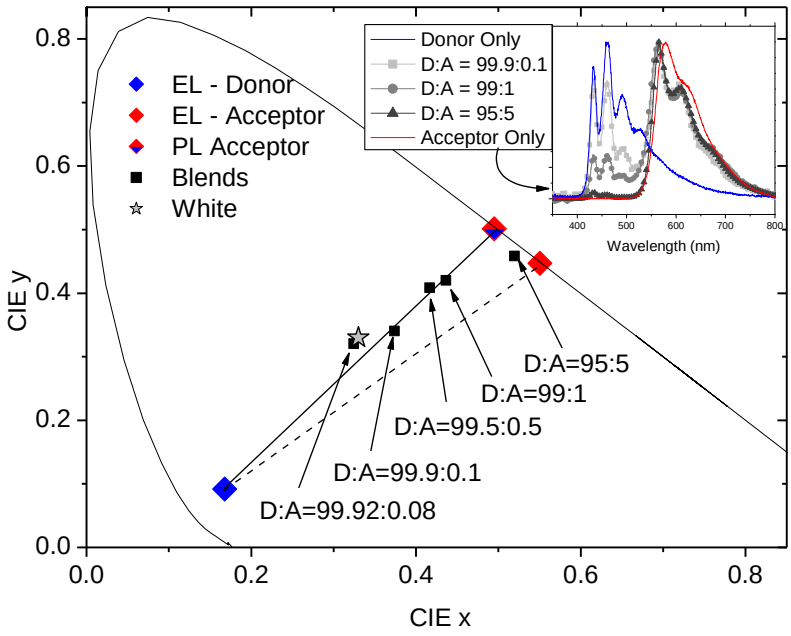

Figure 5-8: CIE coordinates of EL spectra of blends. The CIE coordinate of the acceptor PL is also included. CIE coordinates for the blend emissions fall along a straight line from the donor EL to the acceptor PL (not the red EL). Higher concentrations of acceptor (D:A=95:5) show CIE coordinates between the acceptor PL and EL coordinates. The inset shows the normalized spectra for a selected group of blends, showing the decrease in donor emission.

The CIE coordinates of (0.32, 0.32) correspond to a color temperature of just over 6100K (for reference, the sun has a surface temperature of 5780K). This is not to say that the emission of the blend, when used as an illuminant, will reproduce colors with the same fidelity as would a blackbody emitter. Rather, the relative low luminance in the green-appearing region near 500nm will reduce the color rendering index (13) to such that this particular blend will not be suitable for general lighting applications.

Energy transfer in PFAT-PFBTB systems

While Förster transfer does not involve the formation of a bimolecular complex, the two processes are not mutually exclusive. Systems of molecules whose alignment of energy levels favor partial energy transfer and the formation of complexes such as exciplexes,

may also exhibit Förster transfer. We have studied such a system of polyfluorene-based, fluorescent materials obtained from Dow Chemicals (2)(14)(15). The blue-emitting donor was poly(fluorine-co-anthracene-co-p-tolylamine) (PFAT) and the red-emitting acceptor was poly(fluorine-co-benzothiadiazol-co-thienyl-benzothiadizol) (PFBTB); the molecular structures of each are shown in Figure 5-9. Electrochemical measurements give the HOMO-LUMO gap of PFAT to be 3.72 eV and the gap of PFBTB to be 2.39 eV. Figure 5-9 (c) shows the energy level diagram for the PFAT-PFBTB system.

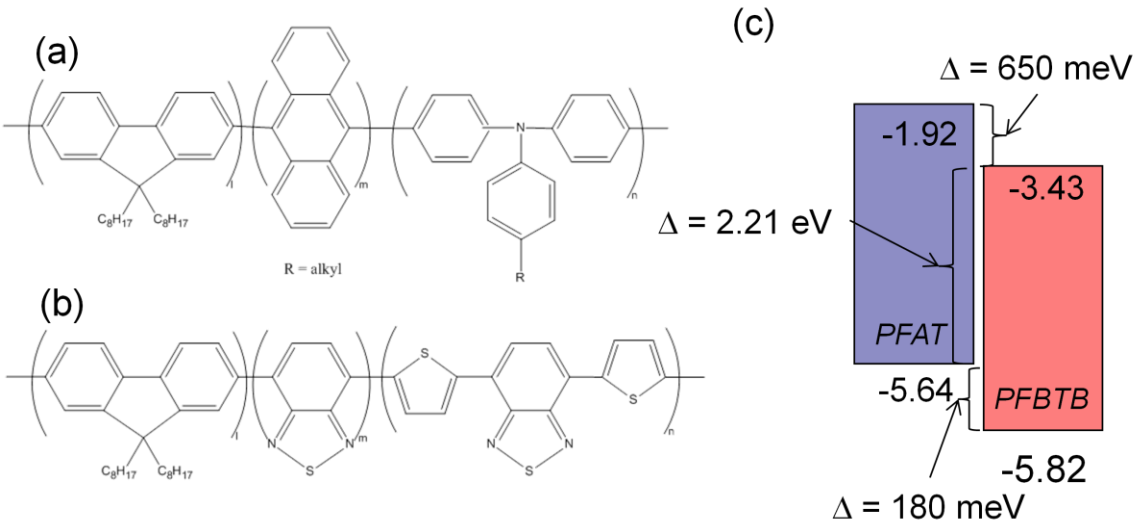

Figure 5-9: Molecular structure for (a) blue-emitting donor poly(fluorine-co-anthracene-co-p-tolylamine) (PFAT) and (b) red-emitting acceptor was poly(fluorine-co-benzothiadiazol-co-thienyl-benzothiadizol) (PFBTB). (c) Energy level diagram for PFAT-PFBTB system.

Figure 5-10 shows the photoluminescence and absorption spectra for thin films of PFAT (a) and PFBTB (b). The PFAT absorption spectrum shows a single absorption peak at 379 nm (3.27 eV). Compared to the estimated HOMO-LUMO gap of 3.72 eV, it is clear that there is a significant difference between the optical and electrochemical gap of the molecule. This suggests that when PFAT is electrically excited, there will be a significant relaxation before the material will emit. The photoluminescence of PFAT has been decomposed in to constituent Gaussian peaks. The highest energy fitted peak is

centered at 463 nm (2.68 eV). Two additional lower energy peaks, centered at 488 nm (2.54 eV) and 522 nm (2.38 eV), complete the PFAT emission envelope.

The PFBTB absorption spectrum shows two distinct peaks at 465 nm (2.67 eV) and 335 nm (3.7 eV). There is also a low energy shoulder near 570 nm (2.17 eV). Like the case of PFAT, the dissimilarity between the absorption peaks and the measured electrochemical gap point to a large amount of energy released during molecular relaxation. This is supported by the large stokes shift (0.86 eV) between the first decomposed emission peak at 649 nm (1.91 eV) and the 465 absorption peak. The presence of the absorption shoulder at 565 nm implies that a photoexcited molecule decays non-radiatively to an intermediate trap state before emitting a photon.

In Figure 5-10 (a), the red dashed line indicates the absorption spectrum of the PFBTB material. As can be seen, there is very good overlap between the spectra suggesting that this system will exhibit efficient Förster transfer.

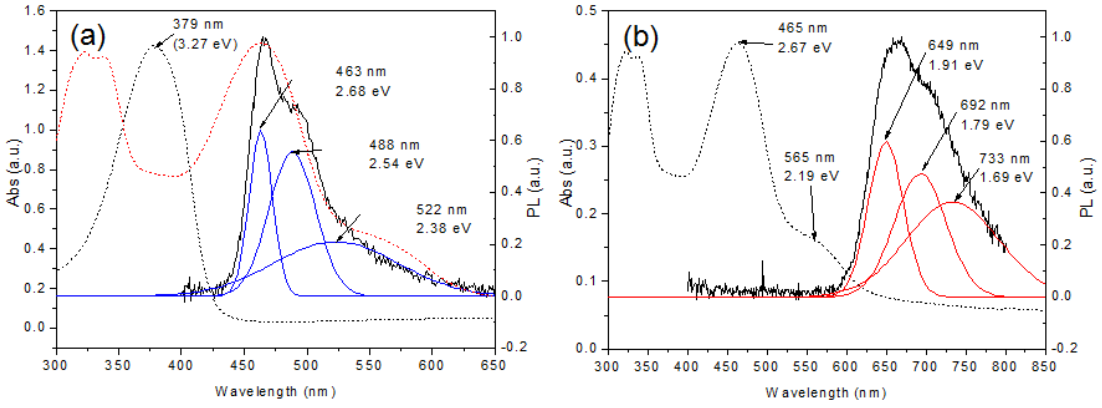

Figure 5-10: Absorption (dashed line), photoluminescence (solid black line) and decomposition (solid red and blue line) for DOW Blue (a) and DOW red (b) polymers

As seen in the energy level diagram of Figure 5-9, the PFAT-PFBTB system has an offset in the HOMO and LUMO values which would tend to promote partial energy transfer

from the donor to the acceptor (16)(17). When an electric field is applied, this offset would tend to confine electrons in the PFBTB phase and holes in the PFAT phase. The formed bimolecular complex is known as an exciplex. The formation of such complexes is an important feature in regards to PLED design as the radiative exciplex decay will alter the emission spectrum of the blend.

The energy of the emitted photon from an exciplex is the difference between the ionization potential of the donor molecule and the electron affinity of the acceptor molecule, less a small amount of energy from the coulombic interaction of the molecules (Δ)(16).

$$E_{ex} = (EA_A - IP_D) - \Delta_{ex} \quad (5\text{-}9)$$

Hence, exciplex formation is detected by the presence of an additional emissive element in the emission spectra for blends of PFAT and PFBTB.

Figure 5-11 shows the PL (a) and EL (b) spectra of thin films made from solutions of PFAT-PFBTB blends of varying weight ratio. The PL and EL spectra of the individual polymers are also included in Figure 5-11 for comparison. Despite the low concentration of PFBTB compared to PFAT, it is clear that a small amount of PFBTB produces a disproportionately large flux of photons. In PL measurements, at 1% concentration by weight, the peak PFBTB emission (within the range of 600-800nm) is greater than the peak PFAT emission. In the case of EL, the peak emissions of PFAT and PFBTB are roughly equal at a red concentration of 0.6%. This is clear evidence of Förster transfer of energy from the PFAT to the PFBTB as the disparity in volume and mass of

the two polymers would tend to favor only PFAT emission in the hypothetical absence of Förster transfer.

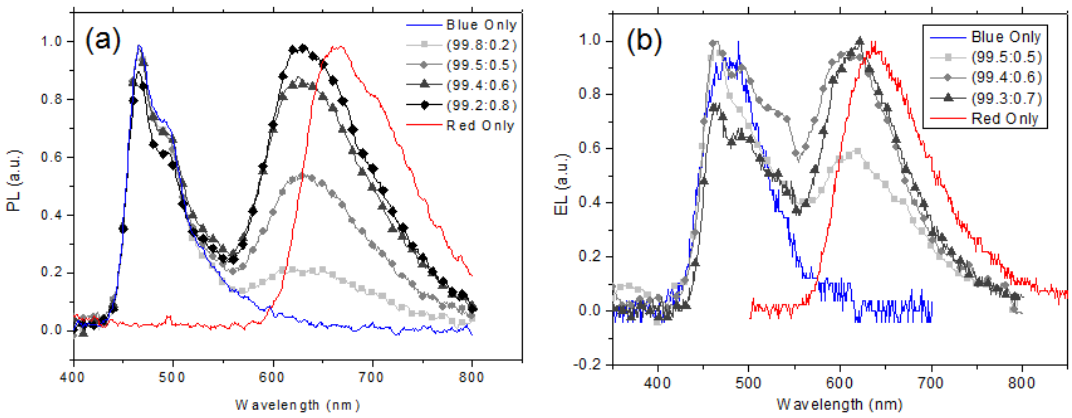

Figure 5-11: Photoluminescence (a) and electroluminescence (b) of blends of DOW blue- and red-emitting polymers

Interestingly, in both the EL and PL spectra, the addition of a small amount of PFBTB appears to blue-shift the red side of the emission when compared to the emission of PFBTB alone. However, a decomposition of both the EL and PL emission spectra (shown in Figure 5-12) reveals that the apparent blue shift is the result of an additional emission centered at 610 nm (2.03 eV) for PL and 588 nm (2.11 eV) for EL. This additional emission is the result of an exciplex forming between the donor and acceptor molecules. The difference between the donor ionization potential and the acceptor electron affinity is 2.21 eV, giving the coulombic interaction between the molecules as Δ_{ex}= 0.1 eV. It should be noted that the exciplex emission is higher in energy than the Red F emission, which is typically not expected since $EA_A - IP_D$ is less than the HOMO-LUMO gap of either molecule (16)(18)(19). As was discussed above, though, the discrepancy between the electrochemical gap and the absorption peak of PFBTB suggests that there is significant relaxation from the electrically excited state to where

the polymer will emit. As a result, the single polymer emission energy can be less than the heterodimeric emission.

Figure 5-12 shows the seven fitted Gaussian peaks for the EL (a) and PL (b) spectra of the samples made with the 99.4:0.6 blend. The addition of this peak, positioned between the emission of the PFAT and PFBTB emission regions, appears to shift the emission of the red polymer.

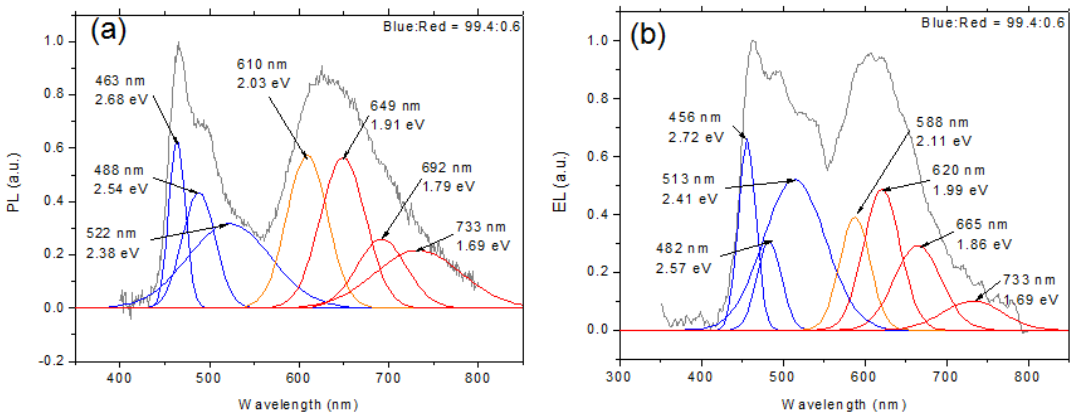

Figure 5-12: Decomposition of EL (a) and PL (b) for blends of PFAT and PFBTB with donor:acceptor ratio of 99.4:0.6

The emission of this additional decay mode is in close agreement with the difference in DOW Red's electron affinity and DOW Blue's ionization potential (2.21 eV).

Unfortunately, due to the presence of this additional exciplex decay mode, the method previously employed to extract the efficiency for Förster transfer is not applicable. With the addition of the exciplex formation constant, the Förster transfer efficiency becomes:

$$E = \frac{k_T}{k_r + k_{nr} + k_T + k_{Ex}} \tag{5-10}$$

where k_{Ex} is the rate of exciplex formation. This obliges an additional measurement to isolate the exciplex emission.

White light Emission from PLEDs using PFAT-PFBTB blend

Single emission-layer PLEDs were fabricated with donor to acceptor blend ratios of 99.4:0.6, 99.5:0.5, and 99.3:0.7. The bottom-emitting devices were fabricated on ITO-coated plastic (20). The fabrication procedure has been reported previously (21). Figure 5-13 (a) shows the luminance vs. voltage and current density while Figure 5-13 (b) shows the emission efficiency and power efficiency vs. luminance for a PLED fabricated with a PFAT:PFBTB ratio of 99.4:0.6. The maximum luminance is 7366 cd/m^2 with a turn on voltage of 5.6V. The maximum emission efficiency is 1.96 cd/A and the maximum power efficiency is 1.09 lm/W.

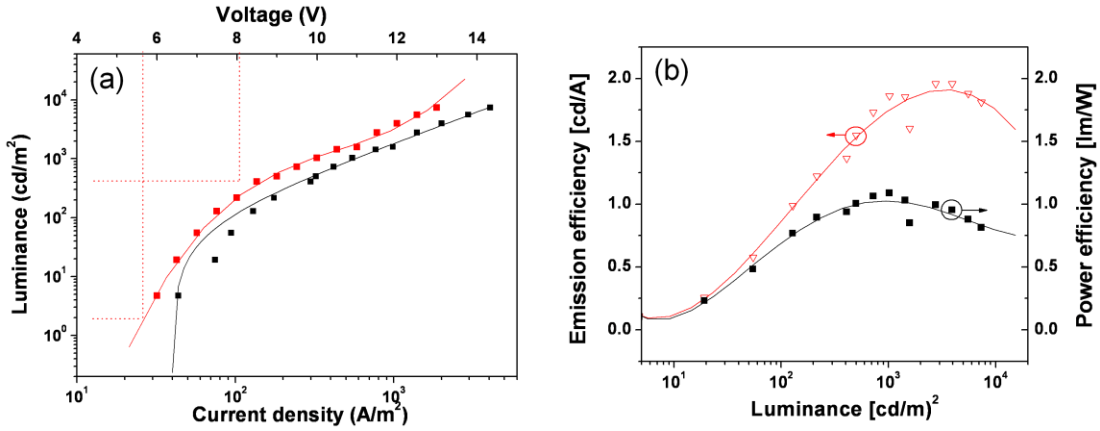

Figure 5-13: (a) Luminance vs. applied voltage and current density; (b) Emission and power efficiency vs. luminance for PLED on plastic substrate using 99.4:0.6 PFAT:PFBTB blend

The decomposed EL spectra for PFAT and PFBTB are shown in Figure 5-14. PFAT shows three peaks: the highest energy peak is centered at 456 nm. The dominant peak is at 483 nm while a broad peak which accounts for the blue emission's long tail is centered at 514 nm. Similarly, the DOW Red EL spectrum shows three peaks with the best fit revealing two main peaks at 621 nm and 665 nm and a broad emission centered at 732 nm.

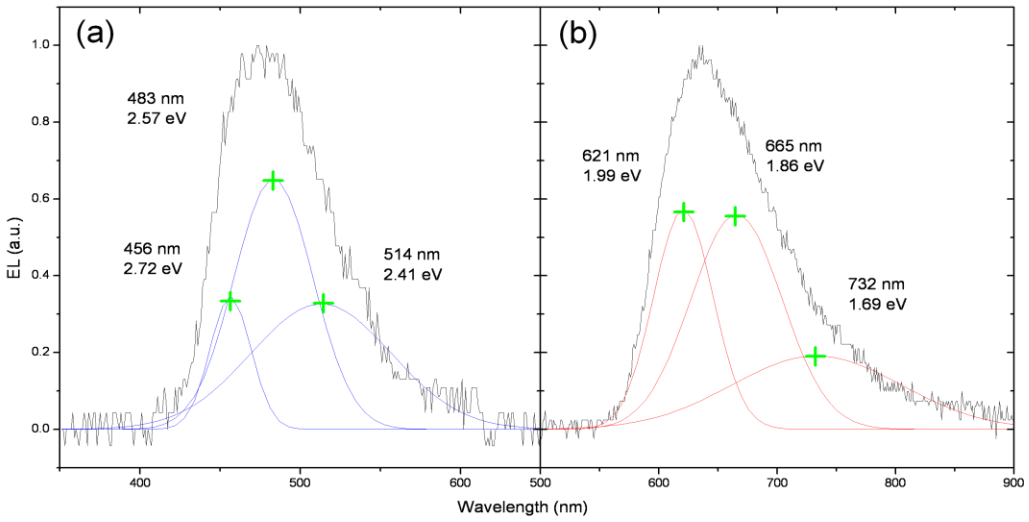

Figure 5-14: Electroluminescence (solid black line) and decomposition (solid red and blue lines) of DOW blue (a) and DOW red (b) polymers

It has already been mentioned that these reference peaks cannot be used to determine the Förster transfer efficiency. The utility of these peaks comes when analyzing the odd behavior of the emission CIE coordinates as the blend ratio changes. As in the case of the PFO-MEHPPV system, the emission envelope of the emitters in the PFAT-PFBTB system change with blend ratio. Unlike the PFO-MEHPPV system, though, the change in donor emission is quite drastic (Figure 5-15 (a)), resulting in a somewhat erratic progression of CIE coordinates (Figure 5-15 (b)), which does not seem to follow a line originating from the donor emission (the acceptor emission, by contrast, changes very little). By decomposing the blend spectra and arithmetically reconstructing the blue emission, we see that the resulting CIE color coordinates arise from an evolving donor emission color.

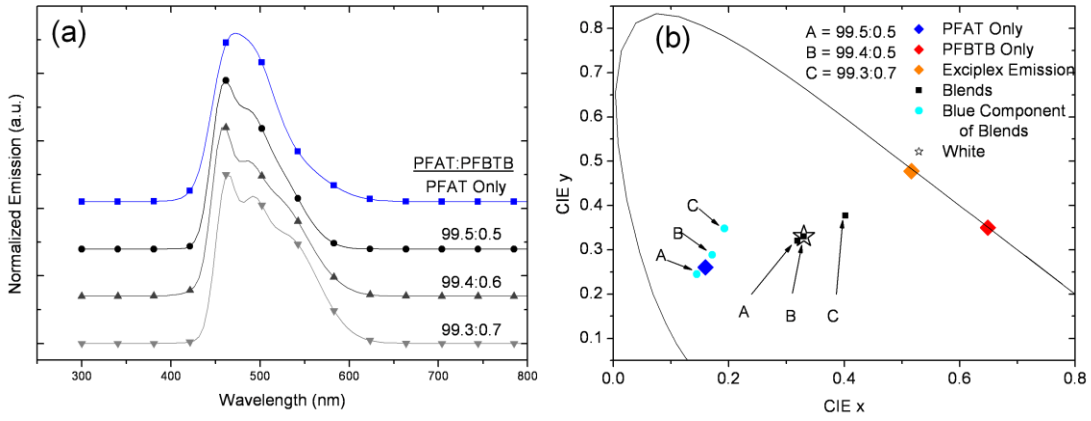

Figure 5-15: (a) PFAT emission spectra reconstructed from the fitted blend spectra reveal an evolving emission envelope. (b) The CIE color coordinates for the PFAT emissions, blend emission, exciplex emission PFAT and PFBTB emissions.

Conclusions

The emission color for polymer blends of fluorescent materials is highly dependent on blend ratio. This is due not only to the critical dependence of Förster transfer on average molecular spacing (which is strongly affected by blend ratio) but also due to the uneven participation of fluorophores and vibrational modes in energy transfer. Polymer blend systems which preferentially transfer energy from specific decay modes alter the fundamental emission colors, resulting in PLED emissions which may veer to the blue or red unexpectedly. In addition, certain polymer blend systems promote the formation of bimolecular complexes. When these complexes decay radiatively, the blend emission is altered accordingly, producing unexpected results. Therefore, designers of white-emitting PLEDs made from blends of fluorescent polymers must take in to consideration the non-linear combination of polymer emissions

Bibliography

[1] Gu, G., Parthasarathy, G., Burrows, P. E., Tian, P., Hill, I. G., Kahn, A., Forrest, S. R., Transparent stacked Organic Light Emitting Devices. I. Design Principles and Transparent Compound Electrodes. Journal of Applied Physics, Vol. 86, p. 4067, (1999)

[2] Lee, H., Johnson, A. R., Kanicki, J., White LED Based on Polyfluorene Co-Polymers Blend on Plastic Substrate. IEEE Trans. Elec. Dev., Vol. 53, p. 427, (2006)

[3] Virgili, T., Lidzey, D. G., Bradley, D. D. C., Adv. Mat, Vol. 12, p. 58, (2000)

[4] Gong, X., Parameswar, K. I., Moses, D., Bazan, G. C., Heeger, A. J., Xiao, S. S., Stabilized Blue Emission from Polyfluorene-Based Light-Emitting Diodes: Elimination of Fluorenon Defects. , Vol. 13, , (2003)

[5] Liu, J., Zhou, Q., Cheng, Y., Geng, Y., Wang, L., Ma, D., Jing, X., Wang, F., White Electroluminescence from a single-polymer system with simultaneous two-color emission: Polyfluorene as the blue host and a 2,1,3-Benzothiadiazole derivative as the orange dopant on the main chain. Adv. Func. Mater., Vol. 16, p. 957, (2006)

[6] Shen, F., He, F., Lu, D., Xie, Z., Xie, W., Ma, Y., Hu, B., Bright and Colour stable while polymer light-emitting diodes. Semicond. Sci. Technol., Vol. 21, p. L16, (2006)

[7] Epe, B., Steinhauser, K. G., Woolley, P., Theory of measurement of Forster-type energy transfer in macromolecules. Proceedings of the National Academy of Sciences, Vol. 80, pp. 2579-2583, (1983)

[8] Meer, B. W. Van Der, Coker, G., Chen, S. -Y. S., Resonance Energy Transfer: Theory and Data. New York : VCH, 1994.

[9] Berlman, I., . Energy Transfer Parameters of Aromatic Compounds. New York : Academic Press, 1973.

[10] Morawetz, H., Studies of Synthetic Polymers by Nonradiative Energy Transfer. Science, Vol. 240, p. 172, (1988)

[11] Birks, J. B., Kuchela, K. N., Energy Transfer in Fluorescent Plastic Solutions. Disc. Faraday Soc., Vol. 27, p. 57, (1959)

[12] Vogel, S. S., Thaler, C., Koushik, S. V., Fanciful FRET. Sci. STKE, Vol. re2, , (2006)

[13] Committee on Colorimetry Quantative Data and Methods for Colorimetry. J. Opt. Soc. Amer., Vol. 34, p. 633, (1944)

[14] Bernius, M. T., Inbasekaran, M., O'brian, J., Wu, W., Progress with light-emitting polymers. Adv. Mater., Vol. 12, p. 1737, (2000)

[15] Inbasekaran, M., Wu, W., Woo, E. P., Bernius, M. T., Fluorene copolymers and Devices Made Therefrom. 6353083 Mar 5, 2002.

[16] Offermans, T., Hal, P. A. van, Meskers, S. C. J., Koetse, M. M., Janssen, R. A. J., Exciplex dynamics in a blend of pi-conjugated polymers with electron donating and accepting properties: MDMO-PPV, and PCNEPV. Physical Review B, Vol. 72, p. 045213, (2005)

[17] Sun, Q. J., Fan, B. H., Tan, Z. A., Yang, C. H., Li, Y. F., Yang, Y., White Light from polymer light-emitting diodes: Utilization of fluorononе defects and exciplex. App. Phys. Lett., Vol. 88, p. 163510, (2006)

[18] A.C., Morteani, Dhoot, A.S., Kim, J.-S., Silva, C., Greenham, N.C., Murphy, C., Moons, E., Ciná, S., Burroughes, J.H., Friend, R.H., Barrier-Free Electron-Hole Capture in Polymer Blend Heterojunction Light-Emitting Diodes. Adv. Mater., Vol. 15, p. 1708, (2003)

[19] Wang, S., Bazan, B. C., Exciplex formation with distyrylbenzene derivatives and N,N-dimethylaniline. Chem. Phys. Lett., Vol. 333, p. 437, (2001)

[20] Hong, Y., He, Z., Lennhoff, L. S., Banach, D., Kanicki, J., Transparent flexible substrates for organic light-emitting devices and other devices. J. Electron. Mater., Vol. 33, p. 312, (2004)

[21] Hong, Y., Kanicki, J., Opto-electronic properties of poly (fluorene) co-polymer red light-emitting devices on flexible plastic substrate. IEEE Trans. Electron Devices, Vol. 51, p. 1562, (2004)

Chapter 6
Low Temperature, Thin Film Encapsulation for OLEDs

Introduction

One of the major factors which diminish OLED lifetime is exposure of atmospheric oxygen and moisture (1) to the device structure. Oxygenated contaminants severely reduce the lifetime of organic devices (2). Moisture can react with the low work-function metal cathode, delaminating the electrode from the organic layers (3). In addition, contaminants can degrade the hole transporting layer, reducing the efficiency of hole injection or react directly with the emissive layer (4), annihilating the active chromophores or quenching luminance (5).

The presence of oxygen in emissive layers is not only a source of collisional quenching, photo-oxidation has been shown to cause specific chemical reactions in emissive polymer. In studies of copolymers of 9,9-di-n-hexylfluorene and anthracene photo-oxidation is known to cause the formation of flurornone defects by replacing the aliphatic chain with carbonyl groups at the 9 position (6). The presence of the double bonded oxygen quenches the fluorescence of the unadulterated fluorene since excitons are likely to diffuse to that location. Samples of polyfluorene-based polymers under exposure to oxygen show an increase in intensity from the excimer emission of the

fluorononе defect and an overall decrease in total luminance. This is the source of the well known blue-green shift in the emission of polyfluorene-based OLEDs (7).

In addition, the presence of moisture in the emissive region has been shown to cause crystallization of tris (8-hydroxyquinoline) aluminum layers (8). Highly polar water molecules can, similar to oxygen, form luminance quenching centers, but the major effect of moisture is on the cathode/organic interface.

The effect of oxidizing agents on the organic/cathode interface causes perhaps the most dramatic change in OLED performance. As OLED devices age, the appearance of non-emissive dark spots becomes evident. These dark spots decrease the effective pixel size and emission intensity, severely limiting the device lifetime. It is proposed that dark spot formation and growth is caused by oxygen and moisture diffusing through microscopic pinholes in the electrode. This, in turn, can cause the formation of metal hydroxide at the electrode-organic interface causing delamination of the cathode from the organic layers (9) (3), or the formation of an insulating layer from the oxidation of the organic layer beneath (10). Due to the low electron affinity of these materials, the cathode interface is highly susceptible to oxidation by atmospheric oxygen and water vapor. Even with aluminum or silver capping layers, oxygen and moisture transmission quickly converts the conductive metal layer to its oxidized form (11). For the calcium cathodes used the OLEDs employed in this study, the reaction is:

$$\begin{aligned} Ca + H_2O &\rightarrow CaO + H_2 \\ 2Ca + O_2 &\rightarrow 2CaO \\ CaO + H_2O &\rightarrow Ca(OH)_2 \end{aligned} \qquad (6\text{-}1)$$

Figure 6-1 shows the effect of this oxidation on a green-emitting, polyfluorene-based OLED with a Ca/Ag cathode. Figure 6-1 (a) is the OLED while under operation with an applied voltage of 10V. The dark spots nucleate at the location of pinhole defects in the electrode and gradually expand as oxygen and moisture diffuse in to the device. Figure 6-1 (b) shows the surface of the OLED when the device is turned off. It is clear from this image that the origin of the dark spots is the region of morphological change shown in this image. Figure 6-1 (c) is a 50x magnification of this region. Within the circular regions which give rise to the dark spots (shown in greater detail in Figure 6-1 (d), a 100x magnification), a color gradation from dark blue at the edges of the circular regions to dark red at the center appears. This pattern is the result of wavelength filtering caused by deconstructive interference of light passing through the calcium oxide/hydroxide layer and reflecting off the silver electrode. A careful examination of the images reveals a small hole at the center of each of the circular regions. This suggests that the source of the pinhole defect is particulate contamination.

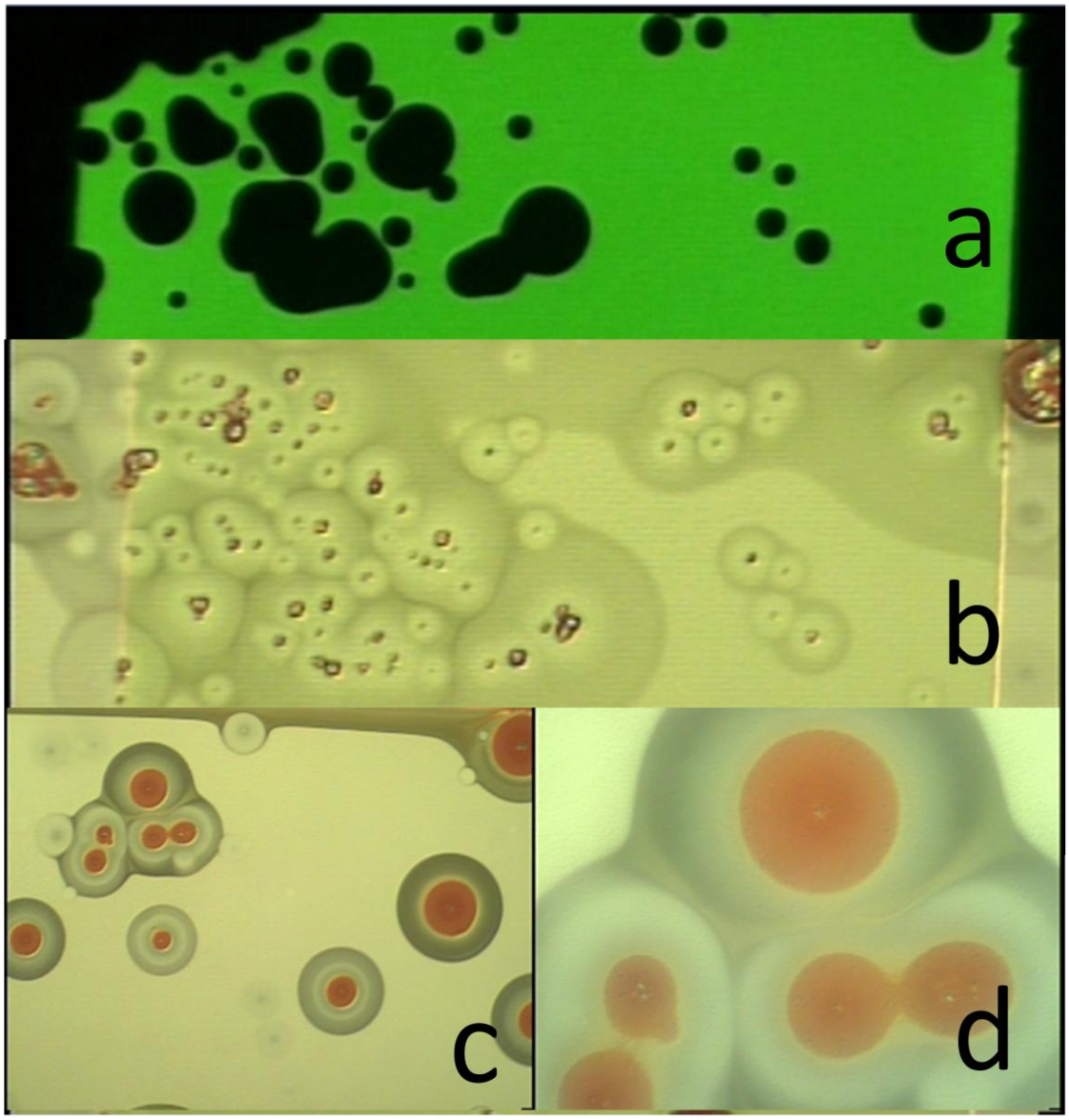

Figure 6-1: Dark spot growth from oxidation and delamination of the cathode. (a) Evidence of dark spots forming while the device is illuminated. (b) Image of the OLED surface after operation. (c) Detail of surface at 50x magnification. (d) 100x magnification

Encapsulation Techniques

Encapsulation of the OLED structure within a protective shell has been employed by many researchers as a way to protect the delicate device and extend the useful lifetime of the OLED (12) (13) (14). Encapsulation works by fabricating a passive structure around the OLED which is impenetrable to atmospheric oxygen and moisture. The

reduction in exposure to atmospheric oxygen and moisture extends the usable lifetime of the device. The most effective structure to accomplish this is the subject of active research. For encapsulation schemes to be useful for commercial applications, it is estimated that the water-vapor transmission rate (WVTR) and oxygen transmission rate (OTR) must be better than $1x10^{-6}$ g/m^2-day and $1x10^{-5}$ cm^3 (STP)/m^2-day, respectively (12).

One of the first encapsulation methods employed towards this end is the addition of a rigid, transparent cap, adhered to the device by a bead of epoxy around the device structure (12) (13), as shown in Figure 6-2.

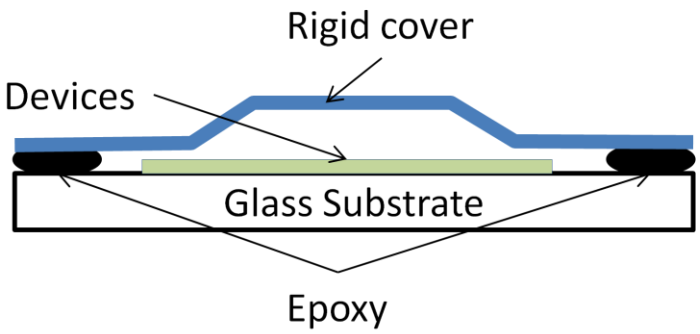

Figure 6-2: Schematic of rigid encapsulation structure

Rigid encapsulation schemes have the drawback in that the glass or metal cover is often bulky and heavy, properties that make this solution ill-suited for display applications. In addition, for flexible OLED applications, the use of a rigid encapsulation structure would be counter-productive. One method to overcome this is to laminate a flexible plastic cap with barrier layers and use an epoxy to seal this cap to the device as shown in Figure 6-3. While flexible caps can be made thin enough for display applications, their efficacy is limited by the use of the epoxy sealants. Epoxies which have low WVTR and OTR are typically rigid (14), which works against the advantages of a thin, flexible cap.

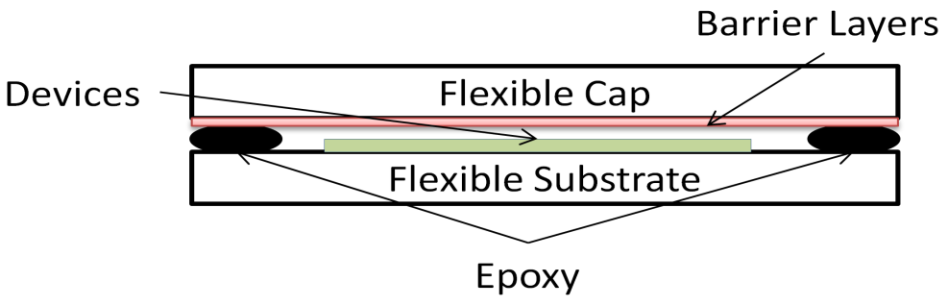

Figure 6-3: Schematic of encapsulation scheme utilizing flexible cap

Thin film encapsulation schemes (TFES), on the other hand, use thin film deposition techniques such as plasma-enhanced chemical vapor deposition (PECVD), sputtering and other physical vapor deposition techniques to fabricate a stack of conformal, pinhole-free barrier layers. This type of encapsulation has a much thinner form factor, which is needed for display applications. In addition, with the fabrication of low-stress structures, it is possible to encapsulate devices on flexible substrates. Additionally, since a TFES is fabricated directly on the device, there is no concern for abrasion of the OLED surface.

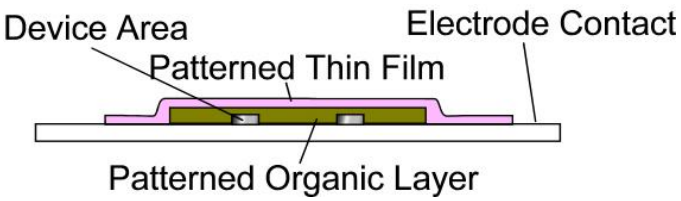

Figure 6-4: Schematic of thin films encapsulation scheme

The deposition process for TFESs, however, must be commensurate with the organic devices. This limits the deposition techniques applicable to TFESs to those which do not involve harsh organic solvents or cause undue stress to the devices. There are a number of criteria that a TFES must meet in order to be applicable to OLED encapsulation.

Encapsulation Criteria

1. **Low oxygen and moister transmission rates** – The highest priority of any thin films encapsulation technique is to effectively block the diffusion of oxidizing agents. It has been estimated that in order for OLEDs to be commercially viable, encapsulation schemes should reduce the oxygen transmission rate (OTR) and water vapor transmission rate (WVTR) to the maxima of 10^{-5} $cm^3(stp)/m^2$-day and 10^{-6} g/m^2-day, respectively (12; 15).
2. **Low Temperature** – Owing to their typically low glass-transition temperatures and melting points, organic materials are particularly sensitive to exposure to heat. For instance, polyfluorene and polyfluorene copolymers have glass transition temperatures between 80°C and 130°C (16) (17). The small molecule Alq3 has a glass transition temperature of 177°C (18). Deposition methods must be low temperature to accommodate these restrictions.
3. **Low Ion bombardment** – Similarly, organic materials can be damaged by excessive exposure to high energy ions bombarding the surface. This is a concern when employing plasma-based deposition processes such as PECVD or RF sputtering, both of which accelerate ions towards the substrate through high DC biases. The deposition conditions must be such that these DC biases are kept to a minimum, while still providing sufficient energy to coat the OLED at an appreciable rate.
4. **Conformal coverage** – Deposited films must completely coat the underlying devices. While feature sizes for OLEDs are typically large, sidewalls at the edges

of the OLED electrodes do exist and deposition methods must be able to protect these sensitive areas, i.e. there should be no shadowing effect.

5. **Dense, pinhole-free films** – Porous and pinhole-ridden films lead to accelerated rates of moisture and oxygen diffusion. In turn, moisture absorption in to the encapsulant films can further degrade the quality of the encapsulation, speeding up the degradation of the device. Pinhole density and film density are functions of the deposition conditions and, as such, processes should be designed with this criteria in mind.
6. **Near-Zero stress** – Highly stressed encapsulation films have short effective lifespans. As the film relieves the internal stress, the mechanical properties of encapsulation scheme degrade. A number of failure mechanisms for highly stressed inorganic films are described below. Low-to-zero stress films maintain their barrier properties and, in addition, can be incorporated in to device structures on flexible substrates.

Low-Temperature Plasma-Enhanced Chemical Vapor Deposition

One deposition technique which has the potential to meet these rigorous requirements is PECVD (19). PECVD has the ability to deposit conformal, dense films at low temperature without the use of chemicals which may damage the underlying devices. In PECVD systems, thin films are fabricated by blending reactive gasses and adding these mixtures to chambers containing process' substrates. Deposition proceeds when enough energy is supplied to the gas to induce chemical reactions on the substrate surface. In low temperature PECVD systems, this energy is supplied by forming a plasma

by ionizing the reactive gasses. The plasma is formed by ionizing the gasses and sustained by continuous electron bombardment of the gas molecules. The electron bombardment gives rise to a menagerie of reactive and excited species as the high energy electrons spur on the complex plasma chemistry. The reactive species adsorb to the substrate surface where they diffuse and react with other adsorbed species, growing the desired film. The plasma can be formed a number of ways, and the type of PECVD system is classified by how the plasma is formed.

In this study, two types of PECVD systems were used. The first is termed capacitively coupled and generates plasma by coupling an RF signal to the reactive gas by means of, expectedly, a capacitor. Figure 6-5 shows the schematic for a capacitively coupled PECVD (20). The chamber is arranged with two electrode. Substrates are placed on the bottom electrode, which is equipped with a heating element and can be either grounded or biased with a negative DC voltage. The top electrode is connected to an RF power supply. Process gasses are introduced to the chamber through the upper electrode, which typically has a showerhead design to efficiently introduce gasses directly in to the plasma. The plasma is established between the electrodes by the application of an electric field typically at 13.56 MHz. Due to the higher mobility of the electrons within the plasma, a DC bias develops between the plasma (positive, due to the high concentration of nuclei) and the electrode. This DC bias accelerates reactive ions to the surface of the substrate. One drawback of a capacitively coupled system is that the plasma current and the DC bias cannot be independently controlled.

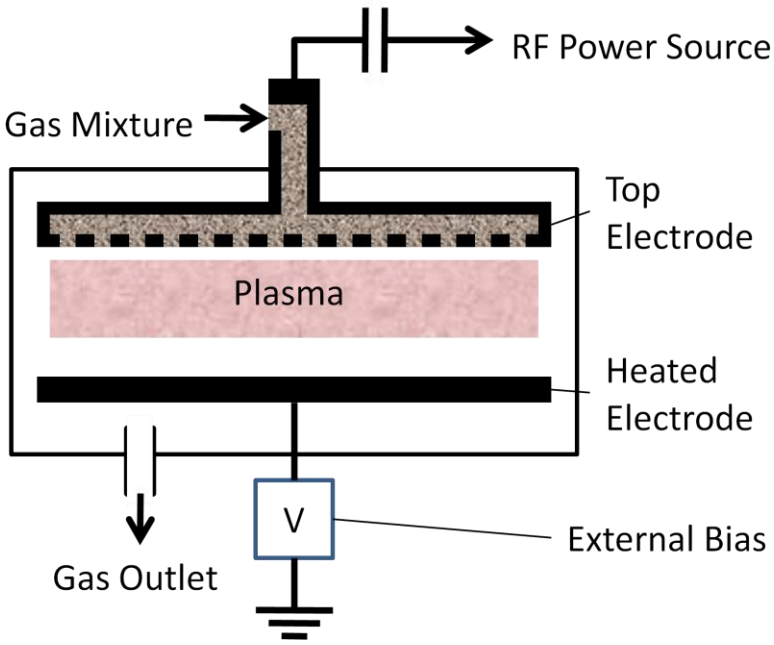

Figure 6-5: Schematic of a capacitively coupled PECVD system

Alternatively, energy can be coupled to the plasma by means of a microwave signal. In an electron cyclotron resonance system (ECR), microwaves are coupled to the gas chamber through a quartz window (21). The microwaves are right-hand circularly polarized, which heats the electrons until they dissociate from the atom, forming a plasma. Figure 6-6 shows a schematic of an ECR system. ECR PECVD typically produces dense plasmas (22). Microwave coupling does not, however, generate a DC self bias. Thus, an RF or DC source must be applied to the substrate holder if ion acceleration is to be used during deposition. This allows independent control of the plasma current and the DC bias.

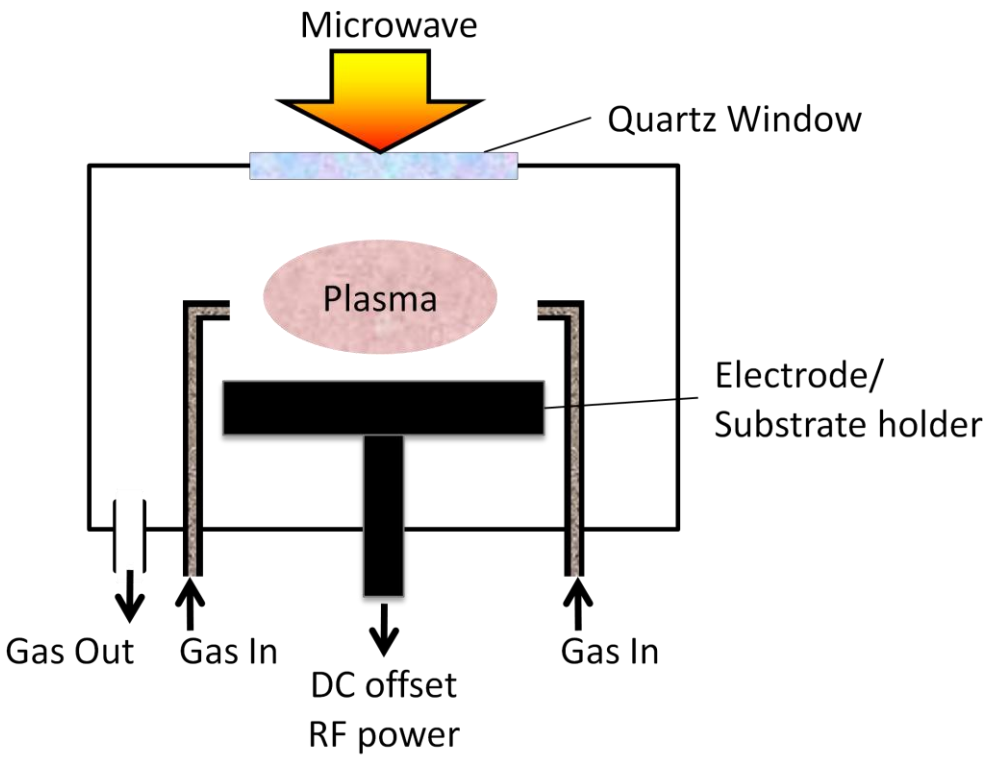

Figure 6-6: Scematic of electron cyclotron resonance PECVD

Both systems have the ability to deposit at low temperature. This is a non-trivial matter as most PECVD processes utilize higher temperature to produce denser films. The high substrate temperatures (200-400^{o}C or higher) increase the mobility of adsorbed reactive species, allowing them to fill in microvoids – forming a dense layer – and increasing the reaction rate between molecules. Since encapsulation of OLEDs requires lower substrate temperature, a number of issues arise which must be experimentally overcome.

Low Temperature Concerns

The deposition conditions for amorphous silicon nitride (a-H:SiN_x), amorphous silicon oxide (a-SiO_x) and amorphous carbon (a-C) are often developed for the semiconductor industry wherein deposition temperatures of 200˚C, 380˚C or higher can be used. The

glass transition temperatures of many of the polymeric materials used in the fabrication of OLEDs is typically less than 150˚C. As a result, deposition recipes cannot be transferred wholesale from inorganic processes to OLED passivation as these conditions would damage the delicate organic layers underneath. Moreover, pinhole density, film stress, film density and deposition rate are highly dependent on deposition temperature and power. Hence, the development of low temperature and low power recipes for effective TFESs is non-trivial.

The incorporation of hydrogen in to silicon nitride and silicon oxide films is a consistent concern for depositing dense barriers, as hydrogen chemically bonds to silicon, nitrogen and oxygen. There is a direct linear relationship between the hydrogen content of a film and the buffered HF etch rate (23). HF etch rate is an indication of film density (lower density leads to higher etch rate), which suggests that hydrogen content is a leading factor in reducing the density of deposited films. Van Assche et. al. (24) report that increasing the density of nitride films deposited via low temperature PECVD does not significantly increase the properties of encapsulating films (namely oxygen and moisture diffusion) indicating that the permeability of the films is dominated by defect density.

Deposition temperature has a strong effect on the quality of the forming surface and, as a result, the bulk mechanical properties of the film. The formation of pinholes and surface irregularities in films grown by chemical vapor deposition processes minimizes the mean surface energy of the developing film. The diffusion of atoms from surface flats to surface irregularities (a process which would result in smooth, layer-by-layer growth and, hence, denser films) is impeded by barriers to diffusion at the edges of

these irregularities. Higher deposition temperatures increase the diffusion rate of diffusing atoms on the growing surface of the deposited film and the additional thermal energy allows these diffusing atoms to overcome diffusion barriers, effectively smoothing out the surface irregularities and increasing the film density. At low temperatures, diffusing atoms on the surface have little thermal energy to overcome these barriers and "fill in" the gaps in the forming surface. Hence, a small hole in an otherwise smooth monolayer can expand as future layers are added to the film. The result is less dense films which provide a less effective barrier to atmospheric oxygen and moisture diffusion. As the temperature of these processes is lowered in order to be commensurate with the thermal requirements of the OLED materials, conditions will need to be altered to compensate for the decrease in film density.

One condition to control is the deposition rate. High deposition rates decrease film density by increasing the rate at which diffusing atoms on the forming surface nucleate and form surface irregularities since a larger number of diffusing atoms on the surface increases the probability of diffusing atoms collide. Dimer, trimer and larger grouping of surface atoms have significantly lower diffusion rates than single atoms and are much less likely to diffuse to gap locations. Conversely, low deposition rates effectively give diffusing atom additional time to diffuse to these locations before nucleating with another atom and becoming effectively immobile (25).

Structural Integrity

Deposition at low temperature tends to increase the porosity of PECVD thin films (26). It has been suggested that the lower substrate temperature leads to lower surface

mobility of deposited radical species during the deposition process. As a result, adsorbed radicals are more likely to arrange in such a manner as to promote microvoids in the growing structure (27). In addition, the chemistry of the growing films can be altered by the lower deposition temperature. It has been observed in a-H:SiN_x films that the concentration of Si-N bonds decreases with decreasing temperature (28), suggesting that lower temperatures promote the inclusion of hydrogen within film structure. The result is less dense, loosely packed films which may have greater oxygen and moisture transmission rates than films prepared at higher temperatures.

Pinhole formation

Pinholes are highly dependent on deposition temperature and substrate conditions (29). Surface tension due to surface morphology or particulate contamination can seed small gaps in the growing surface. At the edge of these gaps, surface tension inhibits the diffusion of atoms in to these gaps, thus enlarging the pinhole as the surface forms. This process is exacerbated by low substrate temperatures leading to high pinhole density at deposition condition below 300˚C (30) .

Particulate contamination

Particulate contamination of barrier films greatly decreases the efficacy of the barrier (15). Larger contaminants (whose dimensions exceed the thickness of the thin film) degrade the efficacy of the barrier by becoming dislodged from the TFES during device operation. This leaved a hole in the encapsulation, through which oxygen and moisture can easily diffuse and degrade the cathode-organic interface, or quench luminance within the emission layer. When the dimensions of the particulate contaminant are on

the order of or smaller than the thickness of the film, contaminants are permanently embedded within the film. Though they do not dislodge, they greatly decrease the overall density of the film which leads to increased oxygen and moisture diffusion.

Particulate contamination is mainly a function of sample handling and chamber cleanliness (31), however, it should be noted that in low temperature processes, particle formation within the chamber seems to occur with greater eagerness. The most likely explanation for this comes from the larger porosity of films grown on the upper electrode and walls of the chamber at low temperatures (31). The deposition process deposits films on both the upper and lower electrodes, since ions formed within the plasma are accelerated towards both negatively charged electrodes. However, only the bottom electrode is heated and, while the temperature of the upper electrode is raised somewhat by conduction of heat from the lower electrode through the chamber, or by radiation, there is a large difference in temperature between the electrodes. This results in a much higher porosity in the growing film on the upper electrode and, in turn, a much less mechanically robust film. This may be a design feature of PECVD tools, as the reduced mechanical stability of this film makes the upper surface easier to clean, but as the temperature decreases, the likelihood of small particles becoming dislodged and seeding larger particles as they fall through the plasma increases.

Particles take on a negative charge within the plasma and are suspended by electrostatic forces along the plasma sheaths (32) (33). If the particles grow large enough, gravitational force will overcome electrostatic force and the particle will fall to the surface where the negative charge will attract the positive reactive species diffusing

on the surface. Otherwise, the particles will remain suspended over the wafer until the RF excitation of the plasma is removed and the particles fall to the wafer.

The inclusion of particles in the growing film alters the morphology of the surface which leads to high localized surface tension around the contaminant. This can thin the encapsulation around the particle forming areas of diminished barrier quality, or the particle can form the seed for stress-induced cracking and/or buckling. In addition, if the particle is large enough, it may become dislodged after deposition, leaving a large hole in the encapsulation though which atmospheric oxygen and moisture may diffuse to the organic device. Regardless, the higher contamination rate spurred on by lower temperature deposition and the increased likelihood of particulate contamination as the deposition time is increased, requires a balance between the maximum film thickness possible within a single deposition and the necessity for particle-free films.

High compressive stress

Because of the difference in thermal expansion coefficients of the PECVD film and the substrate (Si = 2.49 µm/m-°C, SiNx = 2.80 µm/m-°C, SiOx = 8.10 µm/m-°C, at 25°C (34)), compressive films are to be expected at low deposition temperatures (35). The film stress, as measured after deposition, can be expressed as (36):

$$\sigma_f = \left(\alpha_f - \alpha_s\right)\left[\frac{E_f}{(1-\nu_f)}\right](T_d - T) + \sigma_i \tag{6-2}$$

where α_f and α_s are the thermal expansion coefficients for the film and substrate, respectively. E_f is the elastic constant of the film, ν_f is the Poisson's ratio of the film, T_d is the deposition temperature, T is the temperature at which the sample was measured

and σ_i is the intrinsic stress of the film. Consequently, as the deposition temperature is lowered, the film stress is reduced as well. Residual stress in PECVD films is a critical parameter as highly stressed films are subject to a number of failure mechanisms.

Stress-Induced Failure

Thin films with high residual stress, both tensile and compressive, are subject to cracking. In tensile stressed films, cracks will form as a local region of the film contracts. If the adhesion of the film to the surface is poor, this will be accompanied by delamination as the edges of the crack are pulled away from the surface. Compressive stressed films fail depending on the adhesion of the film to the surface. If the adhesion is good, spalling can occur as the lateral stress forcibly ejects a portion of the film outwards. If the adhesion is poor, the film can buckle as segments of the film delaminate from the surface. These failure mechanism are depicted in Figure 6-7.

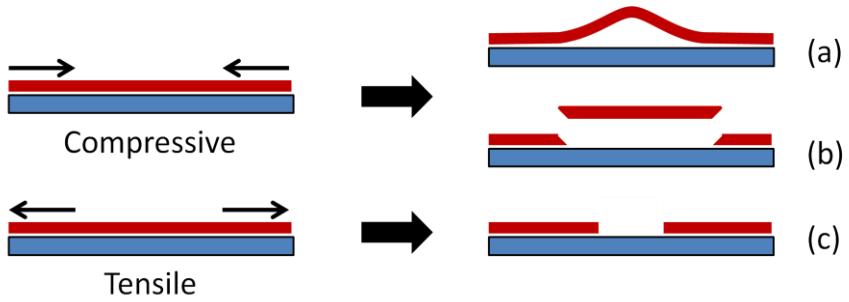

Figure 6-7: Schematic of stress-induced film failure. Compressive stress with poor film adhesion leads to buckling (a); compressive stress with good adhesion leads to spalling (b); tensile stress can lead to film cracking (c).

Although intrinsic stress can be influenced by the surface morphology of the substrate, the flat surfaces involved in OLED fabrication leave PECVD deposition conditions as the primary factor determining residual stress in films. It is generally possible to adjust the PECVD deposition conditions (temperature, RF power, gas concentration and pressure)

to produce stress free silicon nitride and silicon oxide films (31). However, in order to be commensurate with the properties of the organic materials in use, the temperature for these processes must remain low.

Amorphous Silicon Oxide Deposition Chemistry

a-H:SiO_x is deposited through the reactive combination of silane (SiH_4) and an oxygen source, such as nitrous oxide (N_2O) (37). Although, a-H:SiO_x can be produced with other sources of oxygen than N_2O, the reaction between SiH_4 and molecular oxygen (O_2) is highly energetic and produces excessive heat within the deposition chamber. Non-reactive gasses are sometimes added to the chamber to help establish dense plasma. Electron bombardment within the plasma dissociates the process gasses in to a menagerie of molecular species. The most important of which are those radical species which either diffuse to the substrate surface and react directly, or which form chemical precursors which, subsequently diffuse to the substrate. The primary radical formed are $\bullet\ SiH_n$ and $\bullet\ O$. In the presence of a high concentration of hydrogen, hydroxyl radicals, $\bullet\ OH$, are produced, leading to the formation of silanol molecules ($Si(OH)_n$) within the plasma (38). These silanol molecules are incorporated within the growing film and lead to highly polar segments of the silicon oxide network which act as a bridge for moisture diffusion within the film. The most desirous reaction for the purposes of forming dense films occurs between the radicals $\bullet\ SiH_n$ and $\bullet\ O$ after mass transport has brought them to the substrate surface.

Amorphous Silicon Nitride Deposition Chemistry

a-H:SiN_x is deposited through the reactive combination of silane, ammonia (NH_3), and molecular nitrogen (N_2). Non-reactive gasses (He, Ar) are sometimes used to establish the plasma. Within the plasma, the three reactive gasses dissociate according to the following

$$NH_3 + e^- \rightarrow \begin{matrix} NH + H_2 + e^- \\ NH_2 + H + e^- \end{matrix} \quad (6\text{-}3)$$

as well as the radical species of each product.

When the reaction consists of species originating from SiH_4 and NH_3, the formation of precursors precedes the development of the a-H:SiN_x film. The most prevalent of these precursors comes from the reaction of the radical species of SiH_2 and NH_2 to tetra-aminosilane and the radical triaminosilane:

$$\begin{matrix} \bullet\, SiH_2 + 3 \bullet\, NH_2 \rightarrow \bullet\, Si(NH_2)_3 + H_2 \\ \bullet\, Si(NH_2)_3 + \bullet\, NH_2 \rightarrow Si(NH_2)_4 \end{matrix} \quad (6\text{-}4)$$

Radical triaminosilane and tetra-aminosilane react on the surface of the substrate and form the nitride film as NH_2 is eliminated from the film. Since silane dissociates more readily than ammonia, the formation of radical triaminosilane and tetra-aminosilane is highly dependent on the silane/ammonia ratio (39). When this ratio is high, disilane (Si_2H_6) tends to form, leading to silicon-poor, porous films.

When the reaction consists of species originating from SiH_4 and N_2, no precursors are formed (40) (38). Instead, Si-N bonds are created through surface reactions between $\bullet\, Si$ and $\bullet\, N$ on the substrate. Depositions consisting only of SiH_4 and N_2 would, as a result, contain fewer N-H bonds because of this lack of N-H-laden precursors (41).

Amorphous Carbon Deposition Chemistry

a-C films can be produced via PECVD (22) from a large array of carbon sources. The deposition rates of the a-C films largely depend on the ionization potential (IP) of the precursor gas with high IP gasses, such as methane (IP=12.615 eV (42)) having relatively low deposition rates and the deposition rate increasing linearly as the IP decreases.

The primary qualities which determine the properties of the a-C film are the ratio of sp^3 to sp^2 bonding and the inclusion of hydrogen within the film. Indeed, the composition of a-C films can be presented on a ternary phase diagram as shown in Figure 6-8 (22). Higher percentages of sp^3 bonds yield films with higher mechanical hardness and chemical and electrochemical inertness. Diamond, for example, contains 100% sp^3 bonds with no incorporated hydrogen and has a density of 3.515 g/cm^3 and a hardness of 100 GPa (43). Conversely, higher percentages of sp^2 bonds lower the mechanical strength of the film. Glassy carbon is composed entirely of sp^2 bonds and has a density of 1.3 g/cm^3 and a hardness of 3GPa. The incorporation of hydrogen in to the films is also a cause of decreased mechanical robustness.

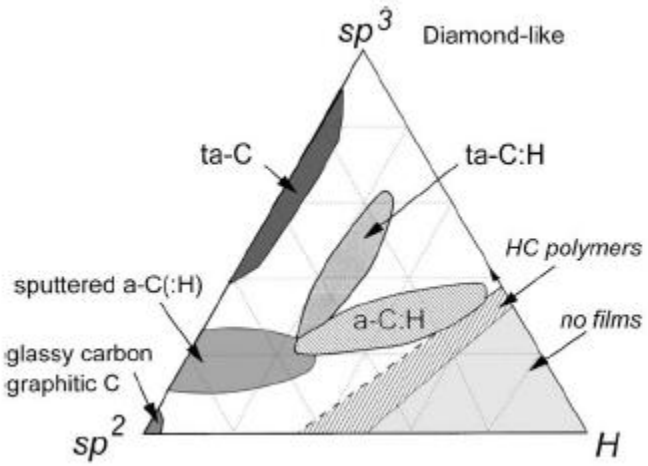

Figure 6-8: Ternary phase diagram for amorphous carbon films

The ratio of sp^3 to sp^2 bonding is highly dependent on the ion energy per carbon atom. Ion bombardment is the key physical process which leads to high fractions of sp^3 bonding and, thus, to mechanically robust films (44). In capacitively coupled PECVD tools, the ion energy is determined by the RF power, which establishes the DC bias voltage between the substrate and the plasma. The highest fractions of sp3 bonds are produced with high bias voltages which produce ion energies of about 100 eV (22).

This is an important property for the development of films to be used with organic devices. High energy ions incident on soft organic substrates can damage the films by implanting in the film, producing conduction pathways and quenching centers or by causing chemical changes to the delicate organic film. It is clear that high quality a-C films can only be incorporated in to encapsulation schemes after the deposition of a buffer layer to protect the organic device.

Encapsulation Failure Mechanisms

Thin film encapsulation can fail by a number of mechanisms which can be broadly classified in to two categories: 1) failure by mechanical faults and 2) failure by chemical, physiochemical and electrochemical faults. A third category could be said to be a combination of the first two categories, such as adsorption-induced stress corrosion cracking, which has been widely studied in silica glass and amorphous silica (45) (46).

Water Adsorption

The adsorption of water proceeds by hydrogen bridging at dangling hydrogen bonds on the film surface. This can lead to further chemical degradation of the encapsulation by hydrolysis. Hydrolized Si-O and Si-N bonds form silanol which, due to its high polarity,

bind to water molecules increasing the moisture diffusion rate and, as a result, the absorption of moisture in to the film. Inorganic films, similar to organic films, swell when suffused with moisture, stressing the film and leading to fracture.

Oxidant Absorption

Water, oxygen and small ionic impurities diffuse, albeit slowly, in to the inorganic films causing internal corrosion which can severely degrade the quality of the films. As has been noted, this process is often started and exacerbated by the adsorption of moisture to the encapsulation surface. Silanol formation, a phenomenon in surface adsorption, also becomes a problem for film quality as moisture and ions diffuse in to the film as silanol formation tends to eliminate nitrogen and silicon from the film. While absorption is an important concern for the longevity of encapsulant films, the diffusion constant of ions and moisture in inorganic films such as silicon oxide and silicon nitride is on the order of 10^{-18} cm^2 s^{-1} (47) (48), which means that failure of encapsulation will most likely be cause by faster processes such as stress cracking and dislodging of particulate contaminants. Never-the-less, as the efficacy of encapsulation schemes improve, these chemical mechanisms will have increasing influence over the lifetime of passivated OLEDs.

Development of Low Temperature Encapsulation Schemes

Strategically, the development of effective encapsulation schemes first involves the development of high quality thin films at low temperature. Much of the work done in this project is devoted to that step. Once high quality films have been developed they are used to build up stacks of thin films until a multi-layered structure has been

fabricated atop the organic devices. Thus, the first step consists of developing low temperature recipes for silicon nitride and silicon oxide. This work proceeded using the GSI PECVD tool located in the MNF at the University of Michigan. As suggested above, the main focus of this segment of work was to produce low stress films with little particulate contamination.

Development of Amorphous Silicon Nitride and Amorphous Silicon Oxide Films

Amorphous Silicon Oxide Films Using GSI PECVD Tool

Amorphous Silicon oxide was produced by flowing a small amount of siliane with an overabundance of nitrous oxide (N2O). Helium (He) was added to the chamber to help establish dense plasma. Table 6-1 show the deposition conditions and the resultant film properties for silicon nitride deposited in the GSI PECVD tool. At low temperature, it is important to prevent the formation of silanol molecules within the plasma. Thus, the ratio of nitrous oxide to silane was set very high (>44) to ensure that the plasma composition has an abundance of oxygen radicals relative to hydrogen radicals. This promotes the formation of Si-O bonds over reactions between silicon and hydroxyl radicals.

GSI PECVD – Silicon Oxide

SiH_4 (sccm)	45	Deposition Rate (Å/s)	92.96
N_2O (sccm)	2000	Index of Refraction	1.54
He (sccm)	250	Film Stress (MPa)	-41.9 (compressive)
Pressure (Torr)	2.6		
RF (W @ 13.56 MHz)	300		
Temp (C)	100		

Table 6-1: Deposition conditions and film properties for silicon oxide deposited in the GSI PECVD tool

The deposition rate for this recipe was found to be almost 93 Å/s. The index of refraction for these films was found to be 1.54, which can be indicative of hydrogen content, porosity or the ratio between SiO and SiO_2 type bonds. Pure SiO_2 has an index of refraction of 1.42 while higher indices of refraction are associated with higher concentrations of SiO type bonds (49). The ratio of SiO to SiO_2 bonds can be controlled by varying the partial pressure of silane in the chamber during deposition (50). This ratio, however, was not a parameter under study as the concentration of defects in the deposited film was of far greater consequence to the overall efficacy of the barrier film.

The residual stress of 1000Å films produced from the above recipe was found, at room temperature, to be -41.9 MPa (compressive). Stress-free a-H:SiO_x films have been fabricated with tetramethylsilane (51) as the reactive gas, but films produced from mixtures of SiH_4 and N_2O tend to be compressive only. Rapid thermal annealing has been shown to significantly reduce residual stress in a-H:SiO_x films and even reverse the radius of curvature for deposited films, changing compressive films to tensile (52). This process, however, involves substrate temperatures of up to 900˚C, which is unsuitable for use in the passivation of OLEDs. During this work, no process was found which produces stress-free or tensile a-H:SiO_x films.

Figure 6-9 shows the FTIR spectra of a-H:SiO_x deposited at low- and high-temperatures in the GSI PECVD tool. Stoichiometric films of silicon oxide have three peak representing the SiO wagging (450cm^{-1}), stretching (1080 cm^{-1}), and bending (800 cm^{-1}). The incorporation of hydrogen produces a number of peaks between 2000 cm^{-1} and 2265 cm^{-1} and, if silanol (Si-OH) is present, a peak at 3650 cm^{-1}. Both spectra exhibit strong

Si-O absorption peaks with moderate amounts of hydrogen absorption as indicated by numerous small peaks in the 2000-2265 cm^{-1} range, though there is not a significant increase in the intensity of Si-H relative to the Si-O peak strength. This indicates that hydrogen incorporation in to low-temperature PECVD oxide films is not a significant barrier to the production of films for barrier applications.

Si-OH absorption (3620 cm^{-1}) is more significant in the high temperature film than in the low temperature film. This is an indication of silanol incorporation. Highly polar, silanol bonding is known to enhance absorption of moisture by the oxide film by binding to adsorbed water molecules. This may be an indication that the high oxygen to silicon ratio in the process gasses is an effective means for preventing silanol incorporation within oxide films.

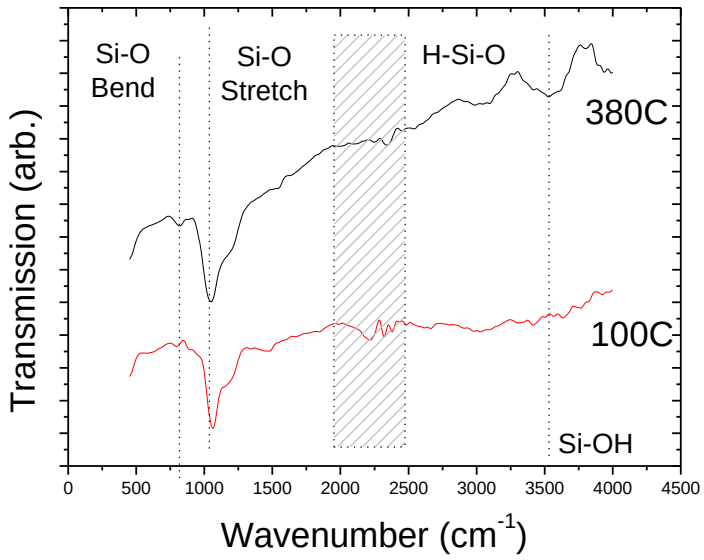

Figure 6-9: FTIR of SiOx deposited at high and low temperature in the GSI PECVD

Amorphous Silicon Nitride Films Using GSI PECVD Tool

The deposition parameters of a-H:SiN_x films were widely varied in order to the effect of deposition parameters on film quality. Low temperature nitride films were produced in the GSI PECVD tool with an ammonia:silane ratio ranging from 4.3:1 to 20:1. An overpressure of nitrogen was also used in these processes to ensure the complete conversion the added silane. Helium was also flowed during deposition. The pressure was varied from 1.4 to 2 torr with an RF power at 13.56 MHz of ranging from 300 to 500W and auxiliary RF power at 400 kHz was varied from 40 to 60W. Table 6-2 shows the deposition conditions and film properties for samples prepared.

Sample ID	Temp (C)	SiH_4 (sccm)	NH_3 (sccm)	N_2 (sccm)	He (sccm)	Press (torr)	RF1 (W @ 13.56 MHz)	RF2 (W @ 400kHz)	Refractive Index	Residual Stress (MPa)
D1	130	51	990	500	250	2	400	40	1.734	-136.4
D2	130	51	990	500	250	1.8	400	40	1.761	-316
D4	130	51	990	950	250	1.5	500	60	1.784	-687.4
D6	130	93	400	950	250	1.5	320	60	1.95	-209.5
D7	130	93	400	950	250	1.8	320	60	1.782	-124.3
D8	130	93	400	950	250	1.4	320	60	2.039	-266.2
D9	100	93	400	950	250	1.4	320	60	1.75	-197.2
D10	100	93	400	950	250	1.5	320	60	1.771	-212.2
D11	100	93	400	950	250	2	320	60	1.773	10.35
D12	100	93	400	950	250	2.6	320	60	1.795	-98
D3	100	93	400	950	250	2.6	320	60	0	-41.35
A	100	93	400	950	250	1.4	320	60	1.818	-190.4
B	100	93	400	950	250	1.4	320	60	1.798	-134.4
C	100	93	400	950	250	1.4	320	60	1.764	-200
D	100	93	400	950	250	1.4	320	60	1.259	-174.5
E	100	93	400	950	250	1.4	320	60	1.426	-148.7
D(a)	100	93	400	950	250	1.4	320	60	0	
F	100	15	900	950	250	1.4	320	60	0	-193.7

Table 6-2: Deposition conditions and film properties for amorphous silicon nitride deposited in the GSI PECVD tool

Many of the recipes used in this set of samples produced unacceptable levels of particulate contamination. This is most likely due to the abundance of gasses within the chamber during deposition. The GSI PECVD tool is outfitted with mass flow controllers

which are comparatively large for a deposition chamber which can only accommodate a single 4-inch wafer at a time. As a result the full scale gas flow parameters are well above those needed for deposition. In addition, the size of the GSI chamber throttle valve makes control of the chamber pressure below 1 Torr difficult. As a result of these two factors, the chamber contained an overabundance of reactive gasses during deposition, which often led to plasma-phase reactions of the gasses, sprinkling the growing surface with nanoscopic and microscopic particulate contamination.

Figure 6-10 shows stress vs. deposition pressure for films deposited in the GSI PECVD at 100 and 130˚C and with ammonia to silane ratios of 4.3 and 19.4. The data shows a strong tendency to produce highly compressive films, especially at lower pressures. Indeed, only one sample from this set shows tensile stress (100˚C at 2 torr produces films with tensile stress of 10.4 MPa). The stress of samples produced at higher pressures than those reported could not be measured as for thickness above 100nm, the production of particulate contamination increased beyond tolerable levels, making measurement impossible.

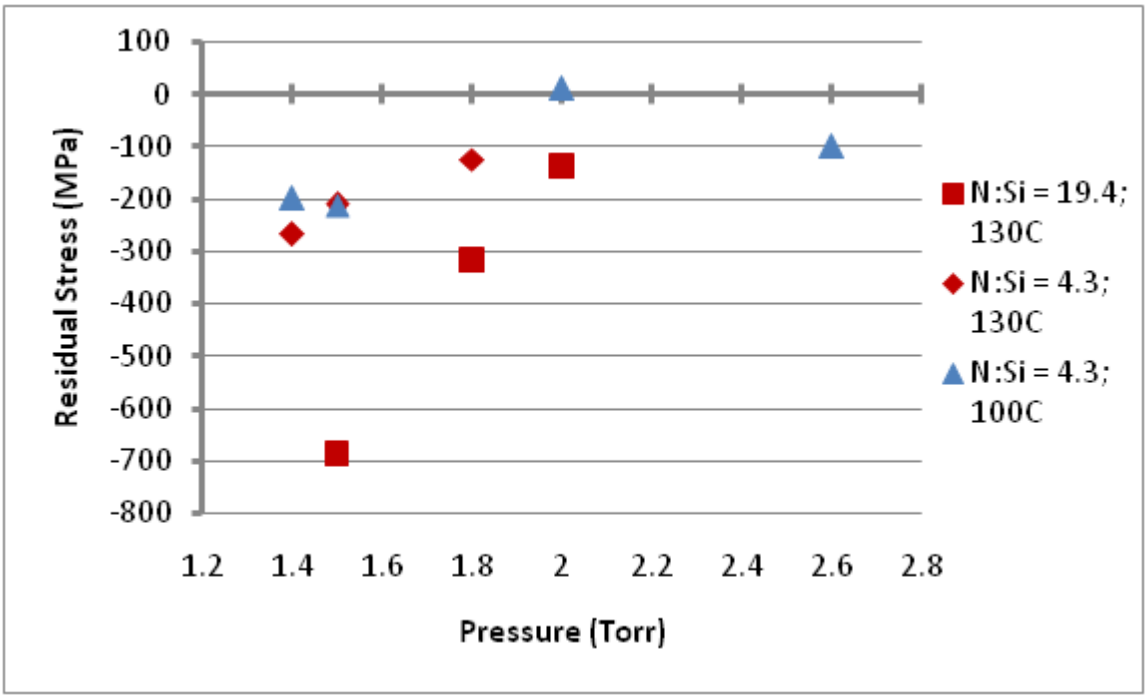

Figure 6-10: Stress vs. Pressure for silicon nitride films deposited at low temperature in the GSI PECVD

The index of refraction, as shown in Figure 6-11, tends to increase with increasing chamber pressure. This is indicative of denser, more silicon-rich films. The target index for stochiometric silicon nitride films is 2.0.

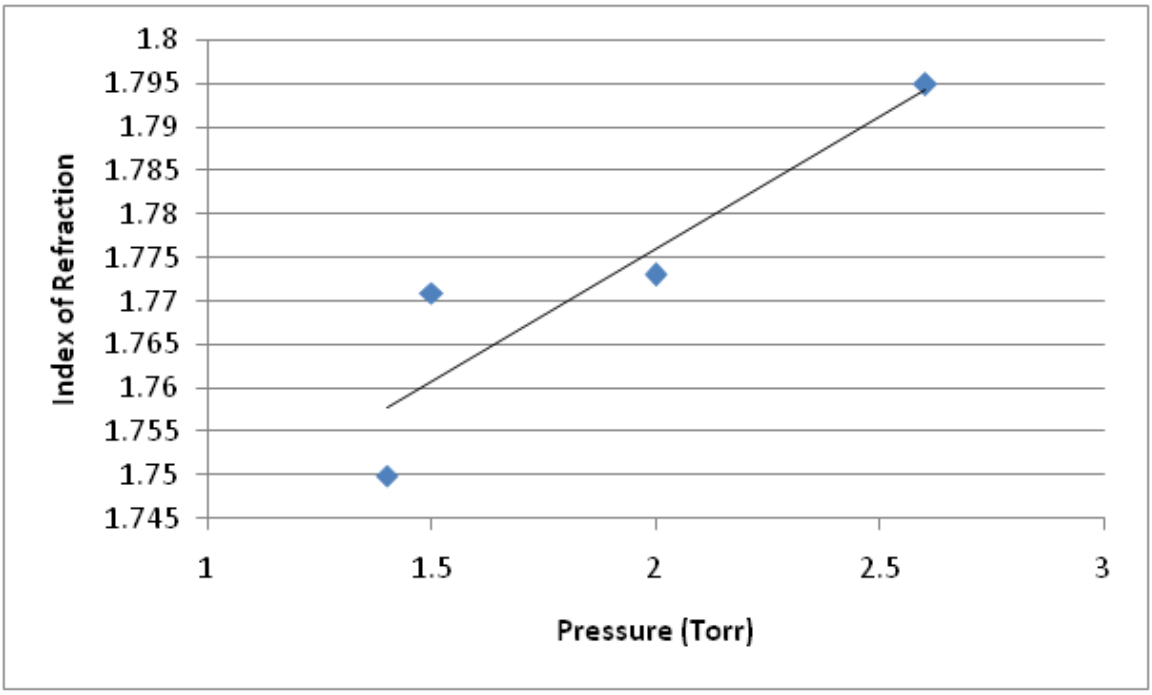

Figure 6-11: Index of refraction vs. chamber pressure for silicon nitride films deposited at low temperature in the GSI PECVD

Figure 6-12 shows the FTIR spectra of silicon nitride films deposited at 100˚C and 380˚C in the GSI PECVD tool. Both spectra show strong absorption peaks at the Si-N stretch mode (865 cm^{-1}). The low-temperature film show significantly higher absorption of atomic hydrogen as the absorption peaks for the N-H wag (1183 cm^{-1}) and N-H stretch (3350 cm^{-1}) modes are much more pronounced when compared to the intensity of the SiN absorption peaks. SiH vibration modes (2000-2265 cm^{-1}) and the NH_2 mode (1550 cm^{-1}) are both present in films regardless of temperature. The higher absorption for the N-H bonds indicates a higher hydrogen content and, hence, a less dense film. The FTIR spectra are not, however, indicative of defect density, a major factor which determines film permeability.

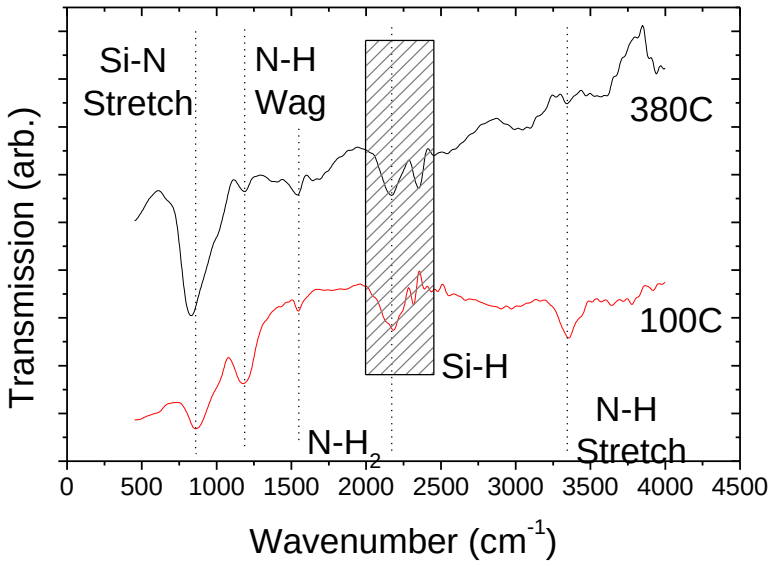

Figure 6-12: FTIR spectra of low- and high-temperature silicon nitride films deposited in the GSI PECVD

Measurement of Encapsulated OLED Samples

Encapsulation schemes were deposited on Alq3-based OLEDs (53). The details of this device are described in Ref. 52. Lifetime testing was performed outside the University of Michigan by placing the devices in an environmental chamber at 85°C and 85% relative humidity and imaged while under operation once a day. The stressing of the devices in the 85°C/85% testing chamber is meant to accelerate the deterioration of the device until it undergoes catastrophic failure. The efficacy of the encapsulation scheme is judged on the longevity of the OLED under these conditions.

Encapsulation with Alternating a-H:SiN_x and a-H:SiO_x films

From the above trials, it was determined that the recipe shown in Table 6-3 in conjunction with the oxide recipe shown in Table 6-1 would provide the greatest chances for successful encapsulation of the OLED samples.

GSI PECVD – Silicon Nitride

SiH_4 (sccm)	51
NH_3 (sccm)	990
N_2 (sccm)	500
He (sccm)	250
Pressure (Torr)	2.0
RF1 (W @ 13.56 MHz)	400
RF2 (W @ 400 kHz)	40
Temp (C)	100

Table 6-3: Final amorphous silicon nitride recipe produced in GSI PECVD tool

In the trials below, OLED samples were fabricated by a collaborator outside the University of Michigan. The samples were transported to Ann Arbor where they were encapsulated within the Michigan cleanroom facility and shipped back to the collaborator for testing. The sample ID for OLEDs which were part of this collaboration begin with the letters 'EM'.

OLED sample EM01 was encapsulated with 6 bilayers of alternating nitride and oxide films. OLED sample EM01-1 was encapsulated with 12 alternating layers of 4000Å films with nitride on the bottom, EM01-2 with 12 alternating layers of 4000Å films with oxide on the bottom, EM01-3 with 12 alternating layers of 6000Å films with nitride on the bottom, and EM01-4 with 24 alternating layers of 2000Å films with nitride on the bottom. All encapsulation schemes were done in the GSI PECVD tool. For each run, the samples were unloaded to a load lock at the midpoint of the deposition and a chamber clean routine was performed. Figure 6-13 (a-d) show the lifetime images for the sample set EM01. Images of the device operation at time 0 hours (having spent no time in the 85°C/85% testing chamber) show a significant number of small dark spots. Most of these spots do not grow in time and are most likely caused by device exposure to moisture before encapsulation. A number of spots, however, grow very rapidly after

exposure to the 85°C/85% testing chamber. These are most likely due to particulate contamination during deposition. After 24 hours of exposure, the dark regions have increased in size. After 48 hours only a single device (EM01-2-D) remains in operation. All encapsulation schemes, at this point, show severe stress-induced buckling, which is the cause of the catastrophic failure. The best results come from sample EM01-2, which shows the least sign of stress-induced buckling. This is most likely due to the natural variation in processing rather than a genuine improvement in encapsulation design.

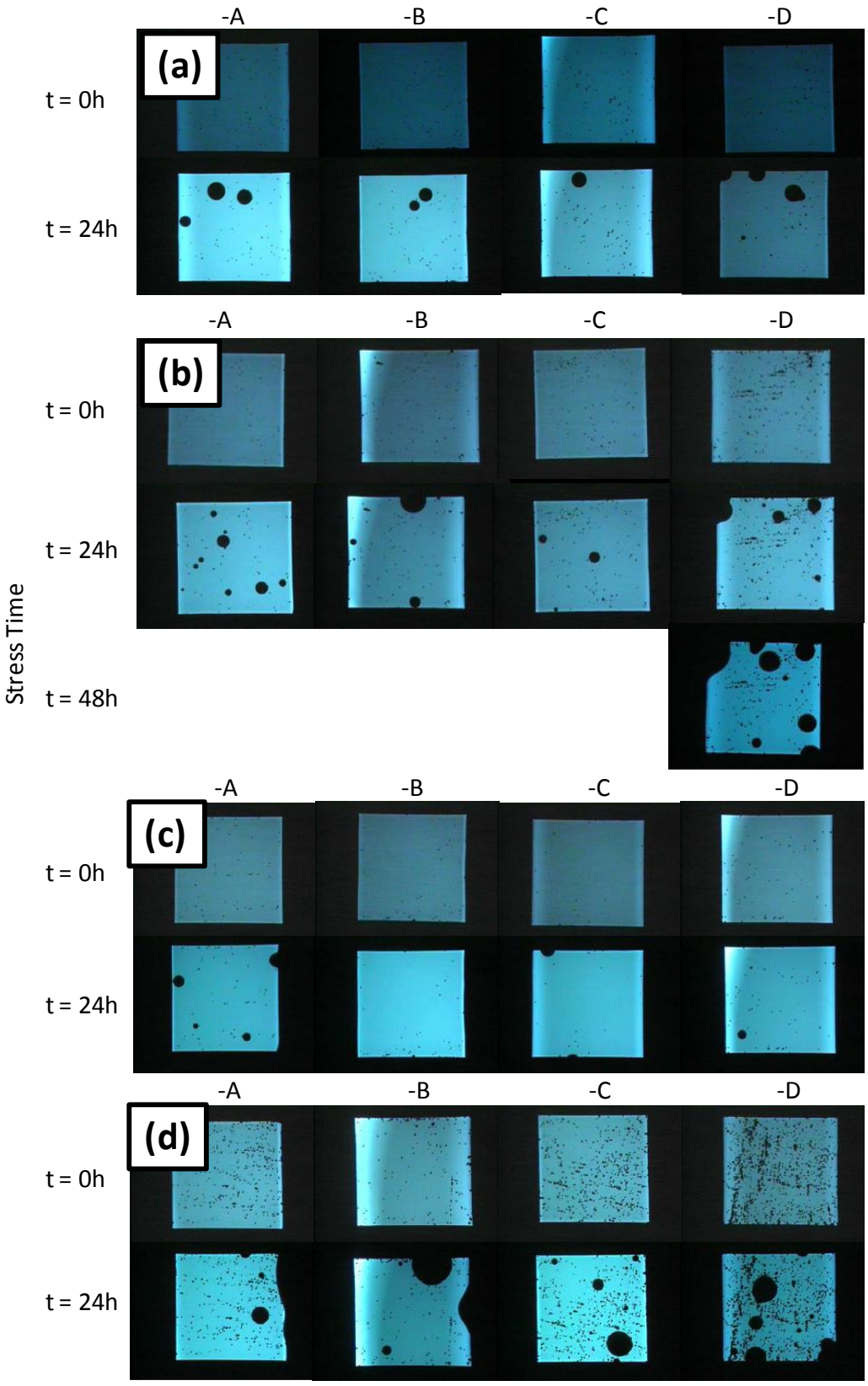

Figure 6-13: Lifetime images of sample set EM01. (a) EM01-1; (b) EM01-2; (c) EM01-3; (d) EM01-4

Figure 6-14: Sample set EM01 showing stress-induced buckling of encapsulation schemes after 48 hours in 85°C/85% testing chamber

Buckling in compressed thin films has been studied extensively and is understood as a mechanism of stress relief (54) (55) (56). It has been shown that delamination of the films precedes buckling and the propagation of the delamination, spurred on by the buckling of the compressed film, depends on the intensity of the film's residual stress, such that no propagation occurs unless the stress exceeds a critical value (55). In addition, buckle initiation is increased by the presence of imperfections in the film surface (56). As a result, the deposition methods used in the above trial, which is suspected to yield high concentrations of particulate contamination as well as highly compressed films, are conducive to the catastrophic film buckling as evidenced in Figure 6-14. From these trials, the need for low stress, clean deposition processes which produce few pinhole defects becomes clear.

Stress-Mitigating Structures

An ideal structure for controlling stress in thick multilayer stacks is one in which alternating tensile and compressive films are deposited. The opposing nature of the

residual stresses (compressive and tensile) effectively cancel out in the stack leaving a stress-free encapsulation. The realization of such a multilayer structures, however, is made difficult by the low-temperature deposition conditions of these encapsulation schemes, as shown in Equation (6-2). Silicon dioxide is typically a compressive film (31) and, while silicon nitride films can be either compressive or tensile, depending on deposition conditions, films deposited at low temperature are typically compressive (-300 – -900 MPa observed from trials). These obstacles necessitate the development of alternative architectures to allow thick TFESs with low residual stress.

Thin films of oxide and nitride at thicknesses of 4000Å, using the best recipes, reveal residual stresses of -41.9 MPa (compressive) and -90.2 MPa (compressive), respectively. However, a TFES comprised of six bilayers of 4000Å oxide / 4000Å nitride (12 layers total, 9.6 μm total thickness) shows a residual stress of only -100.3 MPa (compressive). The fact that the multilayer structure has a residual stress only slightly more compressive than the single silicon nitride layer despite being 24 times as thick and comprised only of compressive films suggests significant stress relaxation at the interfaces of the films.

To take advantage of this, a graded film structure was developed to reduce stress buildup in thick multilayer structures. It is expected that the increase number of interfaces in this structure will also provide a mechanism for stress relief, reducing the tendency of the TFES to buckle. In addition, it is expected that this structure will reduce pinhole formation by providing a clean surface of thin alternating layers (500Å each) on which thicker layers of nitride and oxide can be deposited. The structure: 4×{500Å

Nitride/500Å Oxide} / 4×{1000Å Nitride/1000Å Oxide} / 3×{2000Å Nitride/2000Å Oxide} was deposited on the OLED samples. A chamber clean was performed before the deposition of the 2000Å layers.

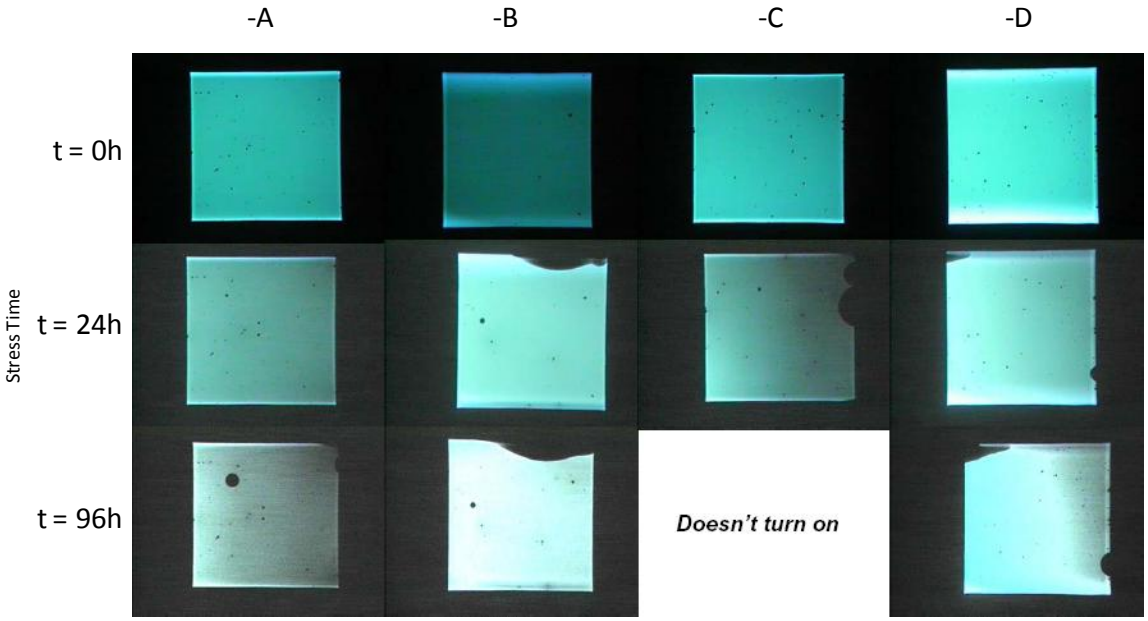

Figure 6-15: Images of sample EM02 as arrived and after 24 and 96 hours in an 85°C/85% testing chamber. No devices turned on after 120 hours

Figure 6-15 shows improved performance of the TFES as compared to the previous sample. Devices are still operational after 96 hours in the 85°C/85% testing chamber. There are few dark spots at t=0 and those present do not expand at an appreciable rate. By hour 96, dark spot formation can be seen to mainly come from the sides of the device, with the exception of OLED –A. Particulate contamination, however, continues to be a consistent problem as seen in dark-field micrographs of the OLED emitting surface before and after encapsulation. In Figure 6-16, the image of the surface before processing exhibits significantly fewer particulate matter than the after image. This particulate contamination, however, does not seem to affect the efficacy of the encapsulation scheme as this contamination does not lead to large dark spot growth as

in the case of sample set EM01. The extended lifetime of these devices can be attributed to the cleaner process accomplished in this run as well as the stress relief efforts used. The catastrophic failure of the devices after 96 hours points to the need for further developments to reduce residual stress in the TFES.

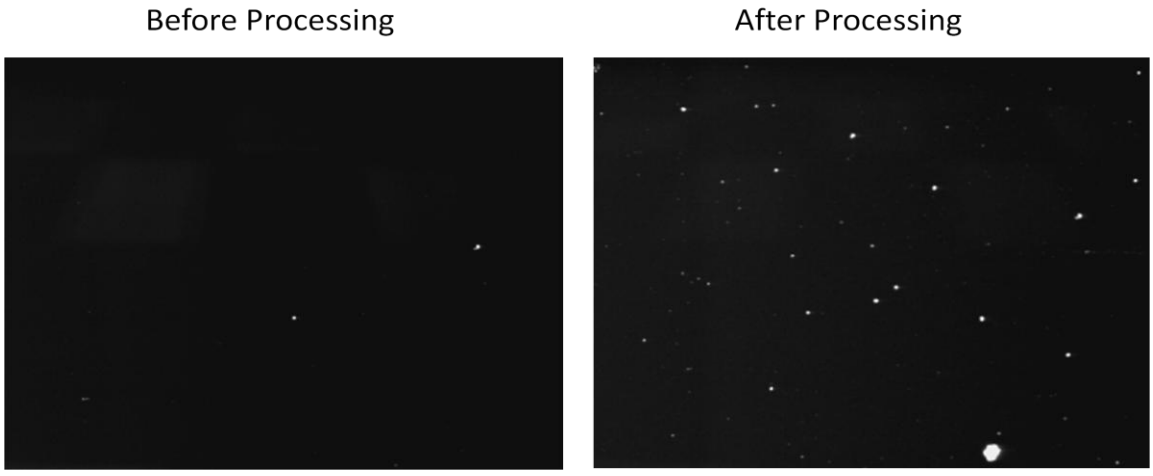

Figure 6-16: Dark-field images of the OLED emitting surface for EM02 showing significan particulate contaminatino after encapsulation

Stress Relief and Particulate Control via Organic Films

The use of organic thin films for encapsulation of OLEDs has been explored previously (57) (58). While the water vapor and oxygen transmission rates for most organic films alone are well below what is required for commercial applications of OLEDs, the incorporation of organic films in to stacks of dense, inorganic encapsulation schemes is expected to enhance the barrier properties of TFES. It has been shown that by using a top polymer coating over alternating layers of silicon oxide and silicon nitride, the WVTR can be decreased by over an order of magnitude (19). This is attributed to the ability of the polymer top coat to seal in particulate matter, embedded in the multilayer stack, preventing the contaminant from becoming dislodged during device operation and leaving a hole in the encapsulation through which atmospheric oxygen and moisture can

diffuse. The ability of the organic film to embed particulate matter rests on the conformal deposition process and low Young's modulus typical of many organic films. Conformal deposition produces organic films which have maximum contact with particulate contamination. A low Young's modulus prevents cracking in the film due to local stresses around the contaminant.

In addition, it has been noted above in equation (6-2), that the residual stress in the inorganic films is dependent on the difference in thermal expansion coefficients of the growing film and the material underneath. For thin films grown on silicon substrates, it has been seen that tensile films are quite difficult to produce. The inclusion of an organic film deposited between the underlying substrate and the inorganic thin films allows for the tailoring of the thermal expansion coefficient contrast, paving the way for low stress deposition.

Parylene Deposition

Parylene C, poly(monochloro-para-xylylene), is a uniquely appropriate organic material for this application. The vapor phase deposition of parylene C produces conformal films with no shadow effect from particulate material without the use of harsh organic solvents. It has a low Young's modulus (<3 kPa) and a thermal expansion coefficient of $3.5\ 10^{-5}\ (^{o}C)^{-1}$ (59).

Parylene C, is a widely used as a conformal coating for printed circuit boards, passivation of semiconductor devices and a coating for biomedical devices. Thin, 0.1 μm films of parylene C have been shown to reduce the transmission of oxygen to 7.2 (cm^3 (stp)·mil)/(100 in^2/d·atm) (ASTM D 1434) at 25˚C and the transmission of moisture to

0.21 (g·mil/100 in2·d) (ASTM E 96) at 90% relative humidity and 37˚C (60). The deposition of parylene proceeds from a vapor phase process and is shown in Figure 6-17. The solid dimer is vaporized at about 150˚C. This gaseous phase is then heated to above 680˚C whereupon the dimer undergoes pyrolysis at the dimer splits at the methylene-methylene bonds. The gaseous, stable monomer, monochloro-para-xylylene, enters the room temperature chamber at a pressure of about 100mTorr. At this pressure, the mean free path of is on the order of 0.1 cm. The gaseous monomer adsorbs and polymerizes on any surface within the chamber. Since polymerization occurs on any surface in contact with the gas, deposition is not limited by line-of-sight and complete conformal coverage can be achieved. The temperature of the chamber never rises more than a few degrees above ambient during the deposition.

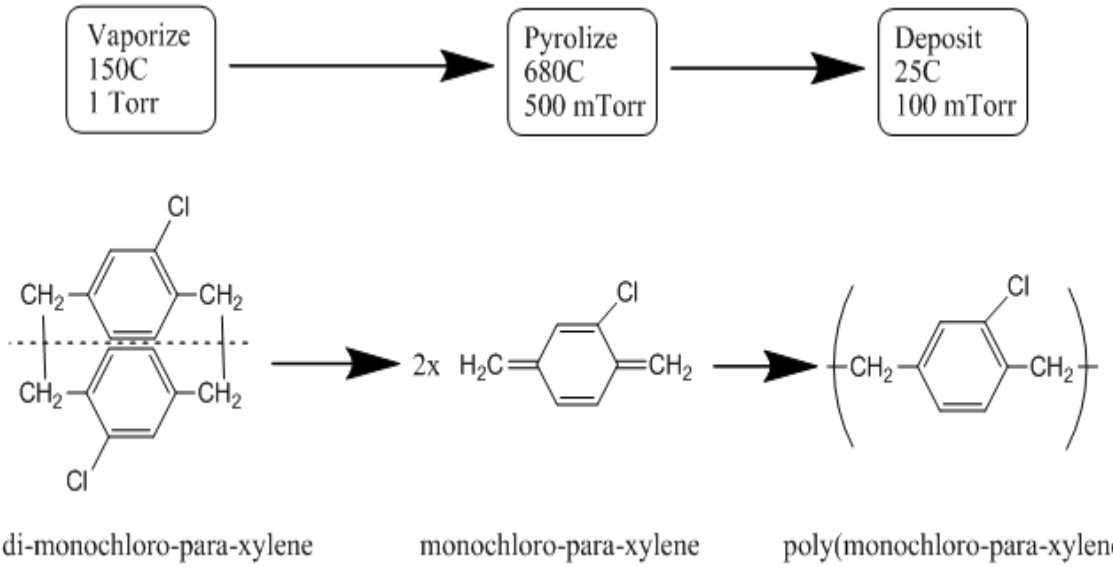

Figure 6-17: Vapor phase deposition process for parylene C

Following the parylene deposition, samples can be transported to other thin film tools for further encapsulation.

Organic Films in Encapsulation Schemes

Sample EM03 was encapsulated with a single layer of parylene, 0.96 µm thick. Figure 6-18 shows the results of placing sample EM03 in an 85°C/85% testing chamber. As expected, a single, thin film of parylene is insufficient as a barrier layer alone. However, is can be seen that the deposition process and the polymerization of parylene on the OLED surface do not cause damage to the device and does provide some barrier against atmospheric oxygen and moisture.

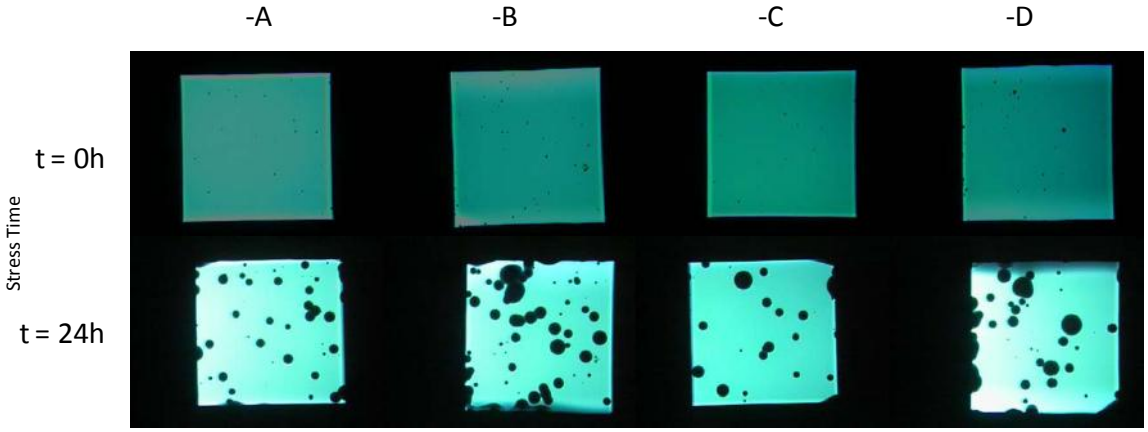

Figure 6-18: Images of sample EM03 as arrived and after 24 hours in an 85°C/85% testing chamber. No devices turned on after 48 hours

To further explore the barrier property gains to be won by particulate control, samples were encapsulated with combinations of PECVD nitride and oxide, sputtered nitride and oxide and parylene. While the conformity of the sputtered layers is not as complete as PECVD films, sputtered films were used because of the process' tendency not to produce particulate matter. Using sputtered films as the initial barrier layers (closest to the devices) will ensure that a clean process is used on the layers closest to the device, which will mitigate the effects of particulate contamination from further processes.

The next set of samples incorporates parylene in to the encapsulation scheme. In addition, these films attempt to limit the deposition of particulate contamination in the early stages of the deposition process by including films deposited by sputtering. Figure 6-19 shows the schematics for the four substrates included in sample set EM04. All sputtered and PECVD films are 2000Å thick. PECVD films were deposited using the recipes described above. Sputtered films were deposited at 700W with a 7×10^{-6} Torr base pressure and 7 mTorr Ar process gas. Sample EM04-1 begins with alternating layers of oxide and nitride with the first two layers being deposited by sputtering and the next three bilayers deposited by PECVD. A film of 1.35 µm parylene film is deposited and then the process is repeated. Sample EM04-2 has only the sputtered layers and the two parylene films (1.35 µm thick, one midway through, one on top). Samples EM04-3 and -4 repeat the schemes of samples EM04-1 and -2, but with the mid-stack parylene film removed.

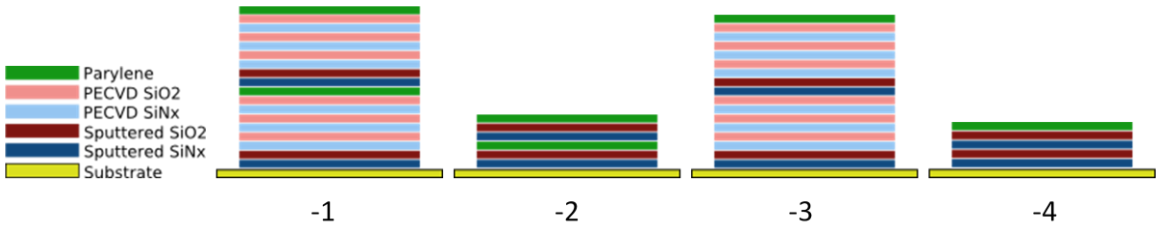

Figure 6-19: Schematics for EM04 incorporating sputtered films and parylene

Figures 6-20 through 6-23 show images of OLED sample EM04-1, -2, -3, and -4 in operation just after encapsulation and then after exposure to the 85°C/85% testing chamber (if the device survived). OLED sample EM04-1 shows great promise since no buckling or dark spot formation can be observed for 168 hours in the 85°C/85% testing chamber. Sample EM04-3 also shows promise, but it is clear that the additional

parylene layer in the first sample enhanced the barrier properties of the stack. OLED samples EM04-2 and -4, on the other hand, did not last past 24 hours in the chamber. From the images, a few points can be made. First, samples which incorporate both sputter-deposited and PECVD-deposited films performed better. Both samples which included only 4 layers of sputtered films showed film cracking after exposure, which is the likely cause of the device failure. This was the case regardless of having one or two layers of parylene as a stress relief layer. Second, a second parylene layer in the middle of the encapsulation stack improves the performance of the TFES. It is likely that the contaminants and defects which developed in the first stage of the encapsulation were largely subdued by the middle parylene layer in sample EM04-1. In sample EM04-3, however, defects created in the first half of the deposition influence the deposition of the second half, thus propagating and resulting in a poorer quality film.

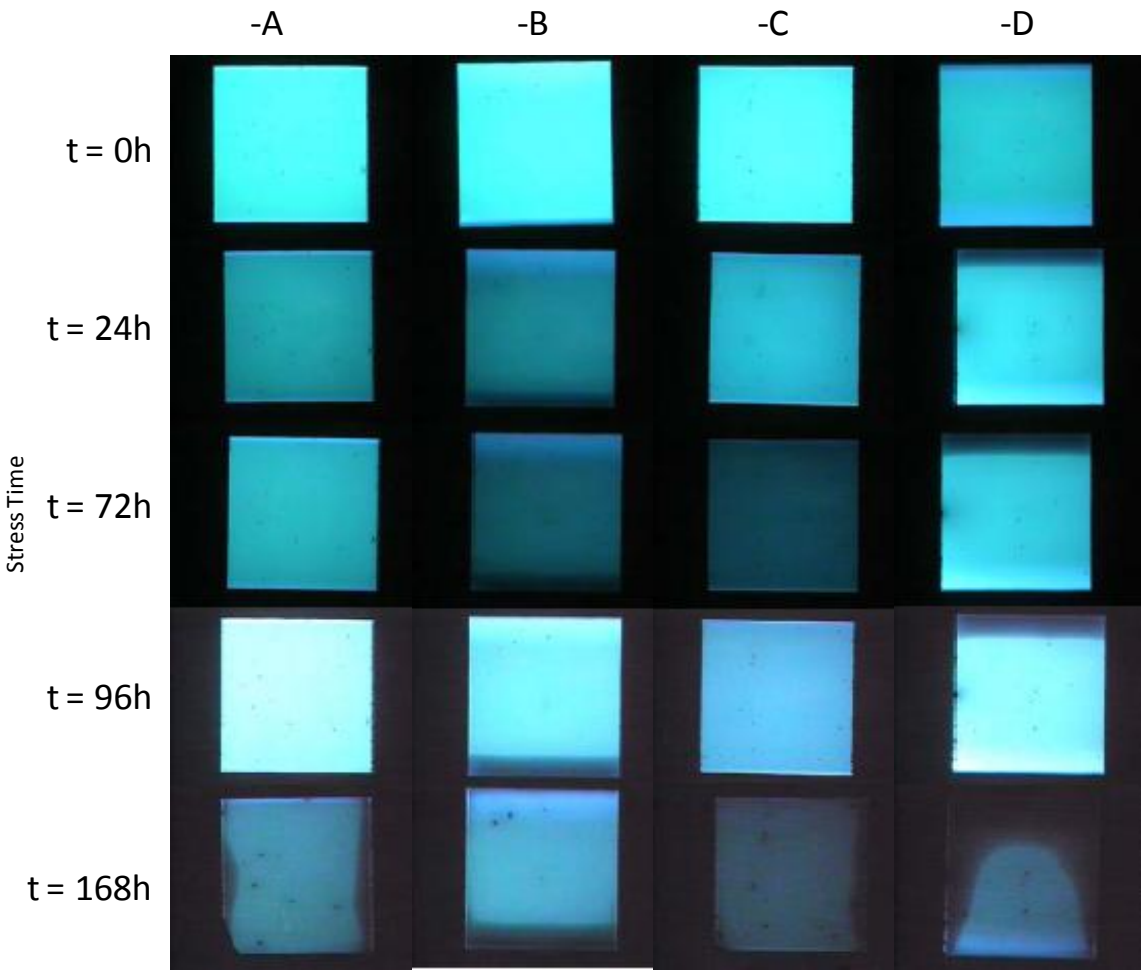

Figure 6-20: Images of OLED sample EM04-1 in operation after exposure to 85C/85% rel. humidity

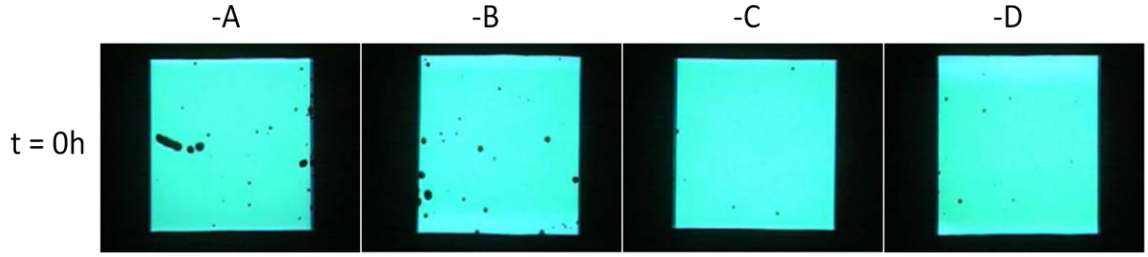

Figure 6-21: Images of OLED sample EM04-2 in operation. The device did not light up after exposure to 85C/85% rel. humidity

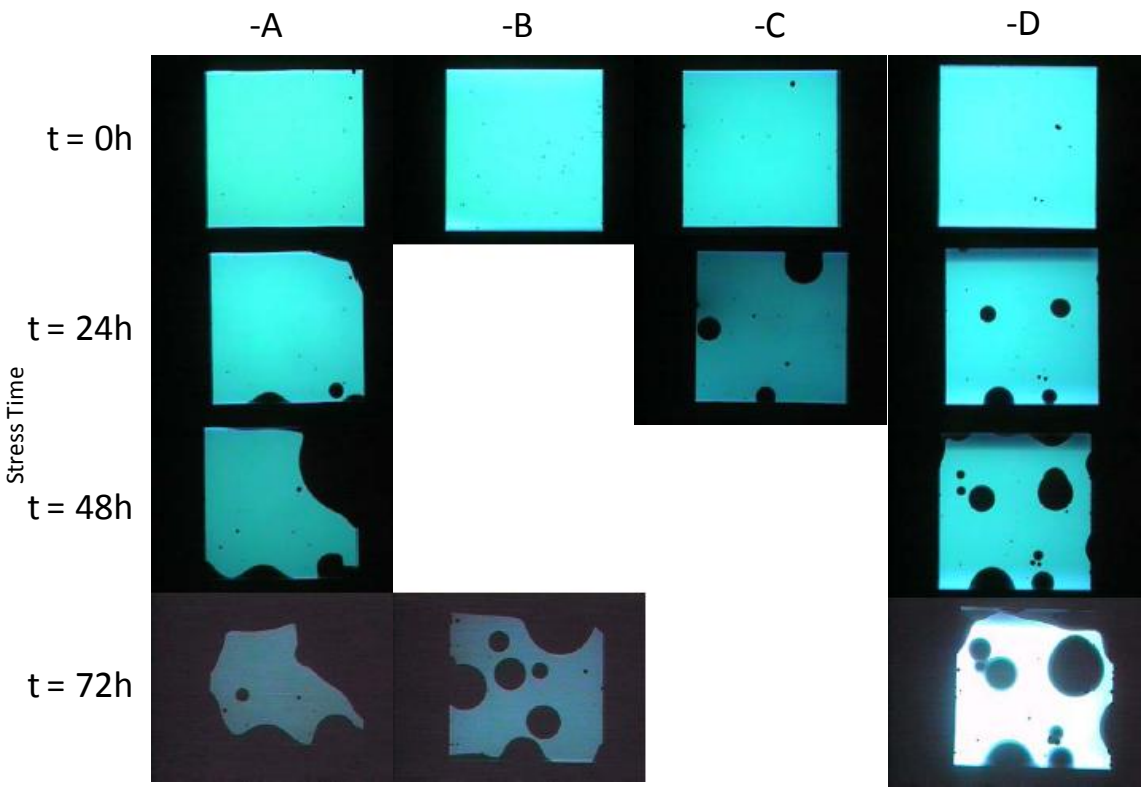

Figure 6-22: Images of OLED sample EM04-3 in operation after exposure to 85C/85% rel. humidity

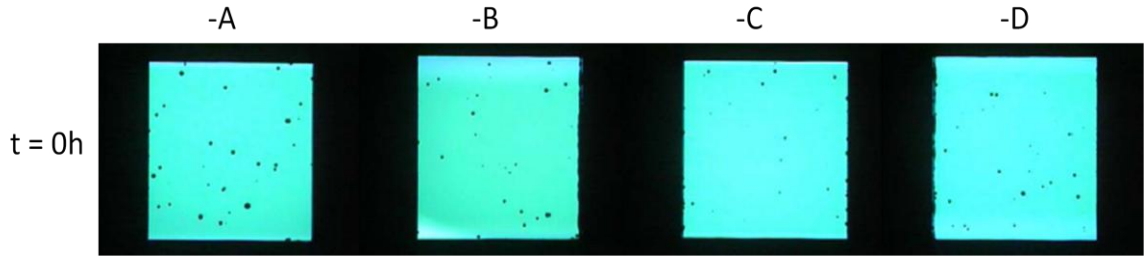

Figure 6-23: Images of OLED sample EM04-4 in operation. The device did not light up after exposure to 85C/85% rel. humidit

The use of parylene for particulate control seems a promising addition to the TFESs. As a stress relief barrier, however, it is not as effective. This is most likely due to the large difference in thermal expansion coefficient between the organic and inorganic layers. To overcome the stress-related issues in TFES, a tensile stress-relief film must be added to the process.

Tensile Amorphous Carbon Films as Stress Relief

Owing to the difficulty of producing tensile nitride or oxide films at low temperature, we explored the possibilities for a third inorganic film, one which exhibits tensile stress when at low temperature deposition. For this, we sought to introduce amorphous carbon to the project. In the initial stages of this project, the University of Michigan did not possess a tool capable of depositing amorphous carbon (a-C). This deficiency has since been rectified with the commissioning of the Plasmatherm 790 PECVD tool, and the addition of a methane gas line. However, much of the initial work with a-C films was performed in the Petit Microfabrication lab at Georgia Tech in Atlanta, GA. The PECVD deposition equipment was an Astex ECR tool. All films produced within the ECR were deposited at room temperature.

Figure 6-24 demonstrates that tensile a-C films can be produced at low temperature by ECR PECVD. The residual film stress increases with increasing chamber pressure. Likewise, the film etch rate in BHF increases with chamber pressure, indicating a decrease in film density. This is supported by the decrease in the index of refraction with increasing chamber pressure, as shown in Figure 6-25. Dense carbon films are characterized by high fractions of sp^3 bonding. High ion energy promotes the formation of sp^3 bonds and, as a result, dense, hard films. Lower deposition pressures increase the DC self bias and, consequently, the average energy of ions bombarding the growing film. Unfortunately, stress measurements were conducted at the University of Michigan after the encapsulation of OLED samples. Thus, while it is clear that for tensile films, a chamber pressure of 50 mTorr should be used, the samples below were made with

recipes that used 20 mTorr. Usually, high compressive stress is associated with high fractions of sp^3 bonding within the film (22) (61). Hence, the production of tensile films likely indicates a low fraction of sp^3 bonding.

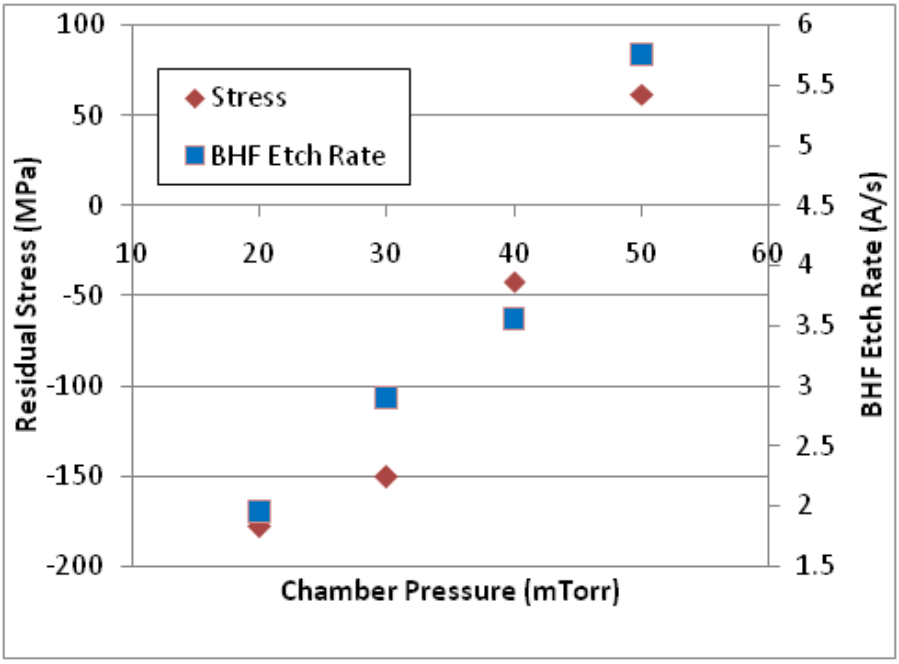

Figure 6-24: Stress and etch rate vs. chamber pressure for amorphous carbon films produced by ECR at Georgia Tech.

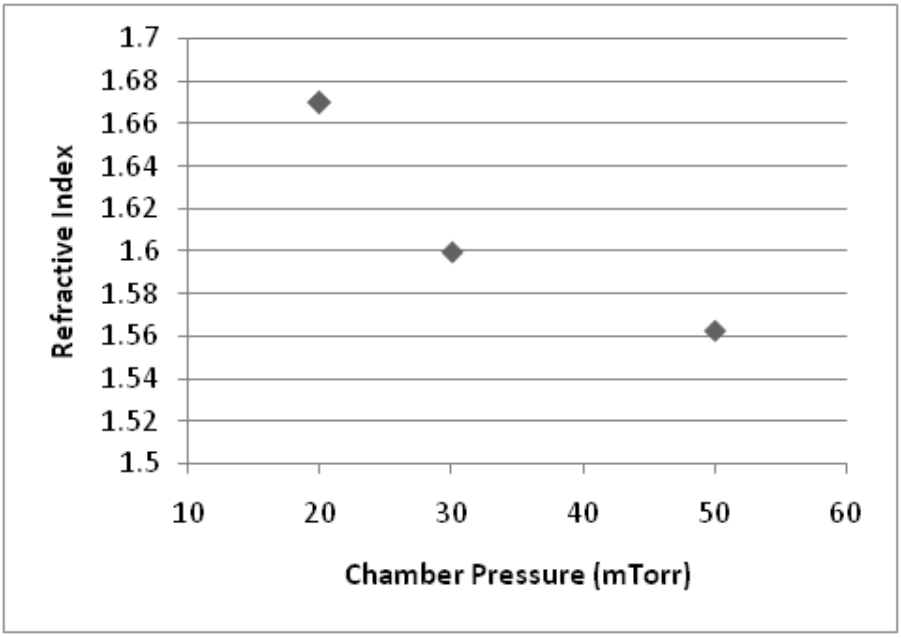

Figure 6-25: Refractive index vs. chamber pressure for amorphous carbon films produced by ECR at Georgia Tech

Table 6-4 shows the deposition conditions used to deposit amorphous nitride and amorphous oxide films using the ECR tool. These recipes were adapted only moderately from the default recipes found preloaded in the tool software.

	ECR Silicon Nitride	ECR Silicon Oxide	ECR Carbon
SiH_4 (sccm)	1	2	
C_2H_4			45
N_2O (sccm)		700	
N_2 (sccm)	39	18	
He (sccm)			
Ar (sccm)	17.5		25
Pressure (mTorr)	20	50	20 / 50*
µWave (W)	300	600	800
Deposition rate (Å/s)	3.10	10.83	10.01
Index of Refraction	1.92	1.678	1.655

Table 6-4: Recipes for silicon nitride and silicon oxide used in the ECR tool at Georgia Tech. *50 mTorr is the pressure which produces tensile films. This was not known at the time the carbon samples were produced. The 20 mTorr recipe was used instead.

To confirm the compatibility of the above processes with the OLED devices, OLED samples EM05-1 and -2 were encapsulated with a single 2000Å film of a-C and a bilayer of 2000Å a-C and 2000Å nitride, respectively. Also, sample EM05-4 was encapsulated with 6 bilayers of 2000Å nitride/2000Å a-C. In the latter samples, nitride was deposited first, directly atop the devices. Figure 6-26 (a) shows the results from encapsulation with a single carbon layer. At t=0, there are a few dark spots forming. After 24 hours in the 85°C/85% testing chamber, the spots have grown considerably, indicating that carbon alone is not a sufficient barrier. Beyond 24 hours, severe cracking in the film was observed over the entire area of the sample and the devices ceased to light up. Figure 6-26 (b) shows the results of encapsulation with the nitride/carbon bilayer. This sample did not fare as well as the previous sample. Images taken at t=0 show that the device does light up, thus the deposition process does not damage the device. The observed

dark spots in these images are slightly larger than those of sample EM05-1, but some devices, like EM05-2-D show relatively few and small initial dark spots. This sample, unlike EM05-1, did not light up after 24 hours in the 85°C/85% testing chamber and showed severe cracking and buckling, but only over the area where organic material has been deposited. OLED sample EM05-4 met with the same fate.

It was noted above, that tensile carbon films can be produced with a chamber pressure of 50 mTorr and that this fact was not known at the time of the sample encapsulation. Thus, OLED sample EM05-2 and -4 have multiple compressive films applied to them. The increased compressive stress is the most likely cause of the premature failure of this sample.

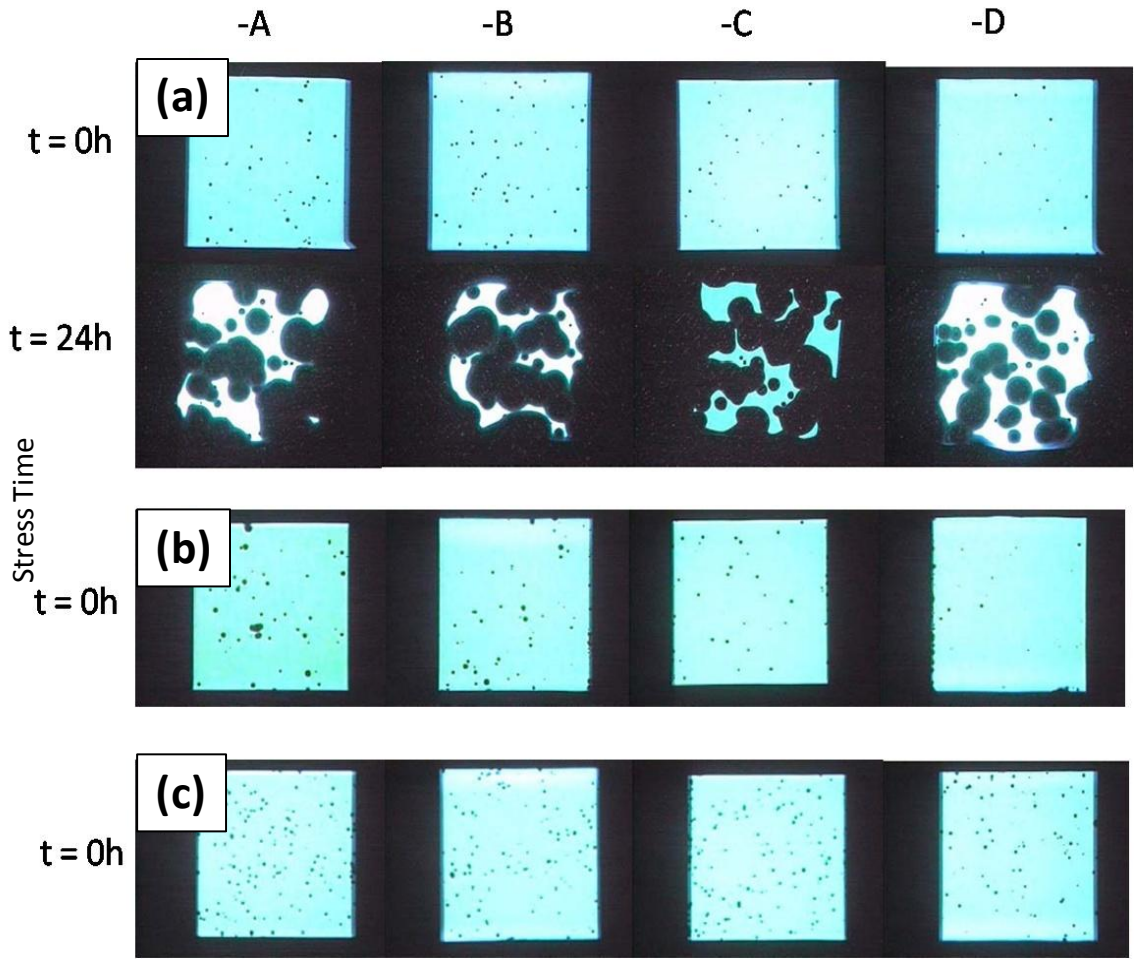

Figure 6-26: OLED sample set EM05 images taken upon arrival and after 24 hours in an 85°C/85% testing chamber. (a) EM05-1 encapsulated with 2000Å a-C; (b) EM05-2 encapsulated with 2000Å nitride/2000Å a-C; (c) EM05-4 encapsulated with 6 bilayers of 2000Å nitride/2000Å a-C.

The incorporation of oxide and parylene films in to the TFES did not improve the quality of the barrier films while compressive carbon films were used. A number of samples were encapsulated with various combinations of oxide, nitride, carbon and parylene. OLED sample set EM06 is shown in Figure 6-27(a)-(d). EM06-1 is encapsulated with {1000Å each of nitride/oxide/carbon} ×2 /2 µm parylene/{1000Å each of nitride/oxide/carbon} ×2 /2 µm parylene. EM06-2 is encapsulated with {1000 Å each of nitride/carbon} ×3/2 µm parylene/{1000 Å each of nitride/carbon} ×3/2 µm parylene. EM06-3 is encapsulated with {1000 Å each of nitride/oxide} ×3/2 µm parylene/{1000 Å

each of nitride/oxide} ×3/2 µm parylene. EM06-4 is encapsulated with 2 µm parylene/{1000Å each of nitride/oxide/carbon} ×4/2 µm parylene. All samples in this sample set show moderate amounts of particulate contamination. The high stress involved in the encapsulating films caused severe buckling after 24 hours in the 85°C/85% testing chamber.

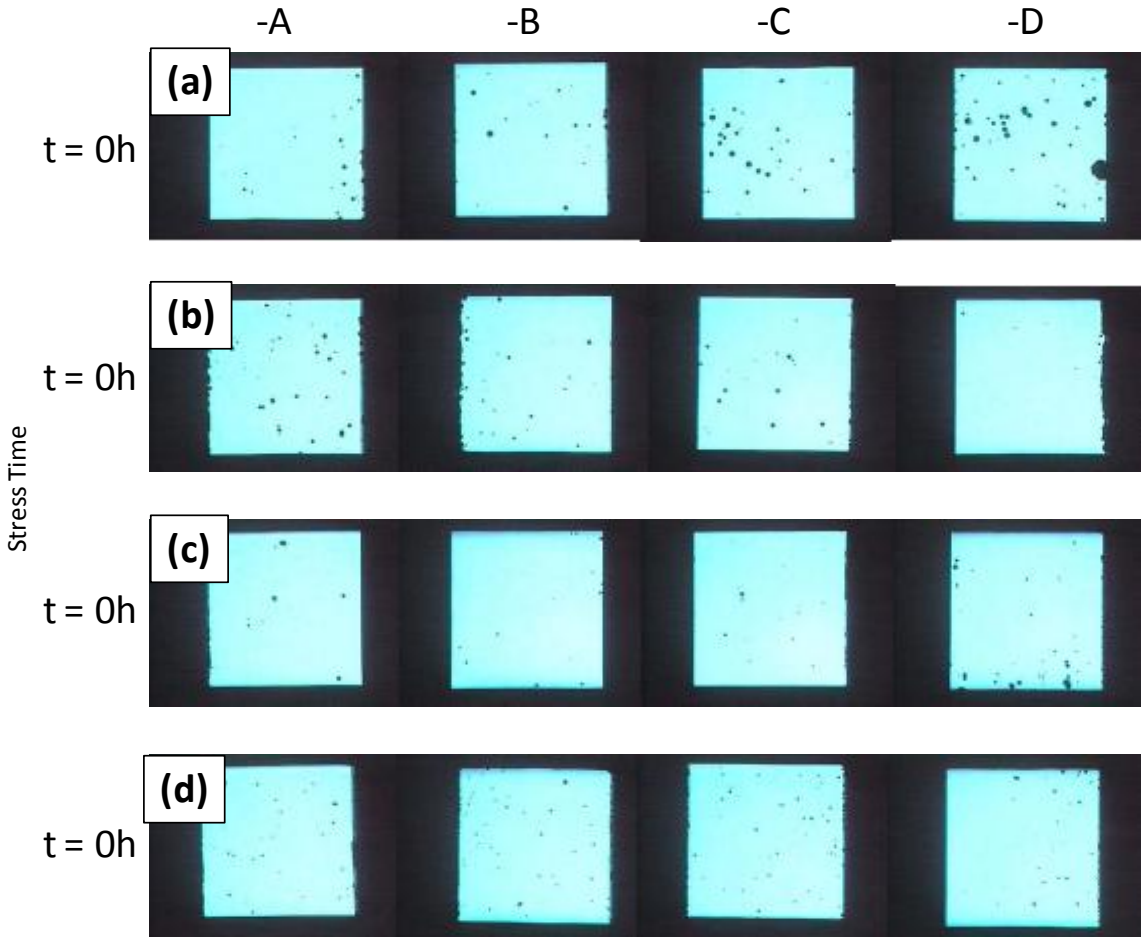

Figure 6-27: OLED sample set EM06 at time = 0h. No device lasted long enough for a second image. (a) EM06-1; (b) EM06-2; (c) EM06-3; (d) EM06-4.

The necessity for tensile films to cancel out the compressive stress is clearly evident by the premature failure of these devices. The incorporation of carbon films in to the TFES, despite the poor performance of devices encapsulated at Georgia Tech, is still a goal. However, before tensile carbon films using the 50 mTorr recipe described above could

be utilized, new facilities at the University of Michigan obviated the need to travel to the Georgia Tech cleanroom.

Film Development in New Deposition Tool

The availability of a new PECVD tool (Plasmatherm 790) at the University of Michigan allows for the deposition of oxide, nitride and amorphous carbon within the same chamber. Similar to the GSI, the Plasmatherm is a capacitively coupled device. The main difference is the ability of this tool to maintain lower deposition pressures and lower gas flow rates. With less mass within the chamber during deposition, it is expected that the Plasmatherm can deposit at lower deposition rates and with less particulate contamination. Lower deposition rates are desirable because they afford longer surface diffusion times for adsorbed reactive species. This, in turn, promotes a more dense film as diffusing species have time to fill in microvoids and surface irregularities.

The oxide, nitride and carbon processes developed for the GSI and Astex tools were adapted to the Plasmatherm. For the oxide deposition, there was, again, little trouble finding a recipe which produced adequate films at low temperature and, again, little hope of making tensile films.

Again, the low temperature deposition process impeded the development of tensile nitride films. Figure 6-28 shows the dependence of film stress on chamber pressure. There is a tendency for films to become less compressively stressed at higher pressures. This trend could not be followed to higher pressures (and hopefully tensile films) as the higher pressures lead to unacceptable levels of particulate contamination. At the other

end of the pressure range, stress measurement for low pressure depositions became impossible as the film uniformity decreased to unacceptable levels below 200 mTorr (stress calculated from measuring the strained wafer's radius require uniform film coverage).

Alternatively plotted, Figure 6-29 shows a clear relationship between residual stress and deposition power. The films become less compressively stress, bordering on tensile, as the deposition RF power is decreased. This is most likely due to low power processes favoring the formation of tri- and tetra-amino silane precursors over the direct reaction of silicon and nitrogen. Tensile nitride films can be produced when NH3 groups are eliminated from the film as tri- and tetra-amino silane groups react. Thus, the more tensile films suggest that molecular nitrogen plays a lesser role in low power depositions. As such, the effective N:Si ratio decreases at lower power, altering the quality of the produced films and setting a lower limit on power.

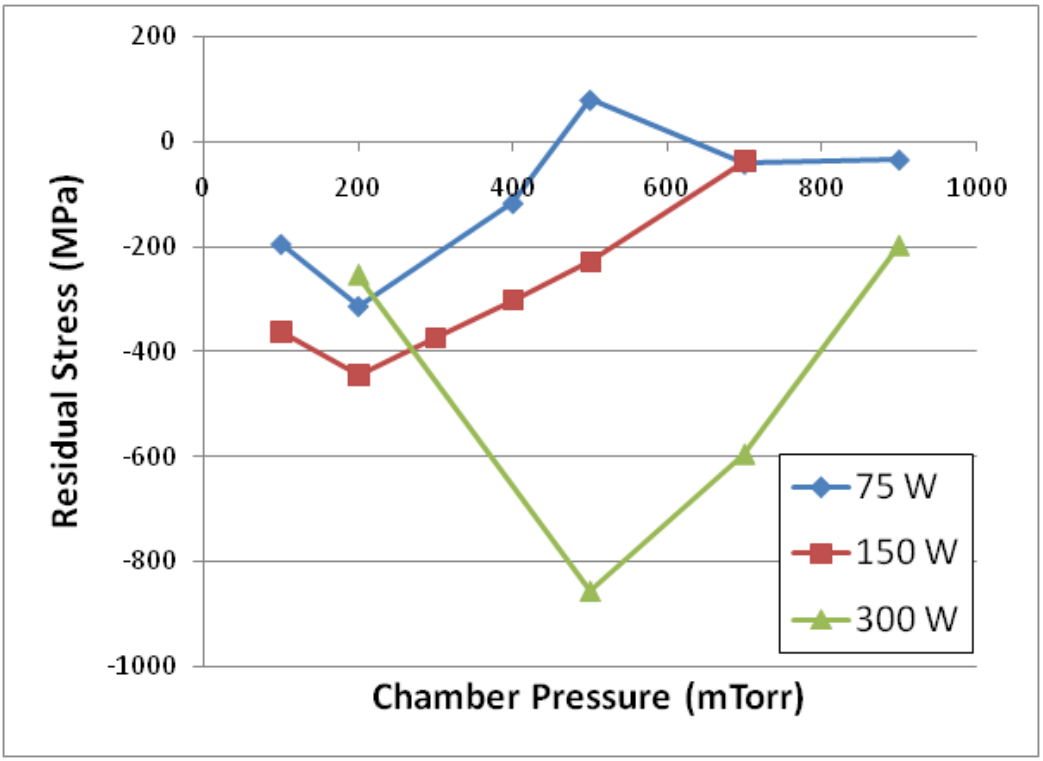

Figure 6-28:Residual stress vs. chamber pressure for silicon nitride films grown in the Plasmatherm PECVD tool

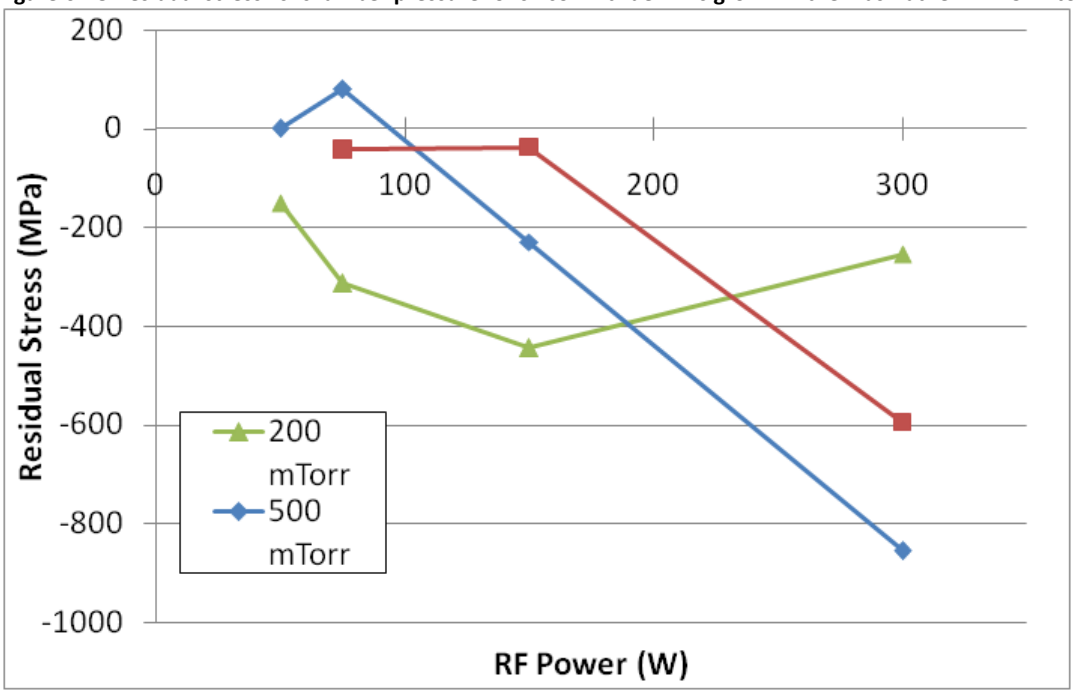

Figure 6-29: Residual stress vs. RF power for silicon nitride films grown in the PLasmatherm PECVD tool

As a result of the compressive nature of these films, films produced in the Plasmatherm are subject to the same failure mechanism as seen in films deposited in the GSI and

Astex tools. Figure 6-30 shows an SEM image (15KV) of a 1000Å film of silicon nitride deposited in the Plasmatherm on a silicon substrate. The image reveals the effect of residual compressive stress on the quality of the film as there is clear evidence of both spalling and buckling. Large (~100µm) holes appear in the film left behind by ejected segments of the film (a). The ejected material has collected on the film surface, adding to the particulate contamination (b). In addition, there are regions of the film which show evidence of buckling (c). This image also reveals the effect that this failure mechanism has on the efficacy of barrier made with compressive films, as it is clear that the large, gaping holes will not provide an effective barrier against diffusion.

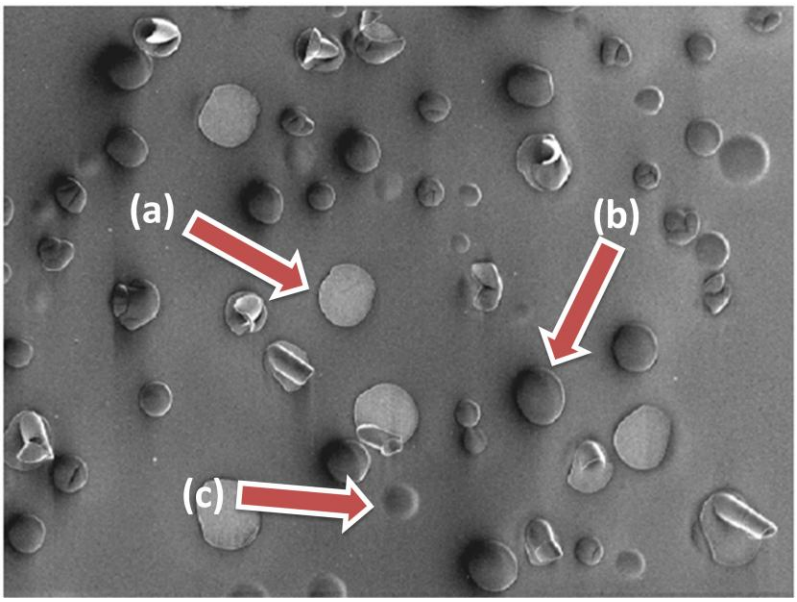

Figure 6-30: Stress failure of compressed silicon nitride films showing the hole left from spalling (a), the ejected material remaining on the surface of the film (b), and buckling of the film (c).

The index of refraction for nitride films remains relatively constant near 1.8 for most deposition conditions, as shown in Figure 6-31. The invariance of the index of refraction over the range of RF power and chamber pressure suggests that index of refraction is dependent mainly on deposition temperature. This suggests that lower density for

silicon nitride films deposited in the Plasmatherm is the effect of porosity resulting from retarded surface diffusion.

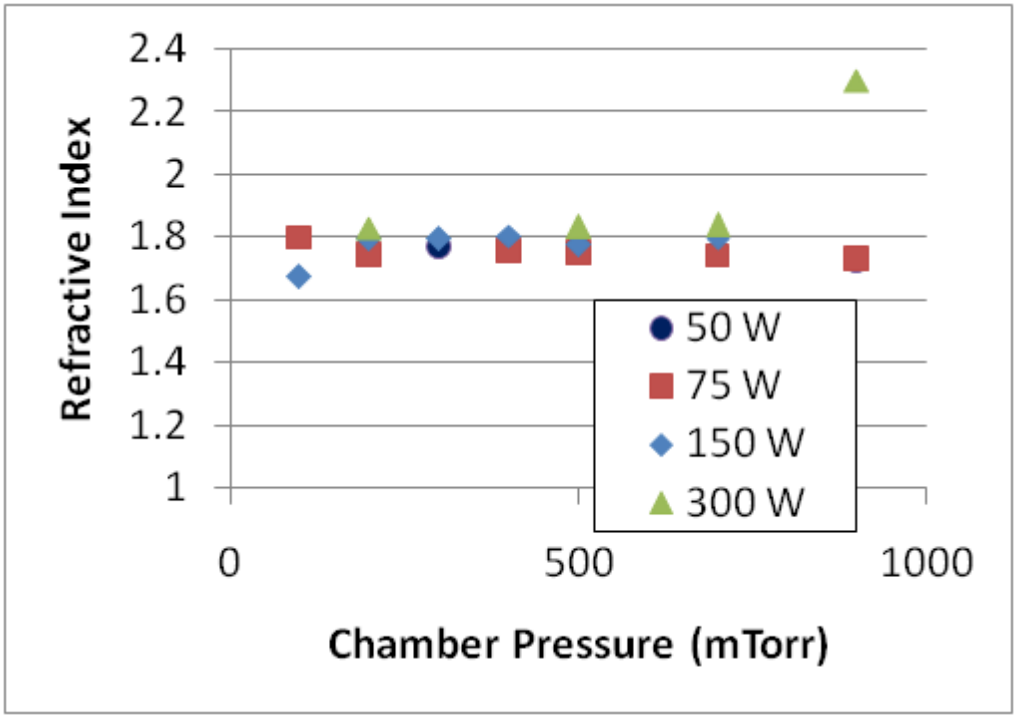

Figure 6-31: Refractive index vs. chamber pressure for silicon nitride films grown in the Plasmatherm PECVD tool

OLED Encapsulation with New Deposition Tool

OLEDs using F8BT were fabricated in the manner described in Chapter 4. Three samples were made: one with no encapsulation, one with a single 2.5µm film of parylene and the final with an encapsulation stack of 2.5 µm parylene/3 bilayers of {1000Å nitride/1000Å oxide} with the inorganic layers deposited in the Plasmatherm PECVD. The lifetimes of the devices were measured at 10V in ambient air (25°C/ 45% rel. humid.) via the method described in Chapter 4. The effective emission area ($(Area_{OLED} - Area_{Dark\ Regions})/Area_{OLED}$) is plotted in Figure 6-32. Images of the devices at approximately 80% emission are shown to the right. It is clear that the use of encapsulation slows the growth of dark spot formation. The use of parylene alone

increases the lifetime (defined in this context as the time required for the effective area to decay to 80%) by a factor of ~15. Employing parylene plus three bilayers of inorganic nitride and oxide results in an increase of three orders of magnitude over the unencapsulated device. In these trials, stress-induced buckling was not observed. This is due to the samples not being placed in an 85°C/85% testing chamber, since stressed samples exposed to excessive heat and moisture will be subject to moisture-induced stress effects, leading to buckling and cracking at an accelerated rate.

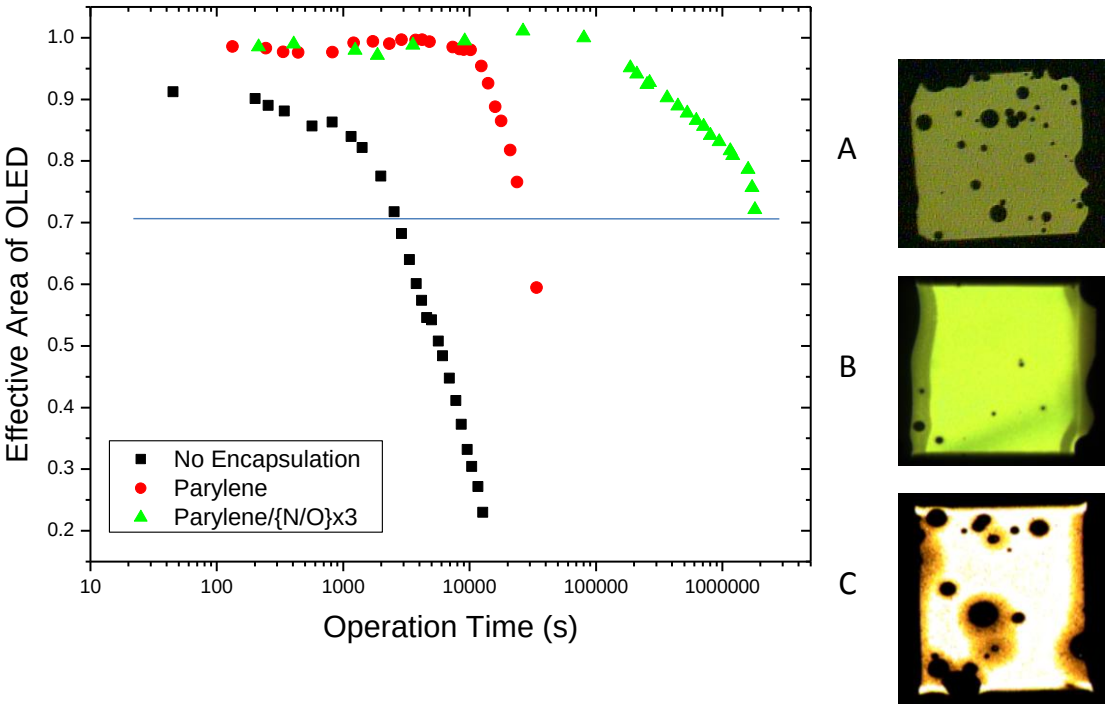

Figure 6-32: Left: Effective area of F8BT-based OLEDs with various encapsulation schemes as a function of operation time. The blue line represents 80% effective area. Right: Images of OLEDs at 80% effective area, A = No encapsulation, B = Parylene, C = Parylene/{N/O}x3

The plots show two regions of decay: a slow, almost stable region followed by a period of more rapid decay abruptly after a given time. This may be due to the slow diffusion rate of atmospheric oxidants through the encapsulation films. During this time period,

the reactive interface between is effectively protected from chemical degradation and mechanical failure.

Zero-Stress Trilayer Stack

Figure 6-33 shows the stress evolution of a tri-layer of 1000Å nitride, 1000Å oxide and 1050Å amorphous carbon on silicon. Both the nitride and oxide layers were compressively stressed after deposition, leading to a total residual stress of -81.0 MPa (compressive). Tensile films of amorphous carbon were then deposited on the nitride/oxide bi-layer in 150Å increments. Stress measurements were made between each deposition. The red line, indicating the change in total film residual stress, shows a large positive change in stress resulting from the first two carbon films. This may be due to surface realignment leading to the relief of built-up surface tension at the oxide/carbon interface. As the carbon film grows, the bulk properties of the film begin to dominate and the stress evolution adopts a linear increase until the original compressive stress of the nitride/oxide bilayer is completely compensated by the tensile carbon film.

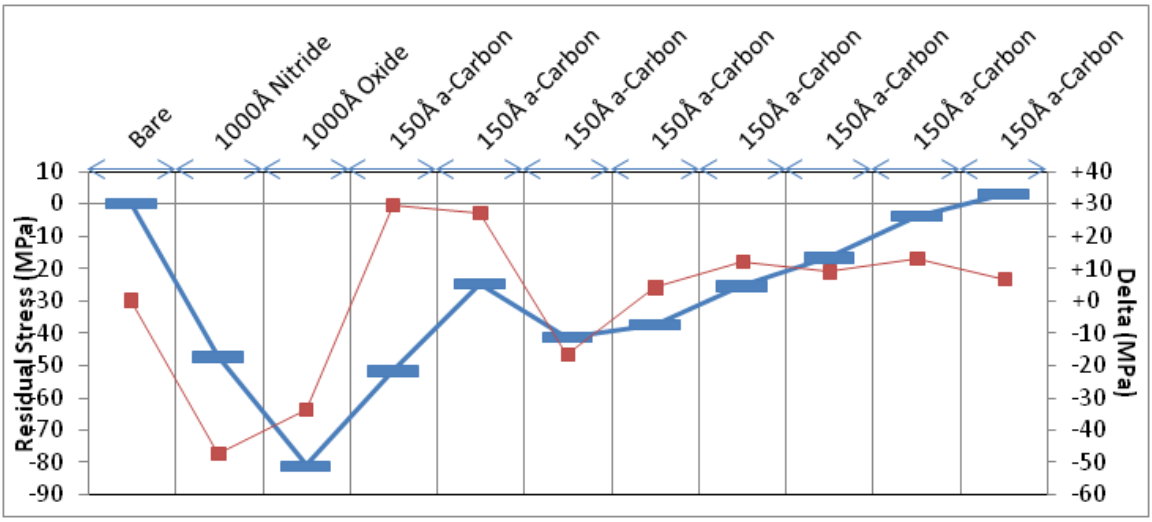

Figure 6-33: Evolution of residual stress for tri-layer stack of 1000Å Nitride/1000Å Oxide/1050Å a-Carbon (Blue line) and the change in film stress from layer to layer (red line).

Conclusions and Future Work

The difficulty of producing stress-free conformal films in a low-temperature, particulate-free deposition process is evident by the results presented here. Even in the best cases, particulate contamination was a significant problem which led to premature failure of OLED devices when tested in the harsh conditions of an 85°C/85% testing chamber. To be certain, some of the problem lies in the fact that the deposition tools used were not dedicated devices, whose chamber conditions are known and tightly regulated. As a result of their multi-use designation, cleaning routines which proved effective at one point in the test runs was found to be unreliable when chamber conditions change.

This is especially challenging for low temperature processes which tend to promote both particulate formation (by increasing the rate of energy-reducing aggregate formation) and higher compressive film stresses (due to mismatches in thermal coefficient of expansions between the substrate and encapsulant film). These difficulties are not,

however, unconquerable. Dark spot growth rates shown in Figure 6-32 show that encapsulation is effective in preventing the mechanical failure of OLED cathodes even if those encapsulation films suffer from the same defects as those shown in the Alq3-based samples (OLED samples EM01 – EM06). The harsh testing conditions of higher temperature and humidity expose the films' weaknesses. This gives hope to the endeavor insofar as the gap between the results presented here and the desired performance of encapsulation schemes is a matter of protocol and deposition conditions, but not of any fundamental error in conception.

Future work should examine the conditions which prevent the deposition of tensile or zero-stress oxide and nitride films as well as explore the production of particulate contamination. This may require equipment dedicated to the task of thin film encapsulation and (if this tool is plasma-based) able to generate sufficiently dense and energetic plasma, so to mitigate the problems exacerbated by the low-temperature requirement.

In addition, the zero-stress trilayer stack should be applied to OLEDs and stressed in an 85°C/85% testing chamber. It is expected that conformal films with zero stress should extend the usable lifetime of OLED samples and decrease the growth rate of dark spots.

Bibliography

[1] Ke, L., Lim, S. F., Chua, S. J., Organic light-emitting device dark spot growth behavior analysis by diffusion reaction theory. J. of Poly. Sci. B, Vol. 39, p. 1697, (2001)

[2] Hung, L. S., Chen, C. H., Recent progress of molecular organic electroluminescent materials and devices. Mat. Sci. Eng., R, Vol. 39, p. 143, (2002)

[3] McElvain, J., Antoniadis, H., Hueschen, M. R., Miller, J. N., Roitman, D. M., Sheats, J. R., Moon, R. L., Formation and growth of black spots in organic light-emitting diodes. , Vol. 80, , (1996)

[4] Laubender, J., Chkoda, L., Sokolowski, M., Umbach, E., The influence of oxygen and air on the characteristics of organic light-emitting devices studied by in vacuo measurements. Synth. Met., Vols. 111-112, p. 373, (2000)

[5] Ichikawa, M., Naitou, R., Koyama, T., Taniguchi, Y., Exciton Dynamics in Organic Semiconductor Devices: Investigation of Exciton-Charge Carrier Interactions as Revealed by Photoluminescence Responses. Jpn. J. Appl. Phys., Vol. 40, p. L1068, (2001)

[6] Bliznyuk, V. N., Carter, S. A., Scott, J. C., Klarner, G., Miller, R. D., Miller, D. C., Electrical and Photoinduced Degradation fo Polyfluorene Based Films and Light-Emitting Devices. , Vol. 32, , (1999)

[7] Gong, X., Parameswar, K. I., Moses, D., Bazan, G. C., Heeger, A. J., Xiao, S. S., Stabilized Blue Emission from Polyfluorene-Based Light-Emitting Diodes: Elimination of Fluorenon Defects. , Vol. 13, , (2003)

[8] Aziz, H., Popovic, Z., Xie, S., Hor, A.-M., Hu, N.-X., Tripp, C., Xu, G., Humidity-induced crystallization of tris (8-hydroxyquinoline) aluminum layers in organic light-emitting devices. Appl. Phys. Lett., Vol. 72, p. 756, (1998)

[9] Aziz, H., Popovic, Z., Tripp, C. P., Hu, N.-X., Hor, A.-M., Xu, G., Degradation processes at the cathode/organic interface in organic light emitting devices with Mg:Ag cathodes. , Vol. 72, pp. 2642-2644, (1998)

[10] Kolosov, D., English, D. S., Bulovic, V., Barbara, P. F., Forrest, S. R., Thompson, M. E., Direct observaction of structural changes in organic light emitting devices during degradation. , Vol. 90, , (2001)

[11] Nissen, D. A., The low-temperature oxidation of calcium by water vapor. Oxidation of Metals, Vol. 11, p. 241, (1977)

[12] Lewis, S. L., Weaver, M. S., Thin-Film Permeation-Barrier Technology for Flexible Organic Light-Emitting Devices. IEEE Journal of Selected Topics in Quantum Electronics, Vol. 10, pp. 45-57, (2004)

[13] Ghosh, A. P., Gerenser, L. J., Jarman, C. M., Fornalik, J. E., Thin-film encapsulation of organic light-emitting devices. , Vol. 86, , (2005)

[14] Burrows, P. E., Graff, G. L., Gross, M. E., Martin, P. M., Hall, M., Mast, E., Bonham, C., Bennett, W., Michalski, L., Weaver, M., Brown, J. J., Fogarty, D., Sapochak, L. S., Gas permeation and lifetime tests on polymer-based barrier coatings. , Vol. 4105, , (2001)

[15] Lim, S. F., Ke, L., Wang, W., Chua, S. J., Correlation between dark spot growth and pinhole size in organic light-emitting diodes. Appl. Phys. Lett., Vol. 78, p. 2116, (2001)
[16] Niu, Y.-H., Hou, Q., Cao, Y., Thermal annealing below the glass transition temperature: A general way to increase performance of light-emitting diodes based on copolyfluorenes. Applied Physics Letters, Vol. 81, pp. 634-636, (2002)
[17] Teetsov, J., Fox, M. A., Photophysical characterization of dilute solutions and ordered thin films of alkyl-substituted polyfluorenes. Journal of Materials Chemistry, Vol. 9, pp. 2117-2122, (1999)
[18] Caria, S., Como, E. Da, Murgia, M., Zamoni, R., Melpignano, P., Biondo, V., Enhanced light emission efficiency and current stability by morphology control and thermal annealing of organic light emitting diode devices. Journal of Physics: Condensed Matter, Vol. 18, pp. S2139-S2147, (2006)
[19] Rosink, J. J. W. M., Lifka, H., Reitjens, G. H., Pierik, A., Ultra-thin Encapsulation for large-area OLED displays. , , , (2005)
[20] Plummer, J. D., Deal, M. D., Griffin, P. B., Silicon VLSI Technology: Fundamentals, Practice and Modeling. Upper Saddle River : Prentice Hall, 2000.
[21] Nakayama, S., ECR (electron cyclotron resonance) plasma for thin film technology. Pure & Appl. Chem., Vol. 62, p. 1751, (1990)
[22] Robertson, J., Diamond-like amorphous carbon. Materials Science and Engineering R, Vol. 37, pp. 129-281, (2002)
[23] Lanford, W. A., Rand, M. J., The hydrogen contentn of plasma-deposited silicon nitride. , Vol. 49, , (1978)
[24] van Assche, F. J. H., Vangheluwe, R. T., Maes, J. W. C., Mischke, W. S., Bijker, M. D., Dings, F. C., Evers, M. F. J., Kessels, W. M. M., van de Sanden, M. C. M., A Thin film encapsulation stack for PLED and OLED displays. , Vol. 35, , (2004)
[25] Savaloni, H., Shahrestani, S. A., Player, M. A., Influence of deposition rate and time on nucleation of Er on a-C. Nanotechnology, Vol. 8, p. 172, (1997)
[26] Liao, W. S., Lin, C. H., Lee, S. C., Oxidation of silicon nitride prepared by plasma-enhanced chemical vapor deposition at low temperature. Applied Physics Letters, Vol. 65, pp. 2229-2231, (1994)
[27] Besser, R. S., Louris, P. J., Musket, R. G., Chemical Etch Rate of Plasma-Enhanced Chemical Vapor Deposited SiO2 Films. Journal of the Electrochemical Society, Vol. 144, pp. 2859-2864, (1997)
[28] Soh, M. T. K., Savvides, N., Misca, C. A., Dell, J. M., Faraone, L., Chemical structure of low-temperature plasma-deposited silicon nitride thin films. Proceedings of the SPIE, Vol. 5276, pp. 434-441, ()
[29] Monteiro, O. R., Wang, Z., Brown, I. G., Chemical Vapour Deposition of Silicon Nitride in a Microwave Plasma Assisted Reactor. J. Mater. Sci., Vol. 31, p. 6029, (1996)
[30] Allaert, K., Calster, A. van, Loos, H., Lequesue, A., A comparison between silicone nitride films made by PCVD of N2±SiH4/Ar and N2±SiH4/He. , Vol. 132, , (1985)
[31] Mort, J., Jansen, F., , [ed.] Plasma Deposited Thin Films. Boca Raton : CRC Press, 1986.

[32] Donovan, R. P., Yamamoto, T., Periasamy, R., Clayton, A. C., Mechanisms of Paricle Transport in Process Equipment. Journal of the Electrochemical Society, Vol. 140, pp. 2917-2922, (193)
[33] Collins, S. M., Brown, D. A., O'Hanlon, J. F., Carlile, R. N., Postplasma particle dynamics in a Gaseous Electronics Conference RF Reference Cell. Journal of Vacuum Science and Technology A, Vol. 13, pp. 2950-2953, (1995)
[34] Bauccio, Michael, , [ed.] ASM Engineered Materials Reference Book. 2nd. Materials Park : ASM International, 1994.
[35] Winchester, K., Spaargaren, S.M.R., Dell, J.M., Tunable Fabry-Perot Cavities. [ed.] Ash M. Parameswaran, Francis E. H. Tay Kevin Chau, . 2000. Proceedings of SPIE. Vol. 4230, pp. 198-209.
[36] Sunami, H., Itoh, Y., Sato, K., Stress and Thermal-Expansion Coefficient of Chemical-Vapor-Deposited Glass Films. Journal of Applied Physics, Vol. 41, pp. 5115-5117, (1970)
[37] Smith, D., Controlling the plasma chemistry of silicon nitride and oxide deposition from silane. J. Vac. Sci. Technol., Vol. A11, p. 1843, (1993)
[38] Smith, D. L., —. Journal of vacuum science and technology A, Vol. 11, pp. 1843-1850, (1993)
[39] Knight, T. J., Greve, D. W., Cheng, X., Krogh, B. H., Real-time Multivariable Control of PECVD Silicon Nitride Film Properties. IEEE TRANSACTIONS ON SEMICONDUCTOR MANUFACTURING, Vol. 10, pp. 137-146, (1997)
[40] Smith, D. L., Alimonda, A. S., Preissig, F. J. von, Journal of Vacuum Science and Technology B, Vol. 8, p. 551, (1990)
[41] Mackel, H, Ludemann, R., Detailed study of the composition of hydrogenated SiNx layers for high-quality silicon surface passivation. Journal of Applied Physics, Vol. 92, pp. 2602-2609, (2002)
[42] Chupka, W. A., Berkowitz, J., Photoionization of Methane: Ionization Potential and Proton Affinity of CH4. The Journal of Chemical Physics, Vol. 54, pp. 4256-4259 , (1971)
[43] Field, J. E., Properties of Diamond. London : Academic Press, 1993.
[44] Lifshitz, Y., Hydrogen-free amorphous carbon films: correlation between growth conditions and properties. Diamond and Related Materials, Vol. 5, pp. 388-400, (1996)
[45] Michalske, T. A., Freiman, S. W., A molecular mechanism for stress corrosion in vitreous silica. , Vol. 66, , (1983)
[46] Michalske, T. A., Bunker, B. C., , Vol. 56, , (1984)
[47] Ulrich, R. K., Brown, W. D., Ang, S. S., Yi, S., Sweet, J., Peterson, M. D., PECVD silicon nitride postbond films for protecting bondpads, bonds and bondwire from corrosion failure. , Vols. 0569-5503, , (1991)
[48] Dyrbye, K., romedahl-Brown, T., Eriksen, G. F., Packaging of physical sensors for aggressive media application. , Vol. 6, , (1996)
[49] Mukhopadhyay, S., Jana, T., Raya, S., Development of low temperature silicon oxide thin films by photo-CVD. , Vol. 23, pp. 417-422, (2005)

[50] Lan, W. H., Tu, S. L., Yang, S. J., Huang, K. F., Infrared Spectroscopic study of Mercury-sensitized photo-CVD silicon oxide. , Vol. 29, pp. 997-1003, (1990)
[51] Lin, X., Fonash, S. J., Low temperature silicon dioxide thin films deposited using tetramethylsilane for stress control and coverage applications. , Vol. 695, , (2002)
[52] RodrIguez, J. A., Dominguez, C., Munoz, F. J., Liobera, A., Mechanical properties of PECVD silicon oxide films suitable for integrated optics applications. , Vol. 3953, pp. 142-149, (2000)
[53] Ghosh, A. P., Full-color OLED on silicon microdisplay. s.l. : Proceedings of the SPIE, 2002. Organic Light-Emitting Materials and Devices V. Vol. 4464, p. 1.
[54] Matuda, N., Baba, S., Kinbara, A., Internal stress, Young's Modulus and adhesion energy of carbon films on glass substrates. , Vol. 81, , (1981)
[55] Evans, A. G., Hutchinson, J. W., On the mechanics of delamination and spalling in compressed fimls. , Vol. 20, , (1984)
[56] Moon, M.-W., Chung, J.-W., Lee, K.-R., Oh, K. H., Wang, R., Evans, A. G., An experimental study of the influence of imperfactions on the buckling of compressed thin films. , Vol. 50, , (2002)
[57] Keterrier, Y., Durability of nanosized oxygen-barrier coatings on polymers. Progress in Materials Science, Vol. 48, pp. 1-55, (2003)
[58] Lueder, E., Passive and active matrix liquid crystal displays with plastic susbstrates. Electrochemical Society Proceedings, Vols. 98-22, pp. 336-354, (1998)
[59] Modern Plastics Encyclopedia. New York : McGraw Hill, 1968. Vol. 45/No. 1A.
[60] Lacari, J. J., Brands, E. R., Machine Design, , p. 192, (May 1967)
[61] Sullivan, J. P., Friedmann, T. A., Baca, A. G., Stress relaxation and thermal evolution of film properties in amorphous carbon. Journal of electronic Materials, Vol. 26, pp. 1021-1029, (1997)

Chapter 7
Dark Spot Growth Rate of Pulsed OLEDs

Introduction

To date, the most commonly used driving method for OLEDs has been DC – either current-controlled or voltage controlled. AC or pulsed driving of OLEDs is of increasing interest for display and solid state applications (1). Baigent et. al. showed that DC pulsing of OLEDs is a plausible means of sourcing OLEDs for commercial applications (2). They demonstrated in two-layer polymer OLEDs turn-on times of 3μs and that this time is dependent on the transit time of injected charge carriers. In AC and pulsed operation, it is expected that device degradation will be mitigated.

Pulsed driving affects a number of the deleterious factors which limit OLED lifetime. First, a pulsed driving method can mitigate the thermal degradation caused by high current densities (3). Joule heating, which results from current passing through a resistive material, facilitates a number of thermal degradation modes including degradation of organic materials with low glass transition temperatures (such as commonly used hole transporting materials) and accelerated oxygen and moisture diffusion and reaction. Second, mobile ionic impurities do not migrate as much under

pulsed operation. Finally, excess hole injection is mitigated as the off-time in a pulse period allows for charges to diffuse away from the emission region.

Factors that affect device lifetime under pulsed driving conditions are known to be complex. For instance, Liu et. al observed a duty ratio dependence on the forming process, whereby mobile ions realign within the polymer bulk, lowering the resistance of the device, thereby increasing the current density (4). The increase in recombinant charge carrier in the polymer results in an initial increase in device luminance, rather than a steady decrease. They showed that a lower duty ratio increases the initial rise in luminance. As this effect is increased, though, the luminance decays faster as operation time increases, resulting in a lifetime similar to devices with higher duty ratios.

The forming effect notwithstanding, Tsujioka et. al. show that the lifetime of electroluminescent devices can be increased by driving the device with a low duty ratio and low mean current (5). In their experiment they maintained a constant luminance of 100 cd/m^2. A similar result was also reported by Li et. al. (6) Similarly, Cusumano et. al. found that the lifetime of a Alq3-based device is 4 times longer when driven with a 50% duty cycle at 1kHz as opposed to a constant voltage (7). Tsujioka et. al. attribute the extended lifetime of these devices to a lower field-induced orientation of the emissive molecules (8).

Luo et. al. note, however, that this explanation cannot account for the observation that for low duty cycles (<10%) with high current density often show diminished lifetimes (9). They show that device stability depends on the relative EL efficiency in that higher efficiency leads to longer device lifetime. Thus, driving methods which require high

current densities to maintain a constant luminance (such as pulsed methods with small duty ratios) result in an excess of one type of charge carrier, which in turn leads to low EL efficiency and shorter device lifetime. Aziz et. al. were later able to demonstrate that a pulsed driving method which results in an Alq_3-based device decreasing in luminance by only 10% after 600 hours of operation (10).

The studies cited above measure the driving method's effect on the total luminance of OLED devices. The degradation observed in these devices originates from both internal degradation (factors which reduce the emission efficiency of the emissive material) and external degradation (factors which result from the operational environment). Among the latter sources, dark spot formation has been identified as a major contributor to the degradation of devices (11). To date, little research has been done on the effect of duty cycle on the growth of dark spots. This may be because there has been a strong effort to reduce dark spot formation by use of encapsulation techniques (12). However, as AC and pulsed driving becomes more commonplace in OLED applications, the necessity of investigating the effect of these driving methods on dark spot growth becomes clearer.

The most immediate effect of varying the duty cycle of a driving scheme is the loss of luminance with decreasing on-time. Figure 7-1 shows a clear decrease in luminance as the duty cycle is decreased for both a standard lamp (a) and an F8BT-based OLED (b).

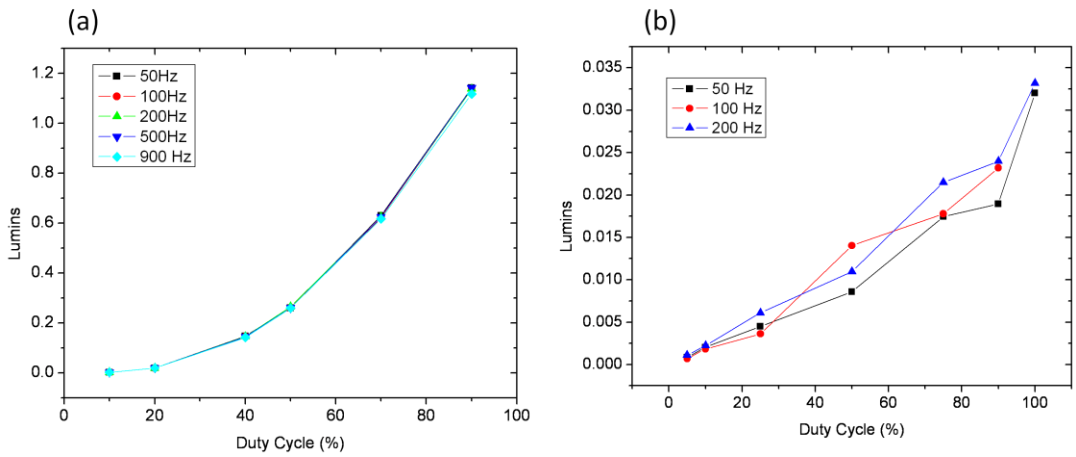

Figure 7-1: Emission vs. Duty cycle for (a) standard lamp and (b) F8BT-based OLED

Experimental

PLEDs were fabricated with F8BT emissive layers as described in Chapter 4. The devices were transferred to an environmentally controlled chamber in air and connected as shown in Figure 7-2. To source the PLED, an HP 8114a pulse generator was used. The deterioration of the OLED under bias necessitates the use of a buffered output from the pulse generator. Since the impedance of the OLED can vary from 5 to 65kΩ as the device deteriorates, the division of voltage between the output of the pulse generator and the OLED changes. To remedy this, a buffer amplifier with input impedance of 1k Ω was used. The buffer amp is an operational amplifier with unity gain. The advantage is that it has sufficiently low output impedance so that it acts as an ideal voltage source across the impedance range of the OLED. It was observed that the amplitude of the applied pulses changed by only ~0.1V during the lifetime of a typical device.

The waveform of the applied bias and OLED luminance are collected by an oscilloscope. An Allied Vision CCD camera, mounted on a microscope, records images of the emissive

area at regular intervals. The shutter length and gain are automatically adjusted to maintain consistent image brightness.

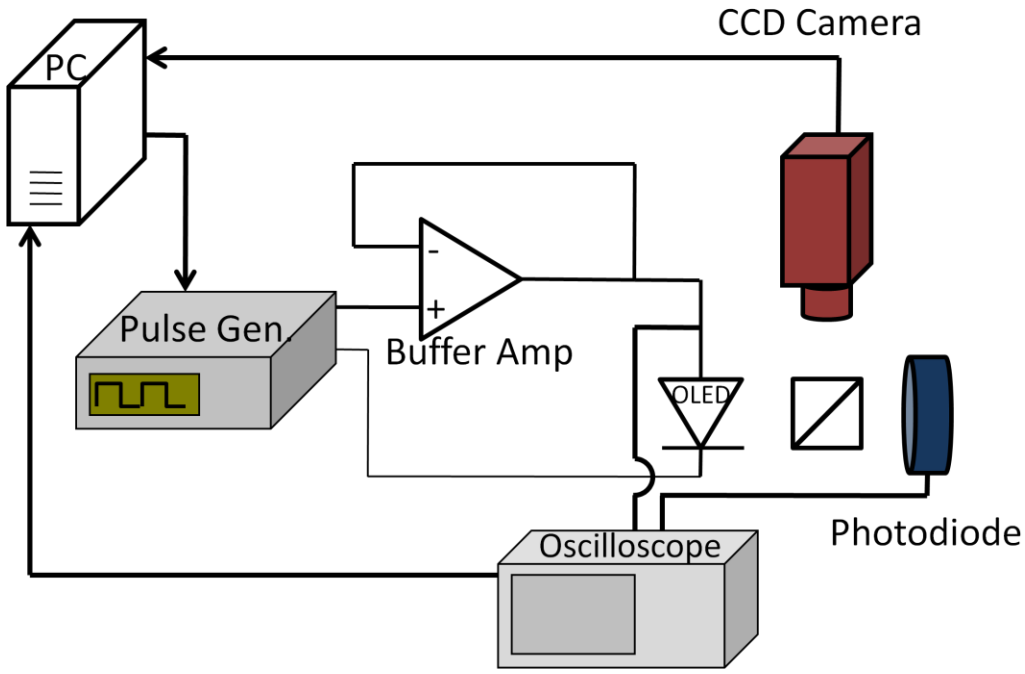

Figure 7-2: Instrumentation schematic for pulsed lifetime measurements

Relative humidity was kept between 21% and 23%for all measurements. The devices were sourced with 10V pulses with a period of 20ms. The duty cycle ranged from 5% to 75%. Images of the emissive regions of the OLEDs were processed as described in Chapter 4.

A pulse width of 20 ms (50Hz) was chosen because it avoids possible pitfalls when the source timebase is set too low or too high. The obvious effect of setting the pulse rate too low is an observable flicker which renders the device unsuitable for use as a light source. When the pulse rate is too high, aside from impedance concerns, which are not addressed here, the shortened pulse width can limit the luminance of the device as the diminished on time becomes less than the natural rise time of the OLED. Figure 7-3

shows the time-resolved luminance of an F8BT-based OLED pulsed at an amplitude of 10V at frequencies of 50, 100 and 200 Hz. The timescale of the plots have been normalized for easier comparison. The left graph shows the result of a 90% duty cycle while the right graph shows the result of a 5% duty cycle. The clearest indication of a limitation imposed by high frequency is seen in the 200Hz, 5% plot; wherein the device is not provided sufficient time to achieve full luminance. This and similar frequency effects can be mitigated by developing materials with faster rise and fall times, whose electroluminance is better able to follow the applied voltage signal.

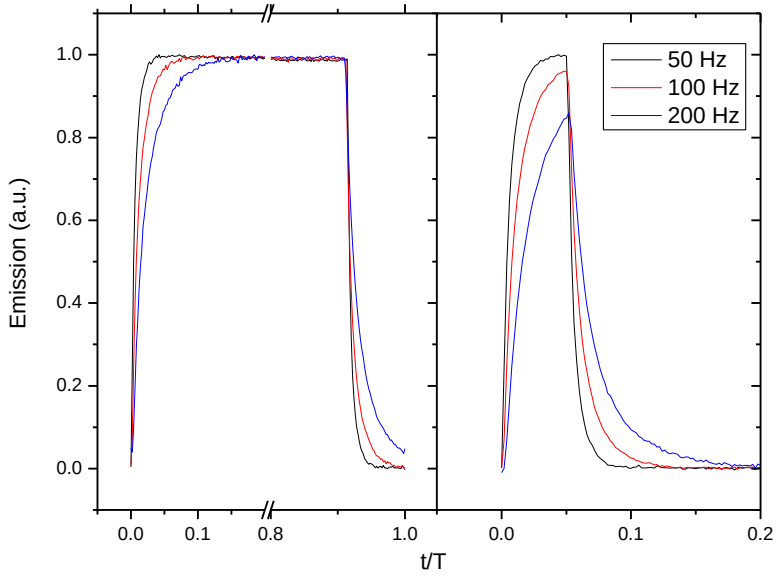

Figure 7-3: Time-resolved luminance of OLED for 50, 100 and 200 Hz. Left: 90% duty cycle. Right: 5% duty cycle. The timescale of the plots has been scaled so that the different frequencies can be compared.

Results and Discussion

Figure 7-4 shows the emissive area of F8BT-based OLEDs as a function of time. There is a clear dependence of dark spot growth rate on the driving pulse duty cycle. As the on-

time of the OLED is decreased, dark spot growth is inhibited. The inset of Figure 7-4 shows the time for the device to reach 50% of its original emissive area as a function of duty cycle.

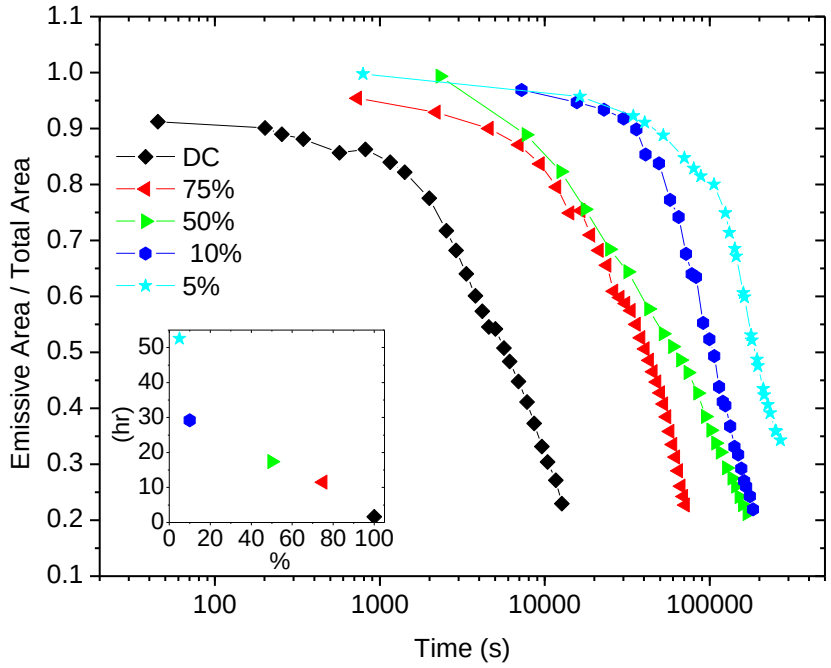

Figure 7-4: Emissive area of OLEDs driven by DC pulses with magnitude 10V, period 20ms and varying duty cycles.

This is in conflict with the results of McElvain et. al. (13) who found that the rate of growth of dark spots was a field-independent process. Their conclusion was based on the observation that after 40 hours of exposure to the same atmospheric conditions, the non-emissive areas of two devices, one stressed at 4.5V and one unstressed, were the same. The devices used in these trials were Alq3-based with Mg/Ag cathodes. These devices have a lower turn-on voltage and higher emission efficiency than that of devices made with F8BT. In the devices reported by McElvain, the initial current density at 4.5V

was 3-5 mA/cm^2. The low voltage and current requirements for such efficient devices is most likely the cause of the apparent insensitivity of dark spot growth the applied field. Such advantageous and admirable performance properties are not, however, an asset of F8BT devices. As Figure 7-5 shows, at 10VDC, an F8BT-based OLED initially draws about 50 mA/cm^2. Under constant voltage, this current density decreases as the device resistance increases linearly to almost 65 kΩ.

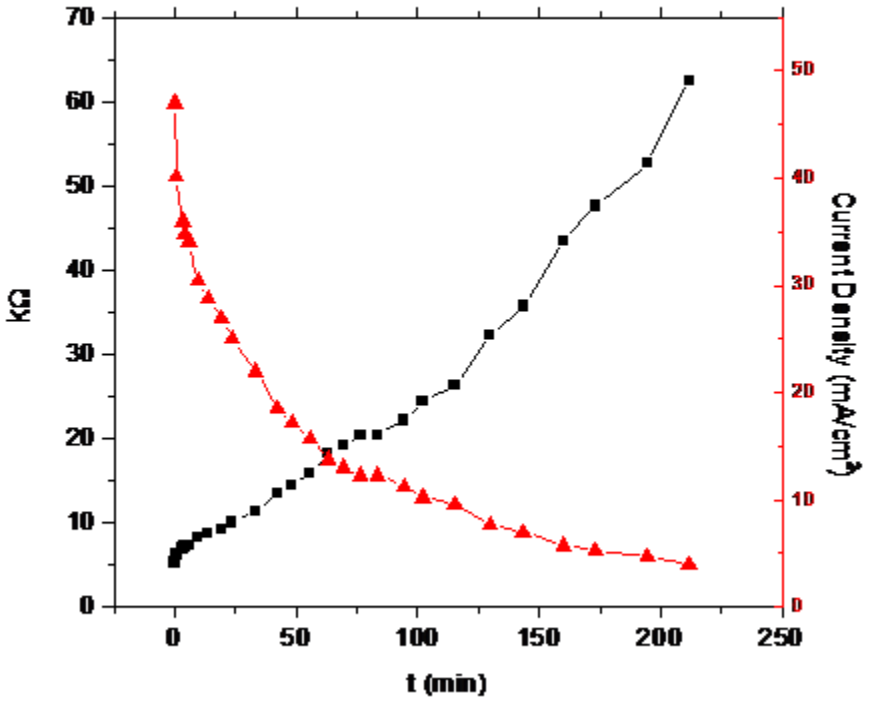

Figure 7-5: Electrical stability of F8BT-based OLED under 10VDC bias. Left axis shows device resistance, right axis shows current density.

The lower emission efficiency of polymer-based devices, as compared to Alq3-based devices, requires that a higher current density be provided to produce the same luminance as similar small-molecule devices. Thus, field-dependent growth of non-emissive regions is greatly pronounced in polymer-based devices, whereas the

observance of this dependence in Alq_3 devices may be swamped by this effect's dependence on atmospheric humidity.

Combination of Pulsed Driving Scheme and Thin Film Encapsulation

After observing the decrease in dark spot growth rate from the application of both thin film encapsulation and pulsed driving, the obvious next step is to combine the two in order to further protect the cathode from deterioration.

An F8BT-based OLED was fabricated using the typical method. The device was encapsulated with twelve layers of alternating a-H:SiN_x and a-H:SiO_x, each layer being 1000Å. The inorganic layers were deposited by PECVD using the best recipes from Chapter 6. The final layer was a 2µm thick layer of Parylene. The encapsulated device was transferred to the lifetime measurement chamber and sourced with 10V at 50Hz with a 50% duty cycle. Figure 7-6 shows the results for this OLED after 700 hours. The fraction of the emissive area for an unencapsulated OLED driven at 10V, 50Hz and 50% duty cycle as well as a 10VDC-diven OLED encapsulated with 2.5µm of parylene followed by twelve layers of alternating 1000Å, PECVD-deposited a-H:SiNx and a-H:SiOx are also plotted for comparison.

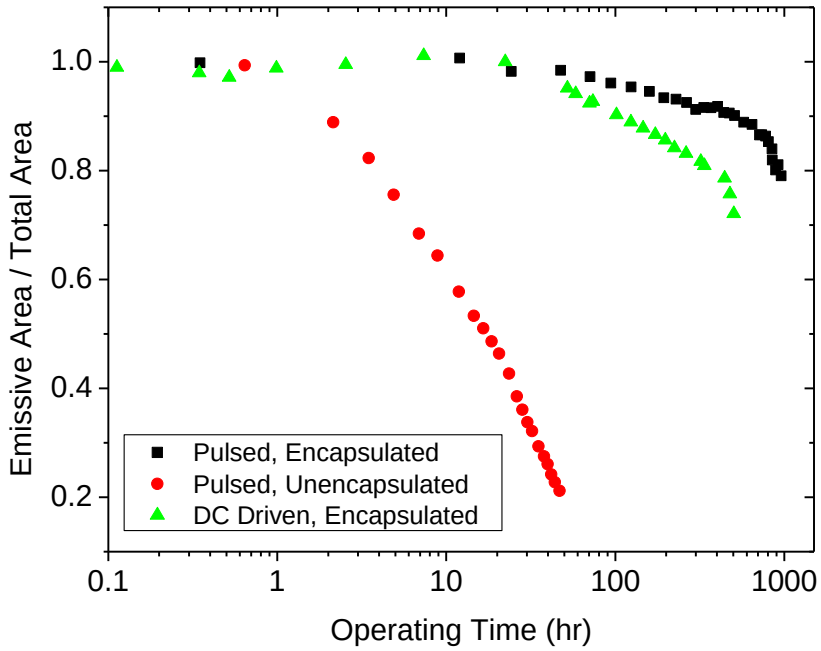

Figure 7-6: Fraction of emissive area vs. operating time in voltage for an OLED encapsulated with 2.5µm of parylene followed by twelve layers of alternating 1000Å, PECVD-deposited a-H:SiNx and a-H:SiOx and driven with 10VDC (green triangles), an OLED unencapsulated and driven with 10V pulses at 50Hz and 50% duty cycle (red circles) and an OLED encapsulated with twelve layers of alternating 1000Å, PECVD-deposited a-H:SiNx and a-H:SiOx and driven with 10V pulses at 50Hz and 50% duty cycle (black squares).

After 1000 hours, the effective area of the pulsed, encapsulated device has decreased to only 79% of the original emissive area. The DC-driven, encapsulated device reached this point after only 350 hours while the pulsed, unencapsulated device took only five hours to reach 80% area. Clearly, the combination of encapsulation and a pulsed driving scheme is an effective means of slowing the growth of non-emissive regions in OLEDs.

Conclusions and Future Work

As evidenced by the disparity between these results and those of McElvain et. al., the role of current density on the oxidation of reactive cathode metals is an important one. The instrumentation described above does not have the capacity to measure sourced

current, as the addition of a resistive element in series with the unstable OLED would lead to uncertainties as the device resistance changes, altering the division of voltage. Replacing the pulsed voltage source with a pulsed current source would allow for the proper control of charge carriers crossing the metal/organic interface. This would allow for a more complete description of the relationship between the electrochemical activity of the cathode with the overall OLED stability.

Bibliography

[1] Lin, Y.-C., Shieh, H.-P. D., Improvement of Brightness uniformity by AC driving scheme for AMOLED display. IEEE EDL, Vol. 25, p. 728, (2004)

[2] Baigent, D. R., May, P. G., Friend, R. H., Emissino characteristics of two-polymer layer electroluminescent devices operating under various duty cycles. Synth. Met., Vol. 76, p. 149, (1996)

[3] Zou, X., He, J., Liao, L. S., Lu, M., Ding, X. M., Hou, X. Y., Zang, X. M., He, X. Q., Lee, S. T., Real-Time Observation of Temperature Rise and Thermal Breakdown Processes in Organic LEDs Using an IR Imaging and Analysis System. Adv. Mater., Vol. 12, p. 265, (2000)

[4] Liu, X., Li, W., Yu, J., Peng, J., Zhao, Y., Sun, G., Zhao, X., Yu, Y., Zhong, G., Effect of Duty ratio of driving voltage on the forming process in aging of organic electroluminescenct devices. Jpn. J. Appl. Phys., Vol. 37, p. 6633, (1998)

[5] Tsujioka, T., Fujii, H., Hamada, Y., Takahashi, H., Driving duty ratio dependence of lifetime of tris(8-hydroxy-quinolinate)aluminum-based organic light-emitting diodes. Jpn. J. Appl. Phys, Vol. 40, p. 2523, (2001)

[6] Li, F., Feng, J., Liu, S., Degradatino of organic light-emitting devices under different driving model. Synth. Met., Vol. 137, p. 1103, (2003)

[7] Cusumano, P., Buttitta, F., Di Cristofalo, A., Cali, C., Effect of driving method on the degradation of organic light emitting diodes. Synth. Met., Vol. 139, p. 657, (2003)

[8] Tsujioka, T., Hamada, Y., Takahashi, H., Operating Current Mode Dependence of Luminescence Properties of Rubrene-doped Yellow Organic Light Emitting Diodes. Jpn. J. Appl. Phys. Part I, Vol. 39, p. 3463, (2000)

[9] Luo, Y., Aziz, H., Popovic, Z. D., Xu, G., Correlation between electroluminescence efficiency and stability in organic light-emitting devices under pulsed driving conditions. J. App. Phys., Vol. 99, p. 5408, (2006)

[10] Aziz, H., Luo, Y., Xu, G., Popovic, Z. D., Improving the stability of organic light-emitting devices by using a thin Mg anode buffer layer. Appl. Phys. Lett., Vol. 89, p. 103515, (2006)

[11] Hung, L. S., Chen, C. H., Recent progress of molecular organic electroluminescent materials and devices. Mat. Sci. Eng., R, Vol. 39, p. 143, (2002)

[12] Liu, Y., Aziz, H., Hu, N., Chan, H., Xu, G., Popovic, Z., Investigation of the sites of dark spots in organic light-emitting devices . Appl. Phys. Lett., Vol. 77, p. 2650, (2000)

[13] McElvain, J., Antoniadis, H., Hueschen, M. R., Miller, J. N., Roitman, D. M., Sheats, J. R., Moon, R. L., Formation and growth of black spots in organic light-emitting diodes. J. Appl. Phys., Vol. 80, , (1996)

Chapter 8
Conclusions and Future Work

White Light Generation and Förster Blends

While many color mixing techniques have been developed and explored, emissive blends utilizing Förster transfer remains one of the most studied and used means of generating white light. With the wide use of Förster blends, researchers have a greater need for methods which probe the mechanics of energy transfer and intermolecular interactions. Among the most important metrics in these systems is the efficiency of energy transfer. In the chapter detailing white emission from blends of polymers (Chapter 5), I have shown an effective means of characterizing the efficiency using spectroscopic methods. Using this method, I have shown that there is a compelling reason to employ Förster transfer as a means of color mixing as it shows a consistent 10-13% increase in efficiency over the trivial color mixing technique of placing two emitters in close proximity.

To be sure, some of the most efficient emission systems utilize a blend of a donor host polymer doped with small molecule acceptors. Never-the-less, a polymer-polymer donor-acceptor system is an effective vehicle for the development of this measurement procedure. The Förster efficiency procedure combines two techniques to arrive at a conclusive value for Förster transfer efficiency: an absolute photoluminescence

quantum efficiency method by spectroscopic measurement (detailed in Chapter 3) and a method of decomposing the blend spectra in to constituent Gaussian peaks in order to reconstruct the donor emission (detailed in Chapter 5).

In addition to the measurement procedure, Chapter 3 also discusses the systematic and measurement error incurred from a spectroscopic procedure. This error is carried through to the Förster efficiency measurement. As seen in Chapter 3, there is considerable error associated with any measurement which makes use of excitation light near or below 400nm. This is in part due to the low responsivity of the detection system at low wavelength and in part due to the low luminance of the calibration lamp in that spectral region.

Future Work: In order to minimize these measurement errors, prevent their propagation in to Förster efficiency measurements and ensure greater clarity and certainty in Förster efficiency, the tooling of the spectroscopic measurement system should be closely examined to ensure that the low wavelength spectral range is measured accurately and precisely. Certainly, a detector designed for the spectral range below 400nm is an appropriate addition to the tool. In addition, it may be necessary to amend the calibration procedure to include either an additional low wavelength step, or to make use of a calibration lamp with appreciable luminance in the spectral region of interest.

An additional source of error in Förster transfer efficiency measurements is the method of decomposition of the blend spectra in to constituent Gaussian peaks. This is done by iterative fitting routines built in to plotting and statistical software, such as OriginLab's

Origin 7.0. the quality of the fit is largely determined by the initial choices of peak position, number, width and height, which are inputted by the user. Clearly this is a source of error in the fitting as a capricious choice of initial parameters can change the details of the finial fitting. As of now, there is no systematic means of characterizing the error associated with this fitting step and, as such, error can not be traced to the final determination of Förster transfer efficiency.

Future Work: The error associated with the fitting of Gaussian peaks to blend spectra should be systematically characterized so to extend the uncertainty analysis through to the final stages of Förster transfer efficiency measurement.

It should also be noted, that the observed rise in efficiency in Förster blends over the trivial case of multiple emitters was done for the case photoluminescence. It is assumed that such a rise in efficiency will be observed in the case of electroluminescence, but no measurements of this nature were made. It is entirely possible envision analogous measurement procedure for Förster transfer efficiency which uses electroluminescent quantum efficiency and spectra in lieu of photoluminescent quantum efficiency and spectra. Unfortunately, the tooling which allows absolute photoluminescent quantum efficiency measurements is not sufficient to also measure electroluminescent quantum efficiency.

Future Work: Following the work described in Chhapter 3, an absolute electroluminescent quantum efficiency procedure using spectroscopic methods should be developed and the systematic error characterized. Since the technique for decomposing spectra in to constituent Gaussian peaks should be the same from

photoluminescent to electroluminescent spectra, this quantum efficiency method should be sufficient for extending the Förster transfer efficiency procedure to electrically stimulated thin films of blended polymers.

Packaging by Thin Film Encapsulation

As OLEDs move closer and closer to ubiquitous commercial devices, the urgency of effective encapsulation rises to a matter of upmost concern. Rapid degradation of organic devices by atmospheric oxidants can quickly quell consumer demand for organic lighting and displays. Thus, as OLEDs enter in to the commercial space, the issues and difficulties of encapsulation gain more attention from researchers.

The motivation for developing thin film encapsulation techniques, as opposed to rigid glass or metal cap methods, arises from the trend in OLED design of making thinner and lighter devices, as well as a desire for inexpensive, high quality material deposition. However, the results of my packaging work, detailed in Chapter 6, reveal that the technical obstacles for producing thin film encapsulation schemes which are commensurate with the organic devices are neither straightforward, nor close to being resolved.

Primary among the difficulties faced in these studies were particulate formation and residual compressive stress. In the former case, while it is conceivable that by an intelligent choice of deposition conditions, a particulate-free procedure may be found, I believe this is a highly unlikely scenario if the study is confined to the PECVD tools available at the University of Michigan during the time of this study. The PECVD tools suffer from two main issues. The first is that they are not dedicated tools. The

conditions of the deposition chamber are of critical importance to the quality of the films produced within them. In order to ensure consistent results without the possibility of unexpected chemical reaction which lead to particulate formation, the material deposited within the chamber must be limited to the encapsulant material only. This is simply not possible in a shared facility with hundreds of users requiring a wide array of deposited materials. Indeed, I believe that it is unwise for a research institution, such as the University of Michigan, to address the issue of particulate contamination in encapsulation fabrication, as this is very clearly a tool-determined process and is better left to industry researchers with a clear financial motivation for developing a clean deposition procedure, unique to their own deposition requirement.

The latter issue of residual compressive stress is, I believe, more suited to a research institution as the results and ideas are more easily generalizable. The results shown in Chapter 6 clearly show that low temperature deposition strongly favors compressively stressed amorphous silicon oxide and amorphous silicon nitride films. Environmental stress measurements at elevated temperature and humidity show that encapsulation suffering from high compressive residual stress will catastrophically fail, clearly an unacceptable result for commercial applications.

I employed a number of methods to, first, mitigate the stress (additional interfacial layers, low modulus organic films, etc.) and, then, to try and eliminate the stress altogether (zero-stress stacks of alternating layers). While I was able to show some success in extending the lifetime of compressively stressed encapsulation schemes, the superior solution would completely eliminate the residual stress. The results in Chapter

6 show that a zero-stress encapsulation stack is possible on a silicon substrate, but that applying such an encapsulation scheme to an actual OLED is rife with additional difficulties, the natures of which are, at present, unknown.

Future Work: Zero-stress encapsulation schemes for OLEDs are a critical step for the success of thin-film encapsulation of OLEDs. As such, the issues which prevented the successful encapsulation of an OLED with the zero-stress stack must be identified, explored and overcome. From my studies, some clear starting points for this research have emerged:

- Difference in thermal coefficient of expansion between organic and thin film. This is an important factor which determines the ultimate residual stress of the encapsulant film.
- Adhesion of thin film to substrate. Poor adhesion of the encapsulation to the organic, metal or substrate surface can lead to buckling and catastrophic failure of the encapsulation.
- Difference in surface properties on the device. Patterning of the organic and metal layers creates a situation where the surface of the organic device is a mosaic of different materials. Since the properties (namely those mentioned above) vary from material to material, optimizing the encapsulation scheme for one material may lead to exacerbated stress effects on another region of the device. Techniques for avoiding this problem must be developed.

In addition, it would be advantageous for future researchers to investigate the possibility of applying other thin film deposition techniques, such as Atomic Layer

Deposition, to the task of device encapsulation. It is likely that a deposition technique which is able to cleanly deposit low stress films will yield greater success in this endeavor.

Finally, there is a considerable body of work devoted to the subject of environmentally assisted fracture and cracking. Studies in this field focus on the effect of morphological changes, spurred by exposure to atmospheric oxidants, on the buildup of stress, the propagation of cracks and the premature failure in polymers, metals and ceramics. This is a similar subject to that of cathode delamination, which is also initiated and exacerbated by exposure to atmospheric oxidants. While it is beyond the scope of this thesis, which take a blunt-instrument approach to the prevention of cathode delamination, to explore the detailed failure of the cathode layer through the auspices of environmentally assisted fracture, it may prove fruitful for future studies interested in this phenomenon.

Pulsed Driving Methods

Dark, non-emissive region growth is a major failure mode in OLEDs. As the non-emissive regions increase in size, the total luminance of the OLED decreases as well. Dark spot formation and growth is a ubiquitous phenomenon, noticed by many researchers. The immediate cause of dark spot formation and growth has been identified in the literature as delamination of the metallic cathode from the organic layers underneath. Details of this process can be found in Chapter 7.

It has been suggested that this delamination process is entirely independent of the applied field and dependent solely on the atmospheric conditions – relative humidity

and partial pressure of oxygen in particular. The results shown in Chapter 7 clearly show that there is, indeed, a dependence of the dark spot growth rate on the applied field, since the growth rate varies as the duty cycle of the applied pulse changes. The value of such a conclusion is seen in the nearly two orders of magnitude increase in OLED lifetime (as measured by dark spot area) as the duty cycle is decreased from 100% (DC sourced) to 5%. Indeed, combination of pulsing at 50% duty cycle and thin film encapsulation produced a device which, after nearly 1000 hours in ambient conditions, had only 21% of the emission area consumed by dark regions.

The lifetime measurements reported in these studies, as well as some of the packaging studies, were made with a custom-built tool for inspecting the device during operation. The design of this tool allows the researcher to source the OLED with a constant-voltage DC pulse train. Of course, the amplitude of the pulse train is not the only parameter of concern in these studies. Other metrics, such as current and luminance, are important to these studies and could be used as control points for the lifetime experiments. In other words, constant-voltage sourcing is but one of several possible schemes which also include constant-current and constant-luminance. Unfortunately, the lifetime measurement tool used for the studies in Chapter 6 cannot maintain either constant current or constant luminance. These other control schemes offer a lot of insight in to the decay mechanisms of OLEDs and are, in fact, used with greater frequency than constant-voltage in the literature. Constant-voltage is, in reality, an unlikely control scheme for commercial devices since the voltage will need to be adjusted to compensate for decreases in device luminance over time.

Future Work: The lifetime measurement tool should be updated to allow measurement by constant-voltage, constant-current and constant-luminance control. While the constant-voltage control scheme is the default (and only) scheme, it is lacking in the ability to measure the applied current. This is a more difficult task than originally envisioned. Generally, a resistor of known resistance can be placed in series with the device under test and the voltage across that device would give an accurate measure of the current through the OLED. However, since the resistance of the OLED device changes over time, the voltage divider formed by the OLED and resistor will change, counter to the design of a constant-voltage control. A large passive resistor would reduce the voltage swing as the OLED ages, but the loading would require a very high voltage from the pulse generator to produce an appreciable signal across the OLED.

Of the latter two functions to be added, constant-current should pose the least difficulty. To achieve a constant-current control mechanism, the pulse generator currently in use can either be replaced with a pulsed current source, or outfitted with a current source circuit which converts the voltage input in to a current pulse. Such a current source would need to simultaneously measure the applied voltage so to accurately record the conditions of the OLED.

The constant-luminance control scheme is, perhaps, the most involved since luminance is a result of the applied driving scheme. A future implementation of this type of device would need to incorporate a feedback loop and controlling software which would adjust the applied current pulse and/or duty cycle to maintain constant luminance from the OLED. In any control scheme, the appropriate communications between this device and

a computerized control program should be realized to record voltage, current, luminance as well as continue to collect device images.